Synthese von Nanopartikeln mittels Lichtbogenentladung und deren Anwendung in Beschichtungen

Von der Fakultät für Ingenieurwissenschaften,
Abteilung Elektrotechnik und Informationstechnik
der Universität Duisburg-Essen

zur Erlangung des akademischen Grades

Doktor der Ingenieurwissenschaften

genehmigte Dissertation

von

Qingqing Fu
aus
Shandong

1. Gutachter: Prof. Dr.-Ing. Frank Einar Kruis
2. Gutachter: Prof. Dr. Markus Winterer
Tag der mündlichen Prüfung: 25.06.2024

Arc discharge synthesized nanoparticles and their applications in thin film coatings

From the Faculty of Engineering,

Department of Electrical Engineering and Information Technology,

University of Duisburg-Essen

To obtain the academic degree

Dr.-Ing.

Approved Doctoral Thesis

by

Qingqing Fu
from
Shandong

1. Examiner: Prof. Dr.-Ing. Frank Einar Kruis
2. Examiner: Prof. Dr. Markus Winterer
Date of the oral examination: June 25, 2024

“Learning without thinking leads to confusion, thinking without learning ends in vain”.

“学而不思则罔，思而不学则殆”。

-----CONFUCIUS

-----孔子

Hiermit versichere ich, die vorliegende Dissertation selbstständig, ohne fremde Hilfe und ohne Benutzung anderer als den angegebenen Quellen angefertigt zu haben. Alle aus fremden Werken direkt oder indirekt übernommenen Stellen sind als solche gekennzeichnet. Die vorliegende Dissertation wurde in keinem anderen Promotionsverfahren eingereicht. Mit dieser Arbeit strebe ich die Erlangung des akademischen Grades Doktor der Ingenieurwissenschaften (Dr.-Ing.) an.

Ort, Datum

Author name

Acknowledgments

This doctoral dissertation could not have been accomplished without the support, guidance, and encouragement of numerous individuals. My heartfelt appreciation goes to everyone who has been a part of my life throughout my doctoral journey. Your unwavering support was crucial to the completion of this work.

I extend my deepest gratitude to my advisor, Prof. Dr.-Ing. Einar Kruis. You provided me with the invaluable opportunity to embark on my academic path. Your continuous support and encouragement have been my guiding light throughout this journey. I am immensely thankful for our insightful discussions, the trust you placed in me, and the academic freedom you afforded me. Your mentorship has been instrumental in my personal and professional growth over these years.

My sincere thanks also to Prof. Dr.-Ing.Dipl.-Wirt.Ing. Wolfgang Tillmann for the chance to engage in a collaborative project. Your support and encouragement throughout our collaboration have been greatly appreciated. Special acknowledgment goes to David Kokalj, the project leader, whose relentless research efforts and inquisitive nature have greatly fueled my passion for academia. Our joint work has significantly contributed to my development and stands out as a highlight of my doctoral studies.

I am grateful to Prof. Dr. Markus Winterer and Claudia Gorynski for their readiness to assist whenever I needed access to their experimental facilities. Additionally, my gratitude extends to Prof. Dr. Winterer for his gracious willingness to be my secondary assessor of this doctoral thesis.

I extend my heartfelt gratitude to all my colleagues at the Institute of Technology for Nanostructures for fostering a welcoming, open, and respectful environment that significantly enriched my research journey. My sincere thanks go to Dennis Kiesler, Thore Rosenberger, and Gregor Kotalczyk for their technical expertise. Their invaluable support was essential during the early years of my PhD studies. I deeply appreciate Ivan Skenderovic, Max Frei, and Matthias Masuhr, who were always there for discussions, support, and encouragement. Their presence significantly enriched my doctoral journey. Thanks to my colleagues Jonah Weidemann, Clemens Adler, and Xuebei Zhu for their daily support, making my work more manageable. My appreciation also to Martin Dehnen and Felix Bensel for their laboratory support, offering invaluable knowledge and technical assistance that streamlined my research process.

Gratitude is extended to all the students I've mentored over the last five years. Your engagement and enthusiasm have not only propelled this work forward but have deepened my understanding and commitment to this field. Your insights and queries have been a source of motivation and self-reflection, encouraging me to pursue continuous academic growth. Embarking on PhD research presented significant mental and physical challenges.

I am profoundly thankful for the friends who have been by my side, offering joy and motivation. Special thanks to Claudia Gorynski, Ling Fang, and Xuebei Zhu for their encouragement and for introducing me to various physical activities, which became a vital source of energy for completing my dissertation.

Lastly, my deepest gratitude is reserved for my husband, my parents, and my in-laws. Your unconditional support, boundless patience, and love have been my sanctuary. In every challenge and triumph, your presence has been a pillar of strength and comfort.

Qingqing Fu
February 2024

Abstract

The arc discharge method for nanoparticle production offers all the benefits of gas-phase (aerosol-based) synthesis, including high-throughput production, exceptional purity, continuous operation, and straightforward design. This method is especially effective for synthesizing non-oxide materials, such as metals and ceramics. This work studied the synthesis of metallic copper (Cu) and ceramic titanium nitride (TiN) nanoparticles using an optimized arc discharge reactor, with a focus on how different processing parameters affect the properties of the nanoparticles. Additionally, this research explored the potential applications of these nanoparticles, particularly focusing on Cu nanoparticles for electrically conductive thin films and TiN nanoparticles for protective coatings.

Copper nanoparticles (Cu NPs) emerge as cost-effective substitutes for noble metals like silver and gold in conductive inks, due to their superior electrical conductivity and affordability. Through adjusting the reactor process, a steady production rate of 1.2 to 5.5 g/h was achieved, producing Cu nanoparticles with a primary size of less than 100 nm. These nanoparticles were then used to develop copper inks and subsequent thin films on glass substrates. A thermal sintering process eliminated ink residues and reduced copper oxide in the films, achieving a continuous metallic structure within the sintered Cu films. The copper films exhibited low resistivity, three times that of bulk copper, after thermal sintering in a reducing atmosphere. To reduce film porosity, a multilayer sintering technique was developed, enabling the preparation of a denser Cu film through up to four coating and sintering cycles, significantly lowering porosity from 33.6 % in single-layered to 3.7 % in four-layered sintered films. This reduction in porosity correlates with decreases in electrical resistivity, demonstrating the effectiveness of this multilayer sintering method.

Similarly, titanium nitride nanoparticles (TiN NPs), preferred for protective coatings due to their outstanding thermal, mechanical, and chemical stability, were synthesized in an optimized arc discharge reactor. The research explored the effect of parameters like quench gas velocity, composition, and arc current on nanoparticle quality, yield, and size, finding that higher gas velocities led to smaller particles (10-15 nm). It also proposed a mechanism for cathode tip deposit growth, enhancing understanding of the synthesis process and offering optimization insights. Utilizing optimized parameters, the study produced nanostructured thin films through a novel method combining an atmospheric-pressure arc reactor with a magnetron sputter device, achieving nanocrystalline (nc)-TiN/nc-CrN nanocomposite structures. Microstructural analysis confirmed the successful integration of TiN nanoparticles without significant lateral interface defects. However, pores near TiN nanoparticles indicated that external nanoparticles might disrupt the vertical columnar growth of the CrN Matrix. The research also found that increasing TiN nanoparticle content decreased CrN crystallite sizes and increased grain boundaries, indicating the potential for mechanically enhanced thin films.

Keywords: Arc discharge synthesis, Aerosol particles, Cu conductive films, TiN hard coatings, Nanocomposites .

Zusammenfassung

Synthese von Nanopartikeln mittels Lichtbogenentladung bietet alle Vorteile der Gasphasensynthese (auf Aerosolbasis), einschließlich der Produktion mit hohem Durchsatz, außergewöhnlicher Reinheit, kontinuierlichem Betrieb und unkompliziertem Design. Diese Methode ist besonders effektiv für die Synthese von Nicht-Oxid-Materialien wie Metallen und Keramiken. In dieser Arbeit wurde die Synthese von metallischen Kupfer- (Cu) und keramischen Titannitrid- (TiN) Nanopartikeln mit Hilfe eines optimierten Lichtbogenreaktors untersucht, wobei der Schwerpunkt darauf lag, wie verschiedene Verfahrensparameter die Eigenschaften der Nanopartikel beeinflussen. Darüber hinaus wurden die potenziellen Anwendungen dieser Nanopartikel untersucht, mit zwei weiteren Schwerpunkten: Der Einsatz von Kupfernanopartikeln für elektrisch leitfähige Dünnschichten und der von Titannitrid-Nanopartikeln für Schutzschichten.

Kupfernanopartikel (Cu NPs) sind aufgrund ihrer hervorragenden elektrischen Leitfähigkeit und ihres Preisvorteils ein kostengünstiger Ersatz für Edelmetalle wie Silber und Gold in leitfähigen Druckfarben. Durch Anpassung des Reaktorprozesses wurde eine stabile Produktionsrate von 1,2 bis 5,5 g/h erreicht, wodurch Cu-Nanopartikel mit einer Primärgröße von weniger als 100 nm hergestellt wurden. Diese Nanopartikel wurden dann zur Entwicklung von Kupfertinten und anschließenden Beschichtungen auf Glassubstraten verwendet. Durch ein thermisches Sinterverfahren wurden Tintenreste entfernt und das Kupferoxid in den Filmen reduziert, so dass die gesinterten Cu-Filme eine durchgehende Metallstruktur aufwiesen. Die Kupferschichten wiesen nach dem thermischen Sintern in einer reduzierenden Atmosphäre einen niedrigen spezifischen Widerstand auf, der dreimal so hoch war wie der von massivem Kupfer. Zur Verringerung der Porosität der Schichten wurde ein mehrstufiges Sinterverfahren entwickelt, das die Herstellung einer dichteren Cu-Schicht durch bis zu vier Beschichtungs- und Sintervorgänge ermöglichte und die Porosität von 33,6 % bei einschichtigen Schichten auf 3,7 % bei vierschichtigen gesinterten Schichten deutlich verringerte. Diese Verringerung der Porosität korreliert mit einer Verringerung des elektrischen Widerstands, was die Wirksamkeit dieses mehrstufigen Sinterverfahrens beweist.

In einem anderen Fall wurden Titannitrid-Nanopartikel (TiN NPs), die aufgrund ihrer hervorragenden thermischen, mechanischen und chemischen Stabilität für Schutzschichten bevorzugt werden, in einem optimierten Lichtbogenreaktor synthetisiert. Die Forschung untersuchte die Auswirkung von Parametern wie Quenchgasgeschwindigkeit, Zusammensetzung und Lichtbogenstrom auf die Qualität, Ausbeute und Größe der Nanopartikel und stellte fest, dass höhere Gasgeschwindigkeiten zu kleineren Partikeln (10-15 nm) führten. Außerdem wurde ein Mechanismus für das Wachstum der Kathodenspitzenablagerungen vorgeschlagen, der das Verständnis des Syntheseprozesses verbessert und Erkenntnisse für die Optimierung liefert. Unter Verwendung optimierter Parameter wurden in der Studie nanostrukturierte Dünnschichten durch eine neuartige Methode hergestellt, bei der ein Atmosphärendruck-Lichtbogenreaktor mit einer Magnetron-Sputter-Anlage kombiniert wurde, wodurch nanokristalline (nc)-TiN/nc-CrN Nanokompositstrukturen erzielt wurden. Die mikrostrukturelle Analyse bestätigte die erfolgreiche Integration von TiN-Nanopartikeln ohne signifikante seitliche Grenzflächendefekte. Poren in der Nähe von TiN-Nanopartikeln wiesen jedoch darauf hin, dass externe Nanopartikel das vertikale säulenförmige Wachstum der CrN-Matrix stören könnten. Die Forschungsarbeiten ergaben auch, dass mit zunehmendem Gehalt an TiN-Nanopartikeln die CrN-Kristallitgrößen abnahmen und die Korngrenzen zunahmen, was auf das Potenzial für mechanisch verbesserte dünne Schichten hinweist.

Schlüsselwörter: Lichtbogensynthese, Aerosolpartikel, leitfähige Cu Schichten, TiN-Hardschichten, Nanokomposites.

List of publications

(1) Qingqing Fu, Matthias Stein, Wen Li, Jingzhi Zheng, Frank Einar Kruis
Conductive films prepared from inks based on copper nanoparticles synthesized by transferred arc discharge, Nanotechnology 31 (2020) 025302
https://doi.org/10.1088/1361-6528/ab4524

(2) Qingqing Fu, David Kokalj, Dominic Stangier, Frank Einar Kruis, Wolfgang Tillmann
Aerosol synthesis of titanium nitride nanoparticles by direct current arc discharge method, Advanced Powder Technology 31 (2020) 4119-4128
https://doi.org/10.1016/j.apt.2020.08.012

(3) Qingqing Fu, Wen Li, Frank Einar Kruis
Highly conductive copper films prepared by multilayer sintering of nanoparticles synthesized via arc discharge, Nanotechnology 34 (2023) 225601
https://doi.org/10.1088/1361-6528/acbd1f

(4) Qingqing Fu, Frank Einar Kruis
Determining the ultraviolet radiation dose experienced by aerosols using ultraviolet-sensitive dyes, Aerosol Research 2 (2024) 77-92
https://doi.org/10.5194/ar-2-77-2024

(5) Wolfgang Tillmann, David Kokalj, Dominic Stangier, Qingqing Fu, Frank Einar Kruis
Combination of an atmospheric pressured arc reactor and a magnetron sputter device for the synthesis of novel nanostructured thin films, Thin Solid Films 689 (2019) 137528
https://doi.org/10.1016/j.tsf.2019.137528

(6) Wolfgang Tillmann, David Kokalj, Dominic Stangier, Qingqing Fu, Frank Einar Kruis
Influence of the PVD process conditions on the incorporation of TiN nanoparticles into magnetron sputtered CrN thin films, Surface & Coatings Technology 409 (2021) 126935
https://doi.org/10.1016/j.surfcoat.2021.126935

(7) Wolfgang Tillmann, David Kokalj, Dominic Stangier, Qingqing Fu, Frank Einar Kruis
Bias-voltage effect on the TiN nanoparticle injection into magnetron sputtered CrN thin films towards nc-TiN/nc-CrN composites, Applied Surface Science Advances 6 (2021) 100149
https://doi.org/10.1016/j.apsadv.2021.100149

(8) Wolfgang Tillmann, David Kokalj, Dominic Stangier, Qingqing Fu, Frank Einar Kruis, Lukas Kesper, Ulf Berges, Carsten Westphal
On the synthesis and structural evolution of artificial CrN/TiN nanocomposites, Applied Surface Science 535 (2021) 147736
https://doi.org/10.1016/j.apsusc.2020.147736

Conference contributions

(1) Qingqing Fu, David Kokalj, Frank Einar Kruis, Wolfgang Tillmann; Synthesis of novel nanocomposite coatings via external nanoparticle injection **(Poster)**
2nd Materials Chain International Conference (MCIC), Bochum, Germany, 12-14 November 2018

(2) Qingqing Fu, David Kokalj, Dominic Stangier, Wolfgang Tillmann, Frank Einar Kruis; Optimization of an arc discharge process for external nanoparticle injection into a PVD chamber **(Poster)**
Annual Meeting of the DECHEMA specialist group ProcessNET, Frankfurt am Main, Germany, 6-7 March 2019

(3) Qingqing Fu, Frank Einar Kruis; Conductive films prepared from inks based on copper nanoparticles synthesized by transferred arc discharge **(Poster)**
International Congress on Particle Technology (PARTEC), Nuremberg, Germany, 4-11 April 2019

(4) Qingqing Fu, Julian Neises, Frank Einar Kruis; Stable synthesis of tungsten and molybdenum nanoparticles by transferred arc discharge **(Talk)**
European aerosol conference (EAC), Gothenburg, Sweden, 25-30 August 2019

(5) Qingqing Fu, Frank Einar Kruis, David Kokalj, Dominic Stangier, Wolfgang Tillmann; Synthesis of novel nanocomposite coatings via combining an arc reactor and a magnetron sputter device **(Poster)**
European Aerosol Conference (EAC), Aachen (online), Germany, 31 August - 4 September 2020

(6) Qingqing Fu, Frank Einar Kruis; Determination of the UV radiation dose of an aerosol using UV-sensitive dyes to optimize UV room air filters **(Poster)**
Research conference pandemics: preparedness for future pandemics from a global perspective, online, organized by German Research Foundation, 15 November 2021

(7) Qingqing Fu, Frank Einar Kruis; Determining the ultraviolet radiation dose of an aerosol using ultraviolet-sensitive dyes **(Poster)** 11th International Aerosol Conference (IAC), Athens, Greece, 4-9 September 2022

(8.1) Qingqing Fu, Frank Einar Kruis, David Kokalj, Dominic Stangier, Wolfgang Tillmann; Synthesis of novel nanocomposite coatings via combining an arc reactor and a magnetron sputter device **(Talk)**
(8.2) Qingqing Fu, Wen Li, Frank Einar Kruis; Effect of multilayer sintering on porosity and electrical resistivity of copper films prepared from nanoparticles synthesized from arc discharge **(Flash communication, 5 min)**
9th World congress on particle technology (WCPT9), Madrid, Spain, 18-22 September 2022

(9) Qingqing Fu, Frank Einar Kruis; Determining the ultraviolet radiation dose of an aerosol using ultraviolet-sensitive dyes **(Talk)**
Annual Meeting of the DECHEMA specialist group ProcessNET, Paderborn, Germany, 28-30 March 2023

(10) Qingqing Fu, Frank Einar Kruis; Highly conductive copper films prepared from nanoparticles synthesized via the arc discharge method **(Poster)**
3rd CENIDE Conference, Bergisch Gladbach, Germany, 2-4 May 2023

Contents

List of Figures

List of Tables

List of Symbols

Greek symbols

symbol	definition	unit
α	Dimensionless coalescence parameter	-
β	Collision frequency	$\mathrm{m^3\,s^{-1}}$
η	Gas dynamic viscosity	$\mathrm{kg\,m^{-1}\,s^{-1}}$
η_c	Particle contraction factor	-
γ	Specific surface energy	$\mathrm{J\,m^{-2}}$
λ_g	Gas mean free path	m
λ	Wavelength of the X-ray beam	m
λ_e	Wavelength of the accelerated electrons	m
ω_Cu	Copper mass fraction in the ink	%
ρ	Volume electrical resistivity	$\Omega\,\mathrm{m}$
ρ_p	Particle density	$\mathrm{kg\,m^{-3}}$
ρ_TiN	Density of TiN	$\mathrm{kg\,m^{-3}}$
σ	Standard deviation	-
τ_f	Coalescence time	s
τ_c	Collision time	s
θ_r	Angular aperture of the used microscope objective	°
θ_{hkl}	Incident angle of XRD	°

Latin symbols

Symbol	Definition	Unit
A	Area	m^2
A_0	Constant for Cunningham correction	-
C_c	Cunningham correction	-
d_p	Particle diameter	nm
$\frac{\mathrm{d}v}{\mathrm{d}t}$	Growth rate	$\mathrm{m}^3\,\mathrm{s}^{-1}$
D	Diffusion coefficient	$\mathrm{m}^2\,\mathrm{s}^{-1}$
D_f	Focused diameter	nm
d_{hkl}	Spacing between diffracting planes	m
d_XRD	Crystalline size	nm
d_S	Stokes diameter	nm
d_M	Electrical mobility diameter	nm
d_prim	Primary diameter	nm
D_fm	Fractal dimension	-
e	Elemental charge constant	A s
E_I	Impactor collection efficiency	%
$f_{a,b}$	Frequency of the oscillating element before and after sampling	s^{-1}
F_d	Drag Force	N
ΔG	Gibbs free energies	J
ΔG^*	Critical free energy barrier	J
ΔG_s	free energy to form a new surface	J
ΔG_v	free energy to form a new volume	J
h	BET constant	-
I	Current	A
k	Correction factor for the four-point probe resistivity measurement	-
$\mathrm{k_B}$	Boltzmann constant	$\mathrm{J\,K}^{-1}$
k_0	Prefactor for fractal aggregates calculation	-
K_0	Spring constant related to the tapered element for TEOM device	$\mathrm{kg\,s}^{-2}$
l_res	Characteristics of the objective lens	m
M_m	Nuclei mass	kg
$\dot{m}$	Gas mass flow	$\mathrm{kg\,s}^{-1}$
Δm	Mass difference	kg
m	Refractive index of the viewing medium	-

m_{ink}	Ink mass	kg
m_{ref}	Dispersion mass without metal loading	kg
N	Number concentration	m^{-3}
n	Number of elemental charges	-
p	Pressure	Pa
p_{s}	Saturated pressure	Pa
p_{e}	Equilibrium pressure	Pa
p_0	Saturation pressure of absorbates	Pa
p_{Skimmer}	Skimmer pressure	Pa
p_{Chamber}	Chamber pressure	Pa
Q_{in}	Sheath gas flow of dilution systems	lpm
Q_{a}	Aerosol flow rate	lpm
Q_1	Reactor gas flow	lpm
Q_2	Reactor gas flow	lpm
Q/q	DMA sheath flow ratio	lpm
r	Particle radius	nm
${r_n}^*$	Critical cluster radius	nm
R_{sq}	Sheet resistance	$\Omega/\square$
S	Saturation ratio	-
Stk	Stokes number	-
Stk*	Stokes number for 50% collection efficiency	-
SSA	Specific surface area	$\mathrm{m}^2\,\mathrm{g}^{-1}$
t	thickness of a thin film	m
T	Temperature	K
V	Measured voltage	V
V_{m}	Atomic volume	m^3
V_0	Volume of the absorbed gas per gram absorbent	m^3
$V_{0\mathrm{m}}$	Volume of monolayer absorbed gas per gram absorbent	m^3
v_{1-4}	Gas velocity in aerodynamic lens system	$\mathrm{m\,s}^{-1}$
v_{x}	Velocity in x-direction	$\mathrm{m\,s}^{-1}$
W	Dilution factor	-
W_{A}	Work function	eV
Z_{p}	Electrical Mobility	$\mathrm{m}^2\,\mathrm{V}^{-1}\,\mathrm{s}^{-1}$

1 Introduction

1.1 Aerosol synthesis of nanoparticles and their applications

The term “nanoparticle” came to prominence in the early 1990s, along with related terms such as “nanoscaled” and “nanosized” particles. These describe particles that have at least one dimension within the 1 to 100 nm range. With a size between individual molecular (or atomic) and bulk solid structures, nanoparticles exhibit size-, shape-, and composition-dependent properties that distinguish them from bulk materials. For instance, the reduced size of nanoparticles affects their melting temperature, allowing them to be sintered at notably lower temperatures. Their magnetic properties can also be altered, leading to the formation of superparamagnetic particles. The size and structure of nanoparticles may lead to changes in thermal conductivity relative to their bulk material, either increasing or decreasing it depending on the specific material and its intended application. Electronic characteristics, such as bandgap tuning for electronics, photovoltaics, and optical adjustments in quantum dots, are affected as well. Furthermore, nanoparticles have a much higher surface-area-to-volume ratio than their bulk counterparts, enabling their application in catalysis and porous membranes. Current research is strongly focused on the synthesis of tailor-made nanoparticles for unique functional applications in various scientific and technological fields. These include areas such as optoelectronics, semiconductor devices, sensors, biomedical applications, energy storage, supercapacitors, and environmental applications [142, 103, 171].

Aerosol-based (gas-phase) technologies have been extensively studied and employed to synthesize functional nanoparticles with specific desired properties. A variety of techniques can be utilized to prepare aerosol-based nanoparticles, with the selection largely based on the desired size and material composition. Flames, plasmas, lasers, and wall-heated reactors can be exploited to produce a wide range of functional materials. These methods include synthesis techniques for most of the materials in the periodic table of elements, reinforcing their widespread use in nanoparticle synthesis. The preference for aerosol processes in producing nanoparticles arises from their inherent advantages over wet and solid chemical processes. Notable advantages include:

- High purity and no liquid byproducts

- Cost and energy efficiency in many cases
- A continuous process with limited fabrication and collection steps
- The possibility of scaling up
- Effective control over factors like particle size, crystallinity, and agglomeration degree (by sintering or size selection)

However, the use of aerosol processes for the synthesis of nanoparticles requires a comprehensive understanding of the challenges involved [96, 205]. The challenges that require careful consideration and control are:

- Formation of hard agglomerates (aggregates) due to high temperatures
- Potential for hollow, porous, or inhomogeneous particles
- Broad particle size distribution
- Contamination risks, especially when using low-cost precursors

1.2 Aerosol routes for film generation

Aerosol techniques present a diverse range of methods for fabricating films, capable of depositing various materials including ceramic superconductors, non-oxide ceramics, metal oxides, pure metals, organics, and composites. Aerosol-based film production can generally be classified into four main types: (1) using pre-existing aerosol droplets for surface deposition; (2) forming and depositing particles in situ to produce films; (3) employing hybrid methods that combine both particle and vapor deposition; and (4) delivering volatile precursors in aerosol form for subsequent evaporation and chemical vapor deposition (CVD) to produce films. In general, the performance of films produced via aerosol methods is assessed based on specific properties or criteria relevant to their application, typically including factors like purity, microstructure, morphology, uniformity, and deposition rate, among other specialized considerations [96].

In comparison to aerosol routes for producing particles, aerosol approaches for film production or modification are less well-studied and well-understood. The majority of aerosol-based film production research has been conducted within the fields of applied physics, materials science, and chemistry, focusing on achieving desired properties in the films. Yet, these studies often overlook a thorough analysis of aerosol dynamics and do not clearly identify the distinct deposition mechanisms at play. Advancing the potential of aerosol methods for material processing demands substantial research in several underexplored areas. This includes the need for developing physical or gas-phase reaction pathways to produce multicomponent

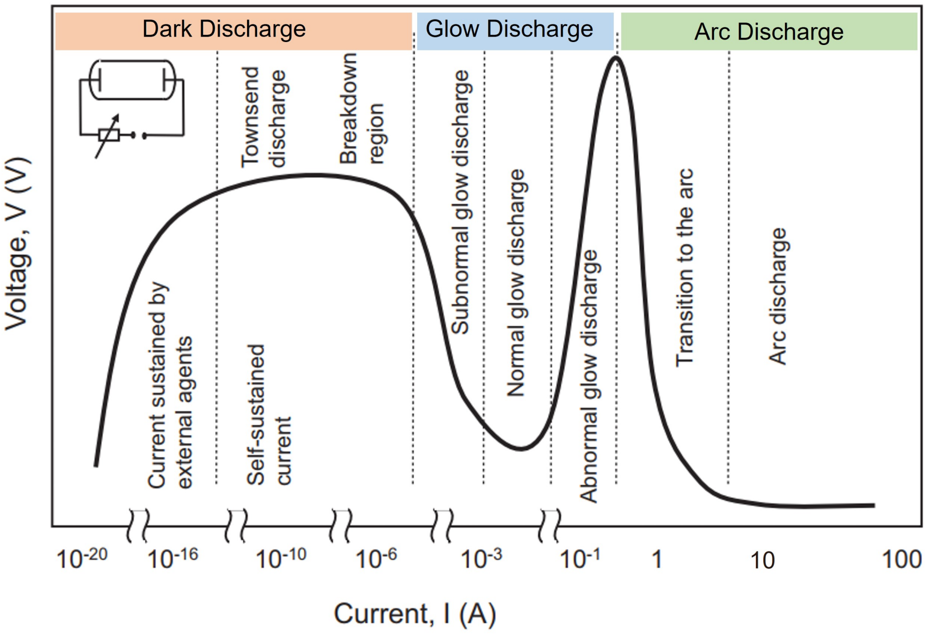

Figure **1-1**: Schematic representation of the different regimes for a DC discharge and their corresponding voltage-current characteristics, adapted from Boulos et al. [12].

materials, as well as exploring new precursors, either single-source or multi-source, designed with specific chemical properties for synthesizing novel materials [56, 57].

1.3 Arc discharge in the gas phase

When a strong electric field is applied between a pair of electrodes in a gaseous atmosphere, gaseous discharges can occur, leading to the generation of plasma–a gas that is partially or fully ionized. At room temperature, gases are typically excellent insulators. However, when a sufficient number of charge carriers are produced, the gas becomes electrically conductive. This transformation process is known as electrical breakdown. Arc discharge is a type of electrical breakdown in gas atoms/molecules, resulting in a sustained electrical discharge. The observed glow phenomenon is due to photons emitted from collisions between ions and electrons within the plasma. In a direct current (DC) discharge, arc discharge can usually be characterized as an electrical discharge of high current (10-200 A) at low voltage (5-30 V), as illustrated in Figure **1-1** [12]. Comprehensive discussions on the use of arc discharge in nanoparticle synthesis (Chapter 2) and the associated particle formation mechanism (Chapter 3) are presented in the following chapters.

1.4 This work

Arc discharge synthesis has all the advantages of gas-phase (aerosol-based) synthesis, including high purity, high yield, and a continuous process. By introducing different gas compositions, such as oxygen, nitrogen, and argon, a diverse range of nanoparticles–like metal, metal oxides, metal nitrides, and carbides–can be produced. This thesis aimed to synthesize nanoparticles using the DC arc discharge method, optimize the arc discharge reactor, and study the influence of process parameters on particle properties. Furthermore, potential applications in film coatings based on nanoparticles synthesized via this method were explored. This thesis specifically studied two nanoparticle systems, metallic copper (Cu) and ceramic titanium nitride (TiN), focusing on their synthesis and their applications in conductive thin films and protective coatings, respectively. The structure of this thesis is organized as follows:

- *Chapter 2* provides an overview of the various nanoparticles synthesized using arc discharge techniques and their functional applications. It also delves into the synthesis and potential applications of nanomaterials pertinent to this work, especially Cu and TiN nanoparticles.
- *Chapter 3* describes the fundamentals of particle formation in the gas phase. The measurement techniques used in this work, which are categorized into online and offline characterization, are also discussed.
- *Chapter 4* focuses on the synthesis of nanoparticles such as TiN and Cu using an arc discharge reactor. Especially for the synthesis of TiN and Cu NPs, the influence of process parameters, such as applied current, gas composition, and quench gas velocity, on the production rate and primary size of particles is discussed in detail.
- *Chapter 5* presents a process for producing Cu conductive films, which includes conductive ink preparation, thin film formation and sintering. This chapter discusses the role of sintering in a reducing atmosphere to overcome the challenge of the inherent oxidation of Cu NPs.
- *Chapter 6* addresses the porosity problem in copper films by introducing a multilayer sintering method. The evolution of the microstructure in the sintered films is analyzed.
- *Chapter 7* highlights the synthesis of artificial TiN/CrN nanocomposite coatings, using a combination of an atmospheric arc reactor and an industrial magnetron sputtering system. Three different aerodynamic lens systems were designed to inject TiN NPs at atmospheric pressure into a high vacuum physical vapor deposition (PVD) chamber. Discussions on the microstructure and defect evolution of the synthesized TiN/CrN are included. Insights into potential avenues for future research are provided.
- *Chapter 8* summarizes the main findings of this thesis.

2 State of the art

Part of this chapter has been published [43, 41, 42]. The first part of this chapter reviews various nanostructured materials synthesized by arc discharge methods and their applications. The second part describes the role of copper (Cu) nanoparticles in printed electronics, especially highlighting the challenges in producing highly electrically conductive copper films, such as nanoparticle oxidation and film porosity. The final part reviews the main synthesis routes for titanium nitride (TiN) nanoparticles and their potential applications in thin films.

2.1 Arc discharge synthesized nanoparticles and their applications

The development of modern technology has led to a demand for materials with specific properties that can perform optimally under desired conditions. Materials that are newly synthesized or prepared and possess a specific chemical and/or physical function are referred to as functional materials. In this context, nanoparticles are of particular interest because of their size-dependent properties, which include electronic, optical, magnetic, mechanical, and chemical properties that differ from those of both their constituent atoms/molecules and their corresponding bulk materials [174, 2]. Nanostructured materials with unique features can be used in various fields of science and technology, including optoelectronics, semiconductor devices, sensors, biomedical applications, energy storage, supercapacitors, environmental applications, magnetocaloric materials, solar harvesting functions, and so on [13, 6, 48, 133, 26, 198, 142].

Aerosol nanoparticles have been produced by various processes, including flame reactors [107, 19, 138, 167], tube furnace flow reactors [149, 148, 84, 141, 159], laser ablation [143], thermal plasmas [129, 163, 164, 134, 200], non-thermal plasmas [131, 169, 82, 199], and sputtering [58, 51]. Numerous comprehensive reviews already outline the development of various aerosol reactors and offer deeper insights into the current state of aerosol technology. For instance, Teoh et al. [186], Schulz et al. [171], and Li et al. [117] examined the recent trends of flame aerosol synthesis of nanostructured materials, emphasizing the processing, modeling, and diagnostics aspects of particle formation in flames for materials processing. Milosevic and colleagues [132] described the potential of the hot wall aerosol synthesis in generating nanoparticles with uniformly distributed components, phases, and internal structures. Both Kim et al. [90] and Ullmann et al. [195] summarized the latest studies on aerosol generation by laser ablation. Kortshagen et al. [100] reviewed the non-thermal plasma synthesis of nanostructured materials, including metal nanoparticles, elemental and compound semiconductor nanocrystals, and organic nanoparticle coatings. Grammatikopulos et al. [51] and Huttel et al. [66] give an overview of gas-phase synthesis by magnetron-sputtering to produce multifunctional nanoparticles. Currently, mostly flame-based reactors have been commercially utilized for producing fine particles. Examples include carbon black (Cabot, Columbia, Orion Engineered Carbons), fumed silica (Cabot, Evonik), pigmentary titania (DuPont, Ishihara, Millenium, Kerr-McGee, Cristal), and optical fibers (Corning, Heraeus, Lucent, Sumitomo) [160, 186].

Among the aforementioned aerosol processes for nanopowder synthesis, thermal plasma is promising for efficiently synthesizing non-oxide materials, such as pure metals and ceramics [15]. The arc discharge is one of the most applied methods to generate thermal plasmas. This method produces a thermal plasma with unique features of high temperatures (1000-10000 K) and high power density. These features provide the energy to vaporize coarse-grained solid materials and/or initiate chemical reactions. Nanoparticles subsequently form through the condensation of these plasma-generated vapors [36, 156, 136].

Furthermore, the arc discharge process inherits all the benefits of gas-phase (aerosol-based) synthesis, including its high-throughput production, exceptional product purity, continuous processing, and simple process design. Since the arc discharge method was first used to produce carbon nanotubes (CNT) by Iijima in 1991 [67], thermal plasma arc discharge techniques have been extensively researched and used for nanostructured materials and coatings [67, 4, 89]. To date, the synthesis of various kinds of nanoparticles, including metals, oxides, nitrides, carbides, borides, composites, and carbon-based materials, has been successfully achieved using arc discharge methods. In this perspective, the following section reviews the recent development with representative examples using the arc discharge process. Arc plasma produced by electrode-less radio frequency (RF), capacitive or inductively coupled discharges, and microwaves are excluded in this section.

2.1.1 Pure metal nanoparticles

Since the late 1990s, arc discharge methods have been explored to synthesize metal nanoparticles, including gold, silver, copper, aluminum, zinc, nickel, tungsten, iron, and others [111, 135, 10, 184]. Owing to their unique properties, metal nanoparticles have applications in optoelectronics, sensor technology, information storage, and catalysis. While various aerosol-based routes are known for producing pure metal nanoparticles – such as flame spray synthesis with highly reductive flames, hot wall reactors, microwave plasma reactors, and spark discharge generators – each has its drawbacks. These include heightened safety requirements for flame spray synthesis using reducing gases like hydrogen, potential contamination from liquid precursors, high energy consumption, extended heating/cooling periods in furnace flow reactors, and the need for possibly hazardous or expensive precursors in flame spray pyrolysis. In this regard, arc discharge synthesis emerges as a preferred method for preparing pure metal nanoparticles from metal feedstock in an oxygen-free environment. Given that most metals have relatively low melting temperatures, the optimal design of the crucible for thermal conductivity and the flow pattern for particle residence time becomes critically essential for the efficient synthesis of pure metal nanoparticles [37].

Chen et al. [21] introduced an atmospheric DC mini-arc plasma (30–40 A, 3 V, Ar plasma) source for the synthesis of nanocrystals. Using this mini-arc source, metallic silver nanoparticles with sizes up to 60 nm were produced at 1–10 mg/h rates. The arc is ignited between a tungsten cathode and a graphite crucible anode using a commercial TIG welder. Owing to the design of the crucible, the arc parameters (such as power) are independent of the feedstock material. Silicon nanopowders (<100 nm) were successfully prepared by converting micron-sized silicon powders (approximately 40 µm) using a DC arc plasma system (9–13 kW, 101 kPa, Ar plasma) [23]. Choi et al. [23] demonstrated that high input power led to the formation of spherical nanoparticles due to complete evaporation, whereas relatively low input power resulted in the production of nanowires. They observed that increasing the input power from 9 kW to 13 kW increased the mean diameter of synthesized silicon nanopowders from approximately 20 nm to 40 nm. Furthermore, a simple and cost-effective transferred arc discharge reactor was developed to produce pure metal zinc (80–400 nm), copper (approximately 65 nm), and silver (approximately 45 nm) nanoparticles at high production rates. X-ray diffraction (XRD) analyses were conducted to perform phase analysis of the crystalline components of the produced zinc, silver, and copper nanoparticles. No detectable metal oxide phases were present. Process parameters influencing the particle production rate include gas composition (Ar, He, N_2 and H_2), electrode design, gas flow rate, and the settings of the DC power supply (10–50 A, 15–25 V, 101 kPa) [180, 179, 178].

2.1.2 Metal oxide nanoparticles

Metal oxide nanoparticles are known for their exceptional resistance to high heat fluxes and corrosive chemicals. These properties make them ideal for catalysts, ceramics, paints, solar cells, and corrosion protection [5]. Until recently, flame-based synthesis (combustion) has been the dominant method for producing commercially available oxide nanoparticles, including titania, fumed silica, alumina, and zinc oxide. The source material is typically a solid metal electrode or powder precursor when using the arc discharge process to synthesize oxide particles. The flowing background gas is usually a mixture of nitrogen, argon, or helium, with oxygen serving as the reactive component. Metal oxides are produced via predominantly exothermic oxidation reactions. As a result, extremely high temperatures are

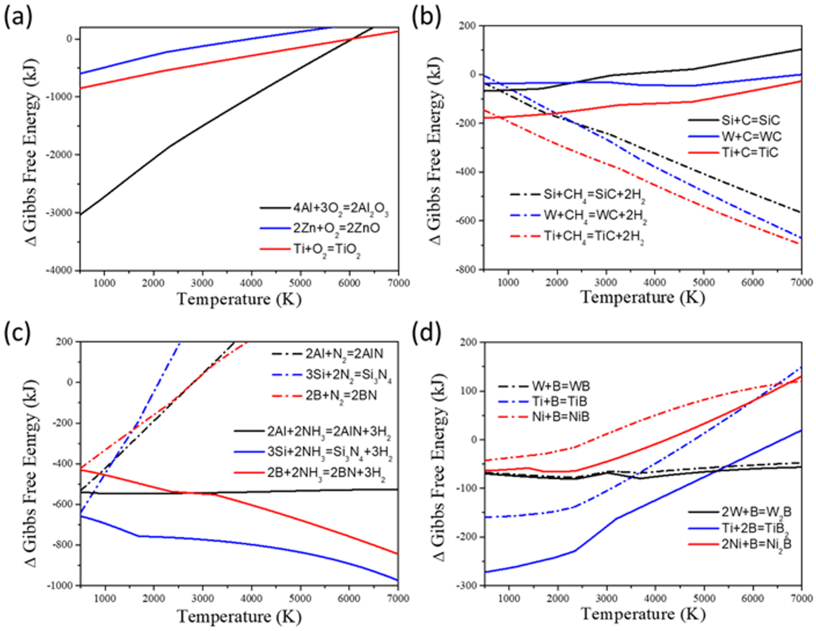

Figure **2-1**: Gibbs free energy of (a) oxidation, (b) carbonization, (c) nitridation, and (d) boridation reactions by thermodynamic equilibrium calculation, reproduced from Kim et al. [89], with permission from Journal of Applied Physics (Copyright 2019)

not thermodynamically favorable for oxide formation, according to Le Chatelier's principle. This is also supported by the Gibbs free energies ΔG calculations presented in Figure **2-1** by Kim et al. [89], which demonstrate that ΔG rises as temperature increases. Thus, the primary appeal of arc discharge methods lies in mass production with controlled phase structures and sizes rather than in the pursuit of ultrahigh temperature conditions [89].

Several research groups have synthesized high-quality titanium dioxide (TiO_2) nanoparticles with controlled structures [35, 194, 116, 90]. Specifically, Fang et al. [35] designed an arc discharge chamber that generated an arc between a pure titanium rod, which served as an anode, and a graphite disc acting as the cathode by a DC-transferred arc process. This DC arc process (60 A, 20 V, 300 Torr, air plasma) produced spherical TiO_2 nanoparticles (approximately 50 nm) with a mixture of anatase and rutile phases. Ushakov and his team synthesize nanosized ZrO_2 and copper oxide using a low-pressure arc discharge plasma process. For the synthesis of Cu_2O nanopowders, the correlation of the average particle size and the product of gas pressure and the arc discharge gap has been established [197, 196].

2.1.3 Metal carbide, nitride, and boride nanoparticles

Protective coatings with enhanced mechanical and tribological properties are widely used in modern applications, such as cutting tools, energy-efficient car engines and machining tools. Metal carbides, nitrides, and borides are often chosen for protective coatings owing to their excellent thermal, mechanical, and chemical stability. For example, most of these materials have high melting points over 3000 K, hardness, wear resistance, and chemical inertness [25, 137, 154]. Arc plasmas are particularly suited for synthesizing various metal carbide and nitride nanoparticles. As illustrated in Figure **2-1** (b) and **2-1** (c), certain metal carbonizing (e.g., reaction with methane) and nitriding (e.g., reaction with ammonia) processes are more thermodynamically favorable at elevated temperatures, as evidenced by the decreasing Gibbs free energies. In contrast, boridation reactions, compared to others, present a thermodynamic challenge with relatively high ΔG values, as shown in Figure **2-1** (d). Pure boron and metal electrodes are usually chosen as the feedstock in the arc discharge process when synthesizing metal borides. Given these considerations, controlling the process temperature to an optimal range is crucial for successfully synthesizing metal carbide, nitride, and boride nanoparticles.

Metal carbide nanoparticles, such as tungsten carbide (WC), silicon carbide (SiC), titanium carbide (TiC) and tantalum carbide (TaC), have been synthesized using DC arc plasma processes [93, 20, 3, 168, 77, 87]. In the case of SiC nanoparticle production, $SiCl_4$ precursors have been favored because of their high reactivity and the straightforward generation of silicon vapor. For instance, nanosized SiC powders were prepared from $SiCl_4$ precursors and methane gas using a DC arc plasma jet (8–12 kW, 101 kPa, $Ar/H_2/CH_4$ plasma). It was demonstrated that the quality of the SiC nanoparticles was affected by the process conditions involving the molar ratio of H/Si and C/Si, and the collection positions [146]. Tungsten carbide nanoparticles were produced using a triple DC arc discharge process (9–10 kW in each torch, 101 kPa, Ar/N_2 plasma). Here, micro-sized tungsten powders and different carbon sources were used as starting materials, including multi-wall carbon nanotubes (MWCNT), amorphous carbon, and CH_4 gas. The crystalline phase structure and morphology of the synthesized tungsten carbide nanomaterials were analyzed using XRD and field emission scanning electron microscopy (FE-SEM). These techniques were particularly useful in identifying differences arising from the various carbon sources [145].

Synthesis of metal nitride nanoparticles was reported using DC thermal plasma processes, such as aluminum nitride (AlN), silicon nitride (Si_3N_4), titanium nitride (TiN), magnesium nitride (Mg_3N_4), boron nitride (BN), gallium nitride (GaN) [188, 147, 93, 20, 3, 168, 77, 87, 95, 94, 93]. In these research studies, metal sources were derived from solid or vapor phase precursors, while ammonia and nitrogen gas were commonly employed as the nitriding agents. AlN nanoparticles were successfully synthesized from micro-sized aluminum powders using a DC arc plasma system (12 kW, 300 A, 101 kPa, $Ar/N_2/NH_3$ plasma). The flow rate of NH_3 is a crucial parameter influencing the crystallinity and particle size of the synthesized AlN particles [93]. While most metal nitride nanoparticles exhibit high crystallinity through thermal plasma processes, synthesizing crystalline silicon nitride (α-Si_3N_4) nanoparticles presents a significant challenge. At temperatures above 1850 °C, the existing silicon nitride materials decompose into silicon and nitrogen. Consequently, most Si_3N_4 reaction products are either contaminated with silicon nanoparticles or exhibit reduced crystallinity (DC, 10—11 kW, 15–75 kPa, $Ar/NH_3/H_2$ plasma, $SiCl_4$ as precursors) [3].

2.1.4 Composite nanoparticles

Composite nanoparticles consist of two or more components at the nanoscale, each of which possesses unique physical and chemical properties. The primary objective behind synthesizing composite nanoparticles is to integrate the beneficial features of each component and to overcome the limitations of single-component properties, enabling various functional applications [126]. In the arc discharge thermal plasma process, multiple atomic precursors are often employed to produce atomic vapors, forming nanoparticles through non-equilibrium condensation during a rapid temperature decrease. Generally, the resultant composite nanoparticles can be classified as simple hybrids, core-shell structure,s, or aggregations of individual nanoparticles of varied composition [103]. Many composite nanoparticles, including alloys [120, 153], metal-ceramics [140, 185], ceramic-ceramics [24], and carbon-metal composites [172, 139, 173, 11, 16], have been synthesized using arc discharge techniques. The potential applications of these nanocomposite powders vary based on the composition, structure, and crystallinity of the tailormade nanoparticles. For instance, challenges like oxidation and corrosion in metal nanoparticles have been addressed by enveloping them with atomically thin carbon or ceramic layers through arc plasma processes [11, 16].

2.1.5 Carbon nanomaterials

Carbon atoms can form covalent bonds with other carbon atoms in various hybridization states (sp, sp2, sp3) and with non-metallic elements. This distinct ability enables them to create diverse carbon allotropic structures, from small molecules to long chains to complex mesoporous architectures [45, 125, 29]. The discovery of carbon nanostructures, such as carbon fullerenes (0D) in 1985 [102], nanotubes (1D) in 1991 [67], and single-layer graphene sheets (2D) in 2004 [144], propelled extensive research into the preparation, properties, and potential applications of carbon nanomaterials. Carbon nanotubes (CNTs) are among the most researched carbon species due to their superior mechanical, electronic, thermal, optical, and chemical properties. The arc discharge method, being the oldest and most widely utilized technique, is essential for synthesizing high-quality CNTs, including single-walled nanotubes (SWNTs), double-walled nanotubes (DWNTs), and multi-walled nanotubes (MWNTs). Over the past two decades, arc discharge techniques for fabricating various carbon-based nanomaterials have been intensively investigated, resulting in many publications [4]. Comprehensive reviews on the state-of-the-art in carbon nanomaterials, encompassing synthesis, properties, and functionalization, have been provided by several research groups. Consequently, this thesis does not endeavor to review recent advances in carbon nanomaterials.

2.2 Copper nanoparticles for conductive thin films

Printed electronics have gained significant attention due to the reduced manufacturing costs and operational simplicity of electrical devices [109]. Generally, printed electronics involves using printing technologies to fabricate electronic circuits and devices. Examples include radio-frequency identification antennas (RFIDs), printed circuit boards (PCBs), thin film transistors, and light-emitting devices [1, 64]. Traditionally, electronic devices have been manufactured using techniques such as photolithography, vacuum deposition, and electroless plating processes. These traditional methods often require expensive equipment and skilled operators. Moreover, these processes usually rely on environmentally undesirable chemicals, resulting in substantial waste [113, 175]. Consequently, many research efforts are devoted to developing electronic printing techniques. In the field of printing electronics, an essential component is the presence of highly conductive patterns, such as conducting lines and films. As most printed electronics are based on the principle of transferring inks to a substrate, various conductive inks, comprising metal-based nanomaterials and carbon-based nanomaterials, have been extensively explored over the past few decades.

Conductive inks based on metal nanoparticles (NPs) or dissolved metal precursors are drawing increasing attention because of the high electrical conductivity of metals. Among them, metals such as silver (Ag, $6.3\times10^7\,\mathrm{S/m}$), copper (Cu, $5.96\times10^7\,\mathrm{S/m}$), gold (Au, $4.42\times10^7\,\mathrm{S/m}$), and aluminum (Al, $3.78\times10^7\,\mathrm{S/m}$), are the primary choices. Inks based on silver and gold, in particular, have been widely investigated and are already available commercially due to their high electrical conductivity and high resistance to surface oxidation [152]. Nevertheless, a notable limitation is the scarcity of silver and gold in the earth's crust, which makes their large-scale production expensive [64, 161]. Studies have shown that Cu NPs oxidize at a slower rate than Al NPs when exposed to ambient conditions [53, 113]. Consequently, copper emerges as a promising alternative for Ag and Au due to its high conductivity (6 % less than that of Ag) and lower cost [128].

Various techniques have been developed to synthesize Cu nanoparticles, including wet chemical methods as well as dry gas-phase processes. Wet-chemistry techniques offer the advantage of controlling particle shape and size, they inherently depend on precursor solutions, which often result in impurities within the final nanoparticles. Besides, many chemical synthesis

Table **2-1**: Comparison of the throughput of copper nanoparticles reported in previous studies. Reproduced from Fu et al. [43], with permission from Nanotechnology (Copyright 2020).

Method	**Copper Source**	**Stabilizer**	**Process Gas**	**Throughput**	**Authors**
Chemical Reduction	$Cu(CH_3COO)_2$	CTAB & PVP	N_2	4.8 g per Batch	Deng et al. [31]
Chemical Reduction	$CuSO_4$	PVP	Air	47-50 g per Batch	Lee et al. [112]
Arc Discharge	Cu Granules	-	N_2	5.5 g per hour, continuous	Stein et al. [179]
Arc Discharge	Cu Granules	-	N_2	69 g per hour, continuous	Stein et al. [181]

methods involve batch processing with an extended production timeline due to multiple processing stages, such as stirring, centrifuging, washing and drying. Therefore, most of these approaches are better suited for laboratory-scale synthesis rather than large-scale production [171].

Only some researchers focused on the challenges of scaling up throughput for copper nanoparticles. Deng et al. [31] introduced a high throughput, large-scale process for producing copper nanoparticles using a chemical reduction method. They achieved a throughput of 4.8 grams per batch, using copper acetate for copper ions, and polyvinylpyrrolidone (PVP) and cetyltrimethylammonium bromide (CTAB) as the stabilizer. Similarly, Lee et al. [112] reported a large-scale synthesis of copper nanoparticles through chemically controlled reduction, attaining a throughput of 60 grams per batch. Recently, advancements have been made using an arc discharge thermal plasma process for the synthesis of metal nanoparticles such as Cu, Ag, Zn, and Al. Studies indicate that the optimized arc reactor can produce several grams of pure copper nanoparticles per hour [179]. Moreover, research into scaling-up production rates through the parallelization of transferred arcs (electrode pairs) has been promising. It has been revealed that the copper nanoparticle production rate increases linearly with the number of electrode pairs used, while maintaining the primary particle size within nanoscale [181]. Table **2-1** offers a summarized overview of the production rates achieved using these synthesis methods.

One of the primary challenges associated with Cu NPs is their tendency to oxidize in ambient air. Oxidation on the surfaces of Cu nanoparticles can significantly reduce the electrical conductivity of printed patterns and require higher sintering temperatures. Much research has been undertaken to minimize the effect of oxidation. Strategies to address the oxidation problem generally fall into three categories: storing Cu NPs in an inert atmosphere [9, 118], coating Cu NPs with a non-oxidizable shell [27, 70, 150], removing the surface oxide layer during post-printing treatment [18, 69, 206, 106]. Copper patterns with an electrical conductivity as high as 2.5×10^7 S/m, which is a level comparable to that of noble metals, have been reported. This has been achieved by coating Cu NPs with organic surfactants (such as PVP and oleic acid), followed by sintering in a reducing atmosphere (such as in hydrogen or carboxylic acid with nitrogen as carrier gas) [69, 91, 88]. Nevertheless, it is noteworthy that the copper nanoparticles used in these studies were synthesized by wet-chemistry techniques, where the copper salts get reduced to copper while the corresponding reducing agents get oxidized.

Apart from the oxidation problem, another factor affecting the electrical resistivity is the thin film porosity after sintering [79, 92, 121, 68, 119, 165]. Compared with Cu patterns with a bulk structure, the porous structure in sintered films could significantly accelerate oxidation process. To the best of our knowledge, only some studies have addressed the problem of copper film porosity. Joo et al. [74] added Cu nanowires (NWs) in a Cu NP ink, aiming to obtain a densely packed Cu NW/NP structure and thereby enhance the electrical conductivity of sintered Cu films. Their findings indicate a porosity reduction to 4.07 % in flashlight-sintered Cu NW/NP films, with an electrical resistivity as low as $22.77\,\mu\Omega\cdot\text{cm}$ (4.39×10^6 S/m). Rosen et al. [165] used a combination of heat and pressure during sintering to produce a dense copper layer. Copper patterns with an equivalent specific resistivity as low as $5.3 \pm 0.3\ \mu\Omega\cdot\text{cm}$ (1.89×10^7 S/m) were reported. Their analysis, including layer morphology and cross-section images, revealed that a high temperature and pressure 225 °C and 1260 pound/inch^2 results in a denser copper layer. However, a detailed discussion on the relationship between porosity evolution and electrical resistivity of Cu films is lacking. Chan et al. [18] introduced a progressive three-step sintering, including low-pressure drying, near-infrared sintering, and intense pulsed light (IPL), aiming for maximum nanoparticle compactness and minimal oxygen content. This approach reduced the porosity of the sintered Cu thin film to 6.3 %, and the electrical resistivity of Cu films was further decreased to $7.9\,\mu\Omega\cdot\text{cm}$ (1.27×10^7 S/m).

2.3 Titanium nitride nanoparticles for protective coatings

Titanium nitride (TiN) has attracted considerable interest because of its outstanding mechanical and tribological properties, such as high hardness and excellent wear resistance [155, 101, 183]. TiN-based thin films are commonly applied in metal cutting tools and aerospace engineering [154, 99, 72]. Additionally, with its high melting temperature of 2930 °C, TiN has emerged as a promising material for plasmonic applications, offering an alternative to traditional plasmonic metals like gold and silver, which have limitations due to their softness and lower melting points [158, 55, 54]. Recent reports indicate that titanium nitride nanoparticles have potential applications in biomedical devices because of their chemically inert properties [33]. Furthermore, nanocomposite coatings containing transition metal nitrides, such as TiN, have enhanced properties such as hardness, oxidation resistance, and wear protective behavior [86, 157].

A nanocomposite thin film comprises at least two distinct phases that incorporate different components, resulting in combined characteristics such as high hardness and substantial ductility. Hardness is defined as a material's resistance to plastic deformation. In crystalline materials, plastic deformation occurs predominantly through dislocation movement under an applied load [154]. In nanocomposite thin films, high hardness is often attributed to the small size of nanocrystalline (nc-) grains, resulting in numerous grain boundaries and, consequently, the absence of dislocation activity [8]. So far, apart from the research in this thesis, no literature has reported a thin film with an nc-CrN/nc-TiN nanocomposite structure, even though both CrN and TiN are commonly used materials for hard coatings.

Basically, physical vapor deposition (PVD) technology offers three possible ways to produce thin films with nanocomposite structures. One possibility is to select two metals with a miscibility gap at specific ratios, forming mixed crystals of varying structures. Another method involves using metals with significantly different nitrogen affinities, leading to nanocomposite structures, such as nanocrystalline metal nitride (nc-MeN)/nc-MeN and nc-MeN/nc-Me. The most widely used approach is selecting a nitride-forming transition metal that is nanocrystalline-sized and encapsulated within an amorphous matrix [192, 190, 191, 193]. However, these conventional processes described above cannot achieve a nc-TiN/nc-CrN nanocomposite structure when using Cr and Ti as the target materials. Instead, a single-phase Cr-Ti-N solid solution is obtained using conventional PVD technology, since both Ti and Cr are transition metals with a high affinity for nitrogen [22, 60, 210, 17, 44]. To address this limitation, a novel hybrid process was proposed [17, 85, 47]. In this process, TiN nanoparticles and CrN thin films are synthesized separately in two independent devices. However, the synthesized TiN nanoparticles are simultaneously deposited during the PVD thin film growth process, enabling the creation of artificial nc-TiN/nc-CrN nanocomposites.

The growing demand for nanosized titanium nitride particles has led to the development of various synthesis methods over the past years. For instance, one approach involves the direct nitridation of titanium oxide nanoparticles in an ammonia gas flow. By adjusting the nitridation time and temperature (from 800 to 1100 °C), TiN nanoparticles, with sizes ranging from 20 nm to 72 nm, could be obtained [115]. Huang et al. [65] developed a method to synthesize nanocrystalline titanium nitride by reacting titanium dioxide with sodium amide for 12 hours. X-ray diffraction (XRD) and transmission electron microscopy (TEM) analysis indicated that the product had a cubic phase with particle sizes of about 10 nm to 40 nm. Besides, the formation of TiN nanoparticles by using titanium tetrachloride ($TiCl_4$) as a precursor is possible as well. Dekker's group [30] has investigated the formation of TiN nanoparticles using titanium tetrachloride ($TiCl_4$), ammonia, and hydrogen. Yang et al. [207] also synthesized titanium nitride powders by using titanium tetrachloride ($TiCl_4$) with ammonium chloride (NH_4Cl) and metallic sodium (Na) as reactants. TEM images revealed that the produced particles possessed irregular shapes and displayed particle sizes of 5 nm to 10 nm. More recently, Grillo et al. [52] studied the vapor phase synthesis based on the ammonia and titanium chloride reaction. It was observed that the particle size analyzed by TEM was smaller than 50 nm. However, these synthesis techniques are based on chemical reactions that inevitably require precursor powders or solutions. Usually, these applied precursors and their byproducts reduce the purity of the synthesized nanoparticles. Furthermore, some of these methods pose challenges regarding production rate and nanoparticle size control [115, 65, 207, 71].

Arc plasma synthesis has been demonstrated as a promising way to produce high-purity nanoparticles of metals and metal-based compounds, such as metal oxides, nitrides, and carbides [86, 129, 179]. From a cost perspective, arc plasma synthesis offers an advantage because it is a nonvacuum technique and requires a cost-effective setup. Only a few researchers have successfully synthesized titanium nitride nanoparticles using the arc discharge method. Mahoney's group [129] used an arc plasma to synthesize TiN nanoparticles by evaporating Ti and simultaneously introducing nitrogen (up to 10 %) in an argon carrier gas. TEM images and the corresponding transmission electron diffraction (TED) pattern revealed that the sizes of the generated TiN nanoparticles are 20–50 nm. Recently, a simple setup has been developed to produce titanium nitride, carbide, and carbonitride nanoparticles by applying reactive arc evaporation of solid titanium. The study by Kiesler et al. [86] demonstrated that the nanoparticle composition could transition from titanium nitride over titanium carbonitride to titanium carbide by adjusting the gas composition of nitrogen, argon, and methane. The crystallite size of TiN particles, synthesized in pure N_2, was determined to be approximately 25 nm based on XRD analysis. All the studies mentioned above showed that titanium nitride nanoparticles could be successfully produced by adding nitrogen as a reactive gas in the arc plasma. Observations indicated that a small fraction of nitrogen in an argon carrier gas could be advantageous to maintain arc stability. Nonetheless, a comprehensive study concerning the influence of the synthesis parameters (such as nitrogen content, quench gas velocity and applied arc current) on the production of TiN nanoparticles remains to be done. Factors potentially affecting arc stability have also not been fully explored.

3 Fundamentals

In this chapter, fundamental theories relevant to the thesis are presented. The chapter is divided into two sections: (1) the synthesis mechanisms of nanoparticles in the gas phase and (2) measurement methods for characterizing the produced nanoparticles and thin films. Given the expansive scope of topics related to the synthesis mechanisms of nanoparticles in the gas phase and the characterization of nanoparticles and thin films, only the major parts pertinent to this thesis are highlighted.

3.1 Nanoparticle formation in the gas phase

The formation and growth of aerosol nanoparticles via arc discharge are based on the principal method of evaporation-condensation. In an evaporation-condensation reactor, a solid bulk material, typically metal, is converted into metal vapors using various techniques, including plasma, laser, sputtering, and heating. When these hot metal vapors mix with the cooler gas flow, the formation and growth of aerosol particles occur. The synthesis of particles with specific properties hinges on both the properties of the aerosol precursor and the conditions within the reactor process. The most critical of these conditions usually relate to the aerosol volume concentration (volume of particles per unit volume of gas) and the time-temperature evolution in the system. Mechanisms for particle formation and growth in the gas phase are generally based on a sequence of steps, presumed to occur in the following order. However, some of these processes may occur simultaneously. Figure **3-1** shows a schematic of the nanoparticle formation process in the gas phase.

Step 1: generating atoms/molecules (i.e., monomers) in the gas phase, where solid or liquid targets are “vaporized” using different techniques: plasma, heating, laser, sputtering, etc.;
Step 2: homogeneous nucleation, leading to the formation of a cloud of stable nuclei;
Step 3: condensation (i.e., heterogeneous nucleation), leading to the formation and growth of nanoparticles considered as “stable” (primary particles);
Step 4: coalescence (i.e., sintering), leading to the formation of “aggregates”;
Step 5: coagulation, leading to the formation of fractal-like agglomerate structures form.

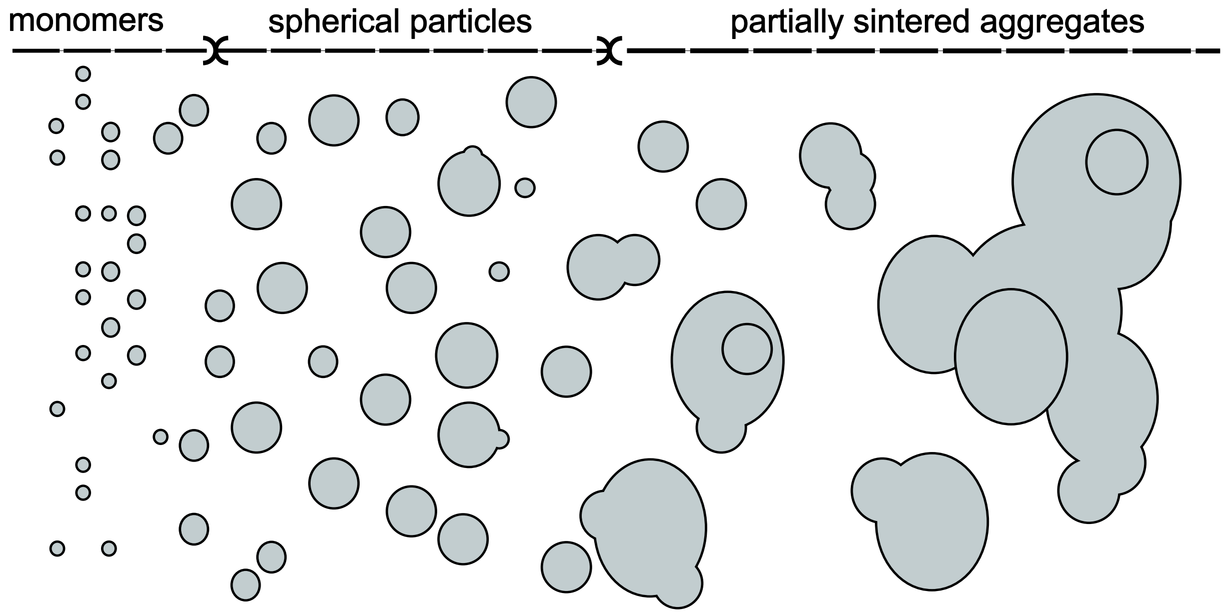

Figure **3-1**: Schematic representation of the particle formation and growth process in the gas phase, adapted from Kruis et al. [104].

3.1.1 Homogeneous nucleation

Nucleation and growth represent typical phase transitions, such as the transition from gas to solid or gas to liquid. The formation of nanoparticles in the gas phase can be explained by the classical nucleation theory (CNT). The CNT is derived from the liquid droplet model. It primarily focuses on the condensation of vapor to a liquid but can also be extended to other liquid-solid equilibrium systems such as crystallization from melts and solutions. Particle formation through homogeneous nucleation arises from a change in the free energy ΔG of the system. The change in the free energy during the cluster formation is composed of two terms: one related to the volume of the emerging cluster and another one related to the contribution of the surface. Consequently, the change in free energy ΔG (Equation 3-3) is the combined result of the change in free energy due to the formation of a new volume G_v (Equation 3-1) and a new surface G_s (Equation 3-2):

$$\Delta G_\mathrm{v} = \frac{4\pi r^3}{3V_\mathrm{m}}(-\mathrm{k_B} T \ln S) \tag{3-1}$$

$$\Delta G_\mathrm{s} = 4\pi r^2 \gamma \tag{3-2}$$

$$\Delta G = \Delta G_\mathrm{v} + \Delta G_\mathrm{s} \tag{3-3}$$

where r is the radius of a formed cluster, V_m is the volume of a single atom, $\mathrm{k_B}$ is the Boltzmann constant, T is the temperature, γ is the specific surface energy of the interface between the drop and the surrounding vapor, and S is the vapor supersaturation ratio. The

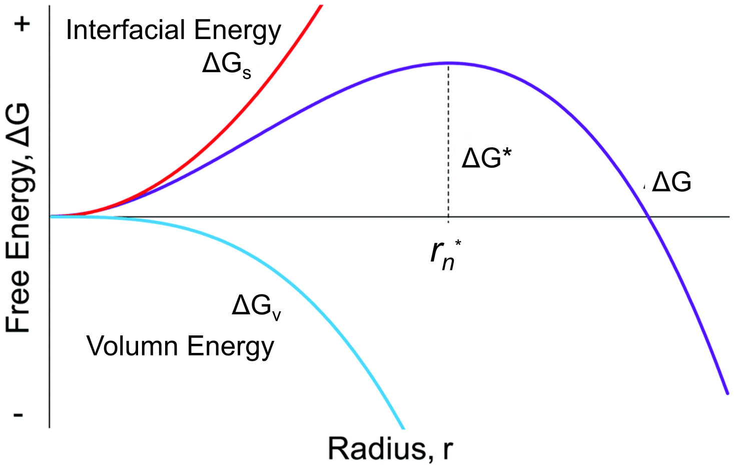

Figure **3-2**: Schematic representation showing the dependence of the nucleation barrier on the radius r according to classical nucleation theory, adapted from Whitehead et al. [204].

saturation ratio S is described by the proportion of the system pressure p to the material-dependent saturated vapor pressure p_s at a given temperature T:

$$S = \frac{p}{p_\mathrm{s}(T)} \tag{3-4}$$

For the nuclei with a smaller radius r, the term G_s is dominant, implying that creating a new surface leads to an increase in ΔG. On the other hand, when the nucleus has a larger radius, the term G_v becomes dominant, leading to a decrease in ΔG. This indicates that nucleation into larger particles is favorable. As illustrated in Figure **3-2**, these two terms relate differently to r. Consequently, the free energy G_s reaches a maximum value ΔG^* at a critical cluster radius ${r_n}^*$, which can be interpreted as the activation energy for nucleation. The critical cluster radius can be derived from the Kelvin equation (Equation 3-5):

$${r_n}^* = \frac{2\gamma V_\mathrm{m}}{\mathrm{k_B} T \ln S} \tag{3-5}$$

Here, V_m represents the atomic volume. Clusters larger than ${r_n}^*$ tend to decrease their free energy further and transform into stable nuclei. Additionally, the critical free energy barrier, ΔG^*, can be determined using the equation below (Equation 3-6):

$$\Delta G^* = \frac{16\pi\gamma^3 V_\mathrm{m}^2}{3\mathrm{k_B^2} T^2 (\ln S)^2} \tag{3-6}$$

During homogeneous nucleation, the key parameters are the formation free energy of the cluster, the cluster size, and the nucleation rate. The size of the critical nucleus has been approximated by various authors through experimental and simulated studies. Typically, the number of atoms/molecules (i.e., monomers) comprising the critical nuclei falls in the range of 10 to 1000 monomers [204, 81].

3.1.2 Heterogeneous condensation

Heterogeneous condensation, also known as nucleated condensation, involves the condensation on pre-existing particles without forming new nuclei. The existing stable nuclei can provide a passive site for the condensation of supersaturated vapor, allowing them to grow. While homogeneous nucleation typically requires saturation ratios of 2–10, heterogeneous condensation can occur at supersaturation ratios of just a few percent. When high concentrations of particles are present, and supersaturation ratios are low, heterogeneous condensation can occur alongside homogeneous nucleation. The rate of heterogeneous condensation depends on the exchange of matter and heat between the particles and the continuous phase [62, 40].

3.1.3 Growth by condensation

When a stable nucleus forms, it has surpassed a threshold (the critical free energy barrier) and will grow through condensation. The growth rate $\frac{\mathrm{d}v}{\mathrm{d}t}$ depends on the saturation ratio, particle size, and particle size relative to the gas mean free path. When particles are much smaller than the gas mean free path ($d_\mathrm{p} \ll \lambda_g$) or in the free molecular range, the particle growth rate is governed by the rate of random molecular collisions between the particle and vapor species. The kinetic theory can be employed to derive the growth rate. However, in the continuum range ($d_\mathrm{p} \gg \lambda_g$), where the particle size d_p is significantly larger than the mean free path λ_g of the suspending gas, the particle growth rate can be determined using thermal diffusion theory, also called Brownian motion (Equation 3-7).

$$\frac{\mathrm{d}v}{\mathrm{d}t} = \frac{2\pi D d_\mathrm{p} V_\mathrm{m}}{\mathrm{k_B} T}(p - p_\mathrm{d}) \tag{3-7}$$

Here, D represents the diffusion coefficient of the condensing species, V_m is the atomic volume of that species, and p_d is the equilibrium vapor pressure above a droplet of diameter d_p [40].

3.1.4 Coagulation and sintering

Coagulation of aerosols takes place when aerosol particles collide because of their relative motion and subsequently adhere, forming larger particles. The theory of coagulation explains how the number concentration of particles and their size evolve as a function of time. As particles collide and coagulate, the total number of particles decreases, and the average

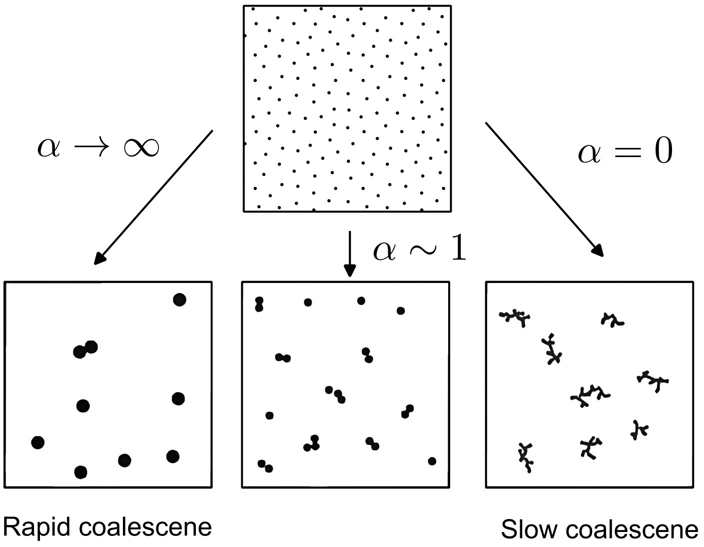

Figure **3-3**: The dimensionless parameter α is the ratio of the average time between collisions τ_c to the time required for coalescence τ_f. For $\alpha \to 0$ ($\tau_\mathrm{f} \gg \tau_\mathrm{c}$), the time between collisions is very short compared with the time for coalescence and fractal-like particles form. For $\alpha \to \infty$ ($\tau_\mathrm{f} \ll \tau_\mathrm{c}$), the particles coalesce as fast as they collide and remain spherical. Adapted from Friedlander [40].

particle size increases. The coagulation rate, in terms of the change in number concentration N can be described as,

$$\frac{\mathrm{d}N}{\mathrm{d}t} = -\frac{\beta}{2}N^2 \tag{3-8}$$

with β being the collision frequency function between two particles or agglomerates described by a fractal-like structure. The frequency function for collisions is influenced by the sizes of the colliding particles, the gas properties (including temperature and pressure), and the characteristics of the flow field. Nonetheless, providing an exact description of the coagulation rate is very complicated, especially for polydisperse aerosols [62, 40]. Kruis et al. [104] proposed a simplified model that describes the evolution of particle morphology, size, and number concentration due to coagulation and sintering. In this model, variations in the polydispersity of agglomerates and primary particles were not considered.

Figure **3-3** illustrates the effect of characteristic times, namely the coalescence time τ_f and collision time τ_c, on the evolution of particle morphology during the coagulation process. The collision time, τ_c, is defined as the average time between two particle collisions, while the coalescence time, τ_f, refers to the time it takes for two particles to merge after making contact. Usually, a dimensionless parameter α, which is the ratio of the collision time τ_c and the coalescence time τ_f, is used to demonstrate the collision-coalescence process, as displayed in Figure **3-3**. Initially, a cloud of very small stable particles is present. When

τ_f is significantly smaller than τ_c, particles coalesce rapidly upon collision, forming larger particles with spherical shapes. When $\tau_\mathrm{f} \gg \tau_\mathrm{c}$ ($\alpha \rightarrow 0$), colliding particles no longer coalesce effectively, forming fractal-like agglomerates. Within these agglomerates, primary particles are held together by physical forces, such as electrostatic and Van der Waals forces. Situated between these two extremes, aggregates bonded by strong chemical forces emerge. These aggregates possess structures that are intermediate to the fully coalesced spheres and the fractal-like agglomerates [40].

In addition to the coagulation rate, the characteristic time for sintering plays a crucial role in shaping particle morphology. Solid particles in contact may undergo sintering into compact particles via several mechanisms, including surface diffusion, grain boundary diffusion, evaporation-condensation, and lattice diffusion. Each of these sintering mechanisms contributes to the reduction in surface area at different rates. The driving force behind the sintering process is to reduce overall free energy, achieved by decreasing specific surface area and simultaneously forming interparticle bonds. Gas-phase synthesis can produce diverse particle structures, e.g., spheres, rods, wires, agglomerates, aggregates or even core-shell particles. The resulting structures depend on the material properties and specific handling conditions during the synthesis process [62].

3.2 Characterization of synthesized nanoparticles and thin films

Key parameters that determine the behavior and properties of aerosol particles include particle size, size distribution, concentration, shape, and chemical composition. However, due to the complex and non-spherical shapes of solid aerosol particles, defining a universal characteristic size becomes particularly challenging. In aerosol science, the term “equivalent diameter” is employed to assign a size to a particle based on its specific property or behavior within a given system. An equivalent diameter is the diameter of a sphere that shares the same value of a specific physical property as an irregular particle (Figure **3-4**) [7].

For instance, the aerodynamic equivalent diameter refers to the diameter of a sphere having either a density of $1000\,\mathrm{kg/m^3}$ (known as the aerodynamic diameter) or the bulk density of the particle itself (known as the Stokes diameter), which settles under gravity at the same terminal velocity as the particle under study. The aerodynamic diameter is useful for characterizing larger particles, typically those greater than 0.3–0.5 µm, where inertial effects are predominant. In contrast, for extremely small particles, inertia plays a lesser role, and Brownian motion becomes more dominant. In such scenarios, the mobility equivalent diameter is commonly used. The mobility equivalent diameter is defined as the diameter of a spherical particle with the same mobility (defined as the particle velocity resulting from a unit of external force) as the particle being studied. Most instruments designed for particle

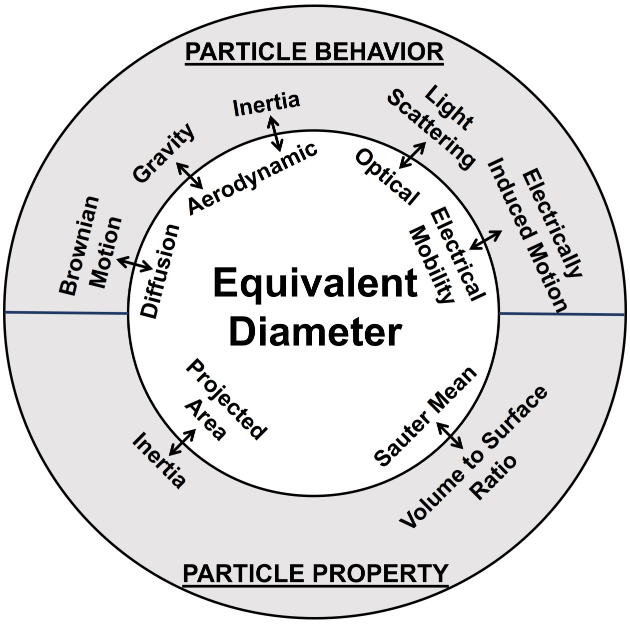

Figure **3-4**: Particle size definitions that depend on observations of particle properties or behavior. Adapted from Kulkarni et al. [7].

measurements are restricted to assess a broad range of particle sizes or multiple particle properties [7]. Thus, selecting the appropriate measurement technique is as crucial as the synthesis process itself.

In this thesis, characterization techniques are organized into two main categories: online and offline characterization. Online characterization enables real-time measurements during the synthesis of nanoparticles, providing immediate insights into the process. Offline characterization, on the other hand, involves the examination of particles after synthesis has been completed, as well as the analysis of the produced thin films. Given that the characterization methods for thin films closely align with those for nanoparticles—encompassing evaluations of purity, microstructure, and morphology—similar characterization instruments were employed throughout this research. It is important to note that this thesis does not address measurements related to the electrical conductivity of copper films. Such measurements utilize standard characterization devices, and as such, their principles of operation are not included in this document. Furthermore, the investigation into the mechanical and tribological properties of titanium nitride composite coatings, carried out in collaboration with Technical University Dortmund (TU Dortmund), is therefore not included within the scope of this thesis.

3.2.1 Online characterization for aerosol particles

While online techniques might offer a limited scope of particle characterization, they can quickly provide critical characteristics of aerosol particles during the synthesis process, such as production rate and particle size distribution. For such online measurements, several commercial devices are available, including the Tapered Element Oscillating Microbalance (TEOM), Scanning Mobility Particle Sizer (SMPS), and Electrical Low-Pressure Impactor (ELPI) are available. The following sections describe the specific online measurement equipment utilized in this thesis.

Dilution system

While standard aerosol instruments such as SMPS, ELPI and TEOM are widely utilized to measure aerosol particles, they are not appropriate for assessing aerosols with high particle number concentrations. The arc discharge reactor used to synthesize nanoparticles was developed for scale-up production and can produce nanoparticles with high number concentrations. Consequently, an aerosol dilution system becomes essential to reduce the particle number concentrations. In this research, a commercial dilution system was chosen to regulate particle number concentrations, since this method was experimentally verified by Helsper et al. [61], and its dilution factor remains unaffected by particle sizes. Figure **3-5** shows the cross-section of the dilution system used in this study. A sheath gas flow Q_{in}, typically composed of compressed air, passes through an annular nozzle enveloping the aerosol inlet suction nozzle. An under-pressure chamber is housed within the dilution system. The low pressure induces a suction of aerosol Q_{a} into the dilution chamber, facilitating a mixture of the two gas flows Q_{in} and Q_{a}. The dilution factor depends on the pre-pressure of Q_{in} and the geometry of the suction nozzle for Q_{a}, which is adjustable by changing the nozzle diameter. The dilution factor is given by the equation $W = \left(Q_{\text{in}} + Q_{\text{a}}\right)/Q_{\text{a}}$. Typically, dilution factors of ten and one hundred are the standards. Moreover, the magnitude of the dilution factor can be further increased by cascading multiple dilution systems.

Scanning Mobility Particle Sizer

Measurements of aerosol particle size distribution based on their electrical mobilities were widely used before the introduction of commercial instruments by the company TSI in the 1960s and 1970s [39]. Scanning mobility particle sizers (SMPS) can monitor the number size distribution of aerosol particles in a size range from 3 to 700 nm. The SMPS setup primarily consists of a pre-impactor, a neutralizer, a differential mobility analyzer (DMA) and a condensation particle counter (CPC). These components are used for pre-separating, charging, classifying, and counting aerosol particles.

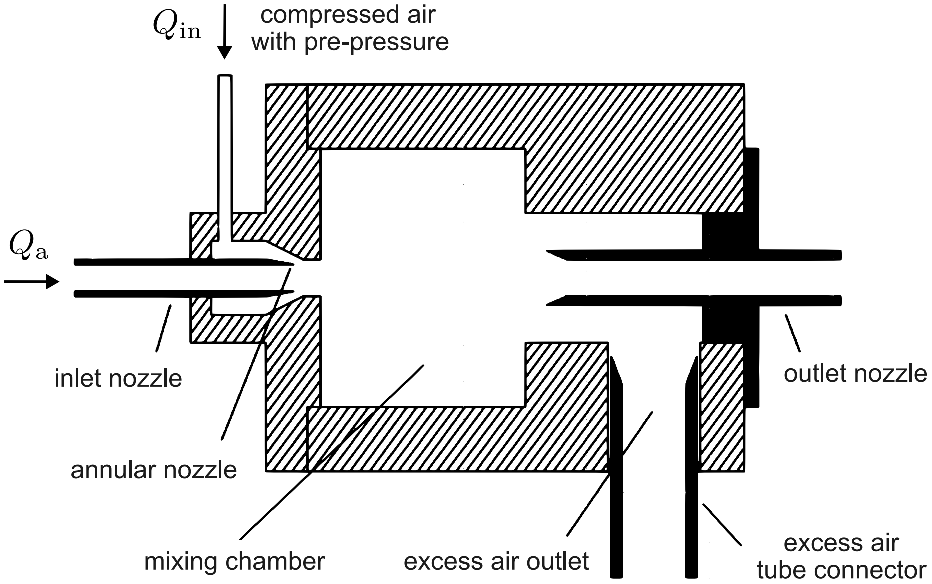

Figure **3-5**: Shematic illustration of functional principle for a commercial dilution system from Palas GmbH (Source: adapted from www.palas.de).

When using a DMA to classify aerosol particles, the particles must be charged and have a defined charge distribution. Therefore, before entering the DMA classifier, the polydisperse aerosol is directed to a neutralizer. Within the neutralizer, a bipolar diffusion charger—employing either a radioactive source or a soft X-ray source—ionizes gas molecules. The resulting bipolar gas ions attach to the particles, producing a bipolar-charged aerosol. The system is designed to ensure the particles attain an equilibrium charge distribution, which is independent of particle chemical composition and morphology [40].

A DMA is designed to select a monodisperse aerosol from a polydisperse aerosol by establishing a defined electrical field within a laminar flow field. In a monodisperse aerosol, all the charged particles possess identical electrical mobility. The fundamental working principle hinges on the fact that the velocity of a charged particle in an electric and a laminar flow field is determined by the size of the particle. When these charged particles in a carrier gas start from the same position, their particle velocity is determined by the balance between the Stokes drag force F_{d} (Equation 3-9) and the electric field force F_e (Equation 3-10)

$$F_{\mathrm{d}} = \frac{3\pi\eta v_{\mathrm{x}} d_{\mathrm{M}}}{C_{\mathrm{c}}} \tag{3-9}$$

$$F_e = neE \tag{3-10}$$

with η representing the gas viscosity, v_{x} being the velocity component of the particle perpendicular to the gas flow, C_{c} as the Cunningham slip correction factor (which depends on

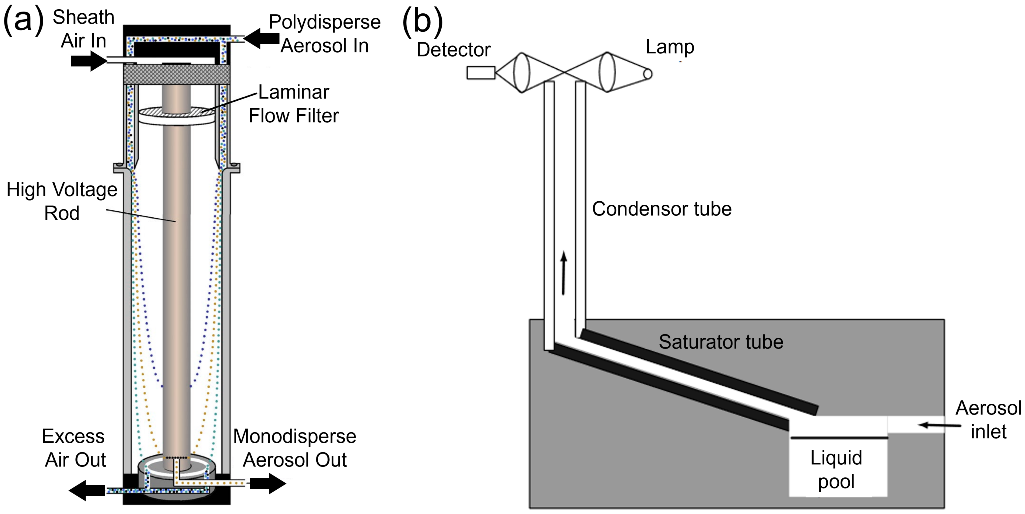

Figure **3-6**: (a) Schematic diagram of a cylindrical version of the DMA and (b) schematic of a condensation particle counter, adapted from TSI (www.tsi.com).

the particle size), n as the number of elementary charges on the particle, e as the elementary charge, E as the electric field, and d_M as the electrical mobility diameter. According to the force balance, one can calculate the electric mobility Z_p (defined as v_x/E, as shown in Equation 3-11).

$$Z_\mathrm{p} = \frac{v_\mathrm{x}}{E} = \frac{neC_\mathrm{c}}{3\pi\eta d_\mathrm{M}} \tag{3-11}$$

Typically, smaller particles exhibit larger electrical mobilities, whereas larger particles have smaller electrical mobilities. Figure **3-6** (a) presents a schematic of a standard DMA in a cylindrical form. The charged polydisperse aerosol flows alongside a co-flowing sheath gas, moving towards an exit slit. Particles with larger electric mobilities travel more rapidly toward the central electrode and adhere to it. Particles with smaller electrical mobilities might be carried away by the excess gas. Only monodisperse aerosol-where particles possess a specific electrical mobility-is expelled from the DMA via the slit at the end of the inner electrode. The specific electrical mobility is determined by the geometry of the DMA, sheath flow rates, and the classifying voltage of the applied DMA device [7]. A CPC device exhibits greater nanoparticle detection efficiency than an optical particle counter. In SMPS measurements, the monodisperse aerosol selected by the DMA is introduced directly into a CPC instrument. As illustrated in Figure **3-6**, the aerosol flow within the CPC instrument is saturated with vapors from a liquid, typically butanol, in a slightly heated saturator. The temperature of this butanol-aerosol mixture then drops in the condenser, causing the vapors to supersaturate and condense onto the nanoparticles. As a result, the particles grow into droplets, and the enlarged particles, ranging in size range from 5 to 15 μm, are readily detectable by an optical counter. Furthermore, combining a DMA with a CPC can significantly reduce the time needed for measurement without compromising the size resolution [7].

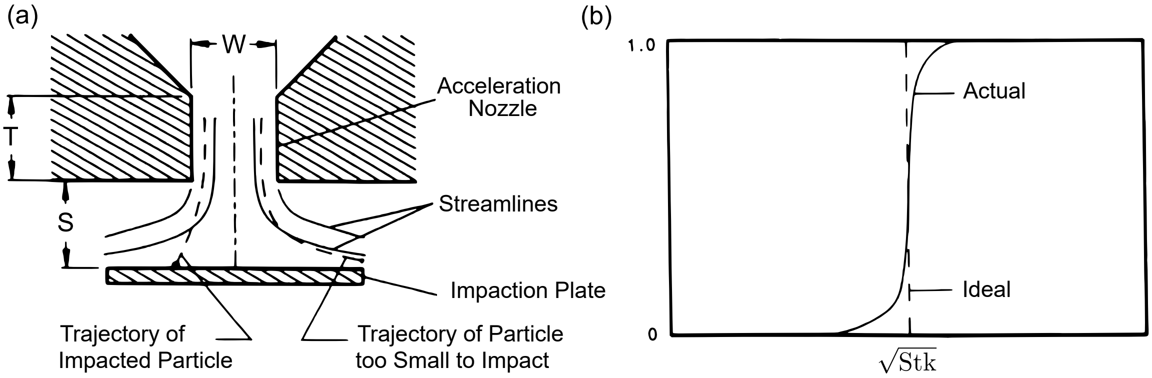

Figure **3-7**: (a) Schematic diagram of the conventional impactor and (b) corresponding particle collection efficiency curves, adapted from Kulkarni et al. [7].

Electrical Low-Pressure Impactor

The electrical low-pressure impactor (ELPI) provides the real-time measurement of size distribution and concentration of aerosol particles within a size range of 6 nm–10 µm. The measured particle number size distribution is based on the aerodynamic or Stokes diameter, given that the principle of inertial classification is used. An ELPI device is made up of three primary parts: a unipolar charger that electrically charges particles, a cascade impactor used for inertia classification, and a multichannel electrometer that records the electric current at each stage of the impactor [7, 76]. Cascade (or multi-stage) impactors allow aerosol particles to be classified and collected based on their inertia. A cascade impactor consists of a series of stages. Each stage has an orifice with successively decreasing gap sizes, directing the aerosol to flow perpendicular to a collecting surface. By altering the direction of the particle-laden gas flow, particle classification becomes achievable. In each stage, particles with less inertia stay within the gas streams and follow the gas streamlines. Large particles, however, do not deviate as much as smaller ones due to their inertia and strike the collector surface.

Figure **3-7** (a) shows a schematic of a conventional one-stage impactor, which consists of a single jet of particle-laden gas streams impinging upon a flat plate. Critical parameters in determining whether an impaction plate will capture a particle include the velocity of the air, the size of the particle, and the dimension of the acceleration nozzle. A dimensionless parameter, the Stokes number Stk, is utilized to estimate whether a particle will impact a collection body or an impaction plate. The Stokes number is defined as the ratio of the stopping distance of a known particle to the physical dimension of the body collector (Equation 3-12).

$$\mathrm{Stk} = \frac{\rho_\mathrm{p} C_\mathrm{c} {d_\mathrm{p}}^2 U}{18 \eta d_\mathrm{b}} \tag{3-12}$$

Where ρ_p is the particle density, C_c is the Cunningham slip correction factor, d_p is the particle diameter, U is the average velocity of the gas flow, d_b is the orifice width or diameter, η is the gas viscosity. The most important characteristic of an impactor is its collection efficiency. The collection efficiency $E_\mathrm{I} = f(\mathrm{Stk})$ is defined as the fraction of particles passing through the nozzle that impact the collecting plate. Efficiency curves for impactors are typically plotted in a general form, as depicted in Figure **3-7** (b). This is because the efficiency curve is directly proportional to the square root of the Stokes number, which in turn is proportional to particle size. The cutoff size of a stage, represented by $d_{\mathrm{S},50}$, typically correlates with the diameter at which the corresponding efficiency of the impactor is 50 % (Equation 3-13). Where the asterisk denotes a value corresponding to 50 % efficiency.

$$d_\mathrm{p}{}^* = \left(\frac{18\eta d_\mathrm{b} Stk^*}{\rho_\mathrm{p} C_\mathrm{c} U}\right)^{1/2} \tag{3-13}$$

As shown in Figure **3-7**, the ideal impactor has a perfectly sharp efficiency curve. This means all particles larger than the cut-size of the impactor are gathered on the plate, while those smaller than the cut-size continue with the gas streams, moving out of the impaction region. However, the efficiency curve, in practice, typically exhibits an S-shape [40, 7, 62].

Aerodynamic Lens System

The basic concept of an aerodynamic focusing lens is similar to that of an impactor, which uses the inertial mismatch between the particles and the carrier gas to separate them. Aerodynamic lenses are designed to form a narrow particle beam by expanding a particle-laden gas stream from a high-pressure reservoir through a nozzle and into a low-pressure chamber. The theory for the design of an aerodynamic lens system (ALS) was first introduced by Liu et al. [123, 124]. Moreover, ALS has been extensively studied and widely used as a sampling device for introducing particles into aerosol mass spectrometers (AMS) for single-particle chemical analysis. Wang and McMurry [202, 201] developed a design and evaluation tool, known as the Aerodynamic Lens Calculator, to eliminate the need for time-consuming calculations.

An aerodynamic lens system typically consists of three main components: an inlet orifice, a series of focusing orifices, and an acceleration orifice. The inlet orifice acts as a critical orifice, regulating the total mass flow rate into the ALS. Following this is a sequence of thin plate-focusing orifices that allow particles with a specific Stokes number to be focused near the centerline of the flow. An important parameter here is the particle contraction factor (η_c), which is the ratio of the final to initial radial positions of the particles traveling through the lens. This contraction factor η_c strongly depends on the Stokes number (Stk). Aerodynamic lenses are most effective in focusing particles with a Stokes number close to one. Figure **3-8** shows a schematic of particle trajectories in an ALS with different Stokes numbers. Considering the radial position of the particle before and after the lens, particles with an optimal Stk close to 1 will be brought very close to the centerline of the flow, as illustrated in Figure **3-8** (b). Particles with a Stk less than this optimum will move closer to

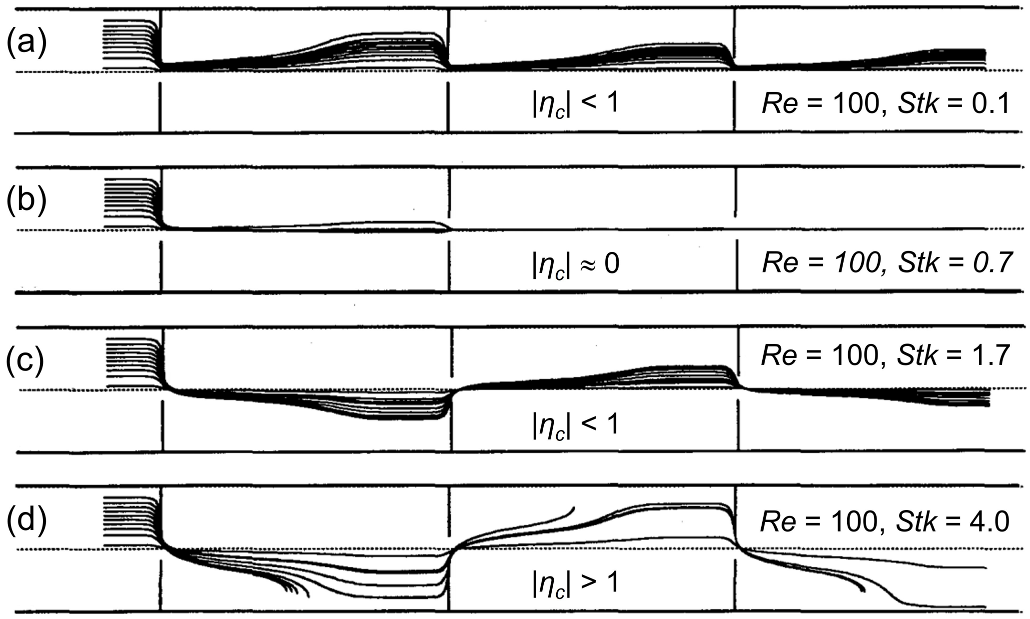

Figure **3-8**: Numerical calculations illustrating the motion of particles in a three-lens system, (a-d): particle trajectories for Stokes number (Stk) = 0.1, 0.7, 1.7, and 4.0 respectively, while the Reynolds number (Re) of the gas flow is constraint to 100, adapted from Liu et al. [123].

the centerline but not as centrally as the optimal ones (see Figure **3-8** (a)). Particles with a Stk greater than the optimum will cross the centerline (see Figure **3-8** (c)). If their Stk is excessively large, these particles will be defocused. This means that their axial position will deviate further from the centerline than their initial position (as seen in Figure **3-8** (d)). The final component of the system is the acceleration nozzle which is also a critical orifice. This accelerating nozzle determines the pressures within the lens system and accelerates the focused particles to velocities near the speed of sound. If the particles are sufficiently focused as they exit the nozzle, they separate from the gas phase and then enter a high vacuum chamber. In particular, the particle transmission efficiency of a well-designed ALS can be significantly improved over that of the capillary and nozzle technology [7].

Based on the work of Wang and McMurry [202], the design of an aerodynamic lens assembly is fundamentally controlled by principles of particle dynamics and fluid mechanics principles. When using sharp and flat orifices to focus particles, an optimal Stokes number is close to 1. The diameter, D_f, that focuses a particle with a Stokes diameter, D_p, in a focusing orifice of the lens assembly is expressed as

$$D_\mathrm{f} = \left(\frac{2\rho_\mathrm{p} d_\mathrm{p}^2 C_\mathrm{c} \dot{m}}{9\pi \rho_\mathrm{g} \eta \mathrm{Stk}} \right)^{1/3} \tag{3-14}$$

where ρ_p and ρ_g are the particles and upstream gas densities, respectively. C_c is the slip

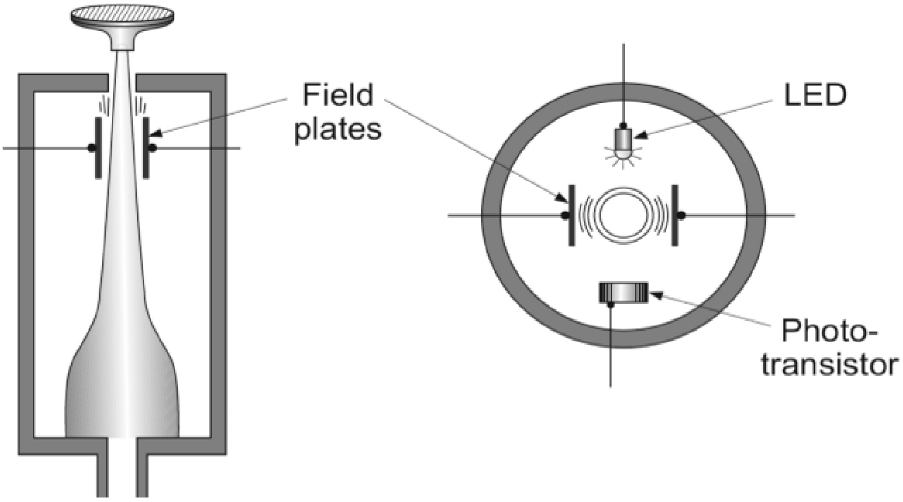

Figure **3-9**: Internal features of Tapered Element Oscillating Microbalance, adapted from Kulkarni et al. [7].

correction factor, $\dot{m}$ is the gas mass flow rate through the lens assembly and η is the gas viscosity. In addition, the Reynolds number Re should be kept low enough to ensure that the flow reattaches soon after the lens and does not become turbulent. The design tool by Aerodynamic Lens Calculator recommends keeping Re below 200.

$$Re = \frac{\dot{m}}{\pi \eta D_{\mathrm{f}}} < 200 \tag{3-15}$$

Despite concerns about turbulence, *Re* plays a crucial role in other lens design considerations, such as pressure drop across an orifice and the spacing between individual lenses. For a detailed insight into the calculation related to the inner diameter and length of the spacers between two lenses, and operating parameters like flow rate, pressure, and carrier gas, one can refer to the comprehensive study by Wang and McMurry [201, 203, 202].

Tapered Element Oscillating Microbalance

A Tapered Element Oscillating Microbalance (TEOM) instrument works by collecting aerosol particles on a vibrating filter. As the particle accumulates on the filter, the oscillation frequency of the filter changes, which is then used to derive the mass concentration of the aerosol. Figure **3-9** depicts the typical arrangement for a TEOM instrument. At the heart of the TEOM system is a specially tapered hollow tube constructed of an elastic, glass-like material. The narrow end (or tip) of the tube vibrates at its natural frequency. A replaceable collection medium, such as a filter, is affixed to the tip. The wide end of the tube is firmly anchored to a relatively massive base plate. When the particle-laden gas flows are drawn through the hollow tube, the particles deposit on the filter. The filtered gas is then drawn through the hollow tube, which is typically controlled by an automatic mass flow controller. The accumulating particles cause the mass increase and, thus, the decrease in the vibration frequency of the tapered element. An electronic feedback system initiates and maintains the oscillation of the tapered element at constant amplitude. A light-emitting diode (LED)-phototransistor pair, oriented perpendicular to the plane of oscillation, detects the oscillation frequency of the tapered element. The light-blocking effect of the oscillating element modulates the phototransistor's output signal, which is then amplified and recorded. For a known system, the change in frequency is stored in memory and can be converted to determine the mass loading of the filter (Equation 3-16).

$$\Delta m = K_0(\frac{1}{f_b^2} - \frac{1}{f_a^2}) \tag{3-16}$$

where Δm is the mass of the collected particles, f_b is the frequency of the oscillating element after sampling, f_a is the frequency before sampling and K_0 is a constant to each tapered element which is derived from the equations of motion for a simple harmonic oscillator [7]. While this expression for Δm is nonlinear, it is monotonic. It is independent of previous mass loading and relies only on the constant K_0 For subsequent measurements, f_b evolves into f_a. After sampling, the new f_b will differ from f_a due to the additional mass accumulated on the filter. Nevertheless, some factors such as adherence effects, overloading, electrostatic effects, and volatilization losses, can introduce biases when using TEOM to monitor particle mass concentration. For instance, plasma–synthesized particles carrying electrical charges might cause a decline in the oscillation frequency of the tapered element. This declination is attributed to the accumulated electrical charge on the TEOM filter. Implementing a bipolar charger before the TEOM can significantly mitigate this interference [7].

3.2.2 Offline characterization for nanoparticles and thin films

To obtain comprehensive particle information–including size, shape, phase, and chemical composition of individual (primary) particles–, offline measurements are often used. These offline techniques involve depositing particles on a substrate or filter for subsequent analysis. Typical techniques for characterizing collected aerosol particles, such as electron microscopy, X-ray diffraction analysis, and Brunauer-Emmett-Teller (BET) measurements, are described in this section.

Brunauer-Emmett-Teller measurement

The BET gas adsorption is employed to determine the surface area of nanomaterials [151]. The BET instrument was developed to measure the specific surface area (SSA) of dried powder samples. SSA is defined as the surface area of a material divided by its mass (m^2/g). Therefore, the measured specific surface area can be utilized to estimate the primary particle size of agglomerated particles by Equation 3-17: provided the density of the bulk material is known:

$$\mathrm{SSA} = \frac{6}{\rho_\mathrm{p} d_\mathrm{prim}} \tag{3-17}$$

Here, ρ_p is the density of the particles, SSA is the specific surface area, and d_prim represents the BET primary diameter of spherical particles, respectively. While the Langmuir theory emphasizes the monolayer adsorption of gas molecules (or adsorbates) onto solid surfaces caused by chemisorption, the BET theory extends this concept to multilayer physisorption. In BET analysis, nitrogen is the most employed gaseous adsorbate due to its availability in high purity and its strong affinity with most solid powders. Consequently, standard BET analysis is performed at the boiling temperature of N_2 (77 K), to ensure detectable adsorption levels. During the adsorption process, precise pressure transducers are used to monitor the pressure changes. The collected data are represented as a BET isotherm, illustrating the quantity of gas molecules adsorbed in relation to the relative pressure. The associated BET equation is presented in Equation 3-18:

$$\frac{p_\mathrm{e}}{V_0(p_0 - p)} = \frac{1}{hV_\mathrm{0m}} + \frac{h-1}{hV_\mathrm{0m}} \left(\frac{p_\mathrm{e}}{p_0}\right) \tag{3-18}$$

where p_e and p_0 indicate the equilibrium and saturation pressure of adsorbates at the temperature of absorption, respectively. V_0 is the volume of the adsorbed gas per gram of adsorbent, and V_0m is the volume of monolayer adsorbed gas per gram adsorbent. h is the BET constant, depending on the heat of adsorption and condensation. A characteristic BET isotherm has a linear behavior within the range of $0.05 \leq p_\mathrm{e}/p_0 \leq 0.35$. Within this range, the value of the slope $(h\text{-}1)/(hV_\mathrm{0m})$ and the y-intercept $1/V_\mathrm{0m}$ are determinable and enable the calculation of the specific surface area [14, 50].

X-ray Diffraction

X-ray diffraction (XRD) is a standard, non-destructive analytical technique used to determine structural characteristics such as phase composition, crystal structure, and orientation in powder or film samples. As illustrated in Figure **3-10**, an X-ray instrument comprises three main components: an X-ray source, a sample holder (or stage), and an XRD detector. In XRD, the generated X-rays are collimated and directed onto a material sample, where the interaction of the incident X-rays with the crystalline sample produces a diffracted wave, which is then detected, processed, and counted. The detected X-ray diffraction is the result of constructive interference between X-rays and a crystalline sample. The wavelength of the X-rays used is comparable to the distance between the atoms in a crystalline lattice. This results in a diffraction pattern that can be analyzed in several ways, the most popular being by applying Bragg's Law (equation 3-19)

$$n\lambda = 2d_{hkl} \sin\theta_{hkl} \tag{3-19}$$

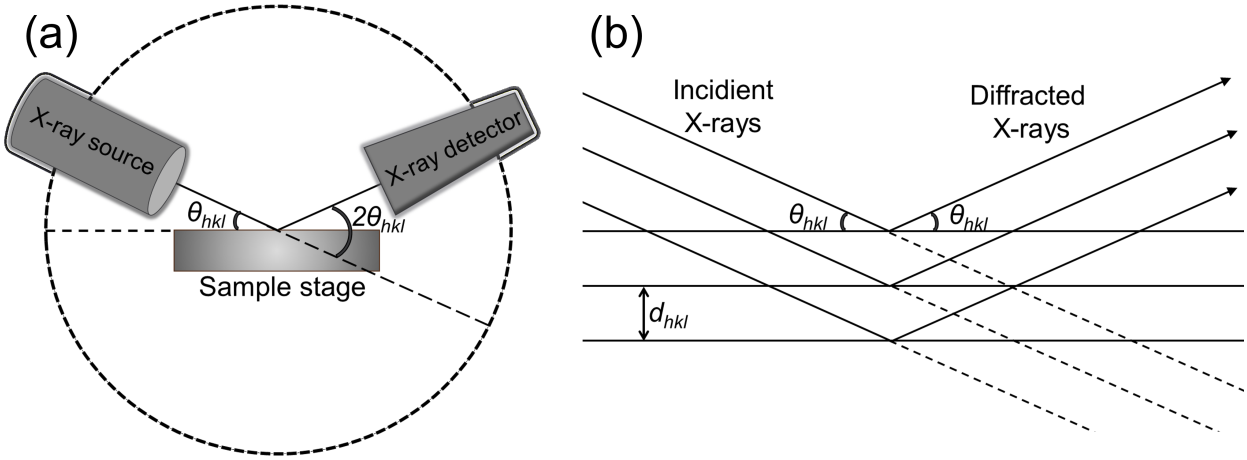

Figure **3-10**: (a) Basic parts and principal of a diffractometer, (b) Principal of X-Ray diffraction and Bragg's law, adapted from Epp [34].

Where λ is the wavelength of the beam, n represents any integer, d_{hkl} is the spacing between diffracting planes, θ_{hkl} is the incident angle. The intensities of X-ray diffraction are determined by the atomic positions within the lattice planes. Therefore, the X-ray diffraction pattern may serve as a fingerprint for periodic atomic arrangements, offering information on the material composition of a given sample. Moreover, diffractograms can reveal details about the crystallite size, when the Scherrer equation is employed. The Scherrer equation relates the widths of the diffraction peaks to the size of crystallites [209, 98].

Electron Microscopy

Electron microscopes, both scanning and transmission, enable the examination of particle size and shape at the nanoscale, significantly smaller than the resolution limit of optical microscopes. According to diffraction theory, this resolution limit is controlled by the wavelength of the electron beam and the characteristics of the objective lens (equation 3-20).

$$l_{\mathrm{res}} = \frac{0.61\lambda_{\mathrm{e}}}{m \sin\theta_{\mathrm{r}}} \tag{3-20}$$

Where λ_{e} is the wavelength of accelerated electrons, which is related to the acceleration voltage and electron wavelength. m is the refractive index of the viewing medium between the objective and the sample (for electrons in vacuum, $\mathrm{m} = 1$), and θ_{r} is the angular aperture. To achieve maximum resolution, λ_{e} should be minimized, and m and θ_{r} should be maximized. The wavelength of the electron beam used in electron microscopes is significantly shorter than that of the light used in optical microscopes. Therefore, scanning electron microscopy (SEM) and transmission electron microscopy (TEM) are commonly used to measure the

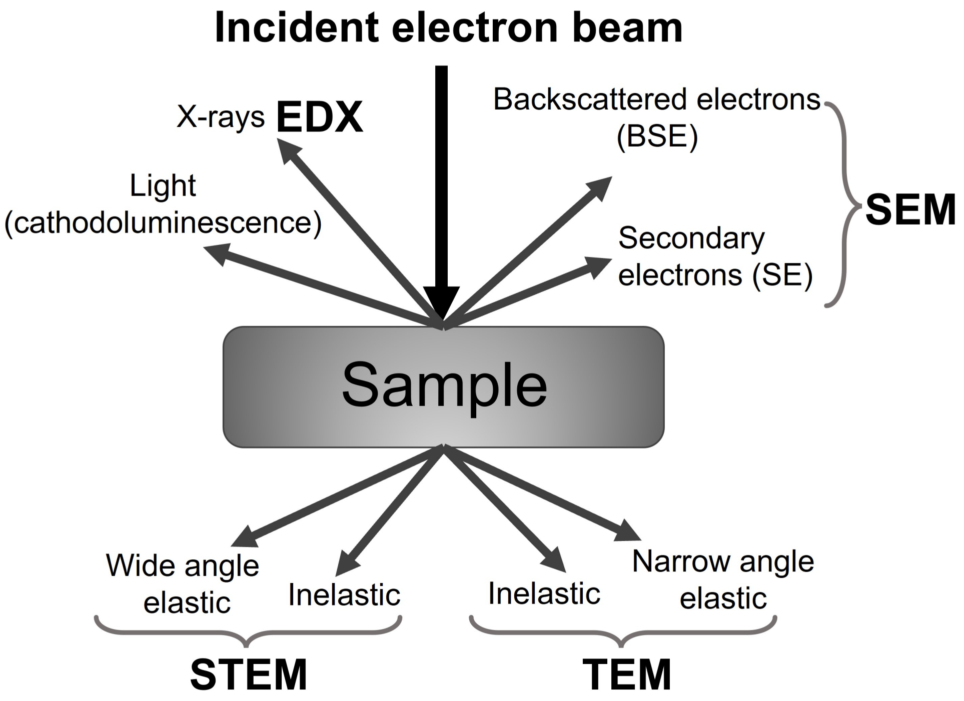

Figure **3-11**: A schematic of phenomena taking place during the incidence of the electron beams, adapted from Stokes [182].

size of nano- and microparticles, examine their microstructure, and, together with energy-dispersive spectroscopy, quantify the elements present in a sample [97].

Figure **3-11** illustrates a schematic of the working principle of an electron beam instrument. The source of the electron beam typically originates from a thermionic emitter, where electrons are extracted from a heated filament (made of tungsten or LaB_6) by a strong electrical field. Once emitted, the electrons are formed into a beam and focused onto the sample with the help of an electromagnetic lens system. As the electron beam interacts with the sample, it causes the scattering of the beam electrons and the ejection of both electrons and X-ray photons from the atoms of the specimen. Modern electronic microscopes are equipped with a range of detectors and collectors, used to capture the scattered or emitted electrons. With a specialized electron imaging system, electron images are formed with essential particle information. It is important to note that electron microscope analysis is carried out in high vacuum conditions. Thus, they are only suitable for materials that do not evaporate or degrade when exposed to a vacuum and an electron beam.

In TEM, a high-energy electron beam (100–400 keV) illuminates the sample situated in a grid holder. These electrons penetrate the sample and are detected by an electron detector located below the sample holder. The TEM image is formed by the electrons that travel through the sample. Typically, the resolution limit of TEM is less than 1 nm, making it ideal for imaging small particles or thin films less than 0.5 µm. In SEM, the electron beam (with energies $< 30\,\mathrm{keV}$) is focused onto a specific area of the sample and scanned across it in a regular pattern. The electron beam causes the emission of both secondary and backscattered electrons from the surface of the sample. Electron detectors, typically positioned above the sample holder, capture these emitted electrons to generate an SEM image. Notably, these SEM images have a three-dimensional appearance since the number of emitted electrons that reach the detector is influenced by the topography of the sample surface. In modern SEM instruments, a resolution down to about 1 nm is accessible, offering detailed insights into powders and films ranging from nanoscale to microscale [62, 7, 97].

Electrical Resistivity of Thin Films

To measure the electrical resistivity of sintered copper films, several techniques are employed: spin coating for preparing the thin film, a stylus profilometer for measuring film thickness, and the four-point probe method for determining sheet resistance.

In the spin coating process, a small amount of dispersion is deposited onto the center of the substrate, typically using a pipette to dispense a known volume of liquid. The substrate is then accelerated to a preset rotational speed, causing the liquid to spread to the edges due to centrifugal force, forming a thin film on the surface. The film thickness continues to decrease until disjoining pressure effects cause it to reach an equilibrium. The final film thickness depends on the properties of the applied liquid such as viscosity, drying rate, surface tension, and solid loading [59, 38].

A stylus profiler can measure surface features ranging from 10 nm to 1 µm in height. The instrument's lateral resolution is determined by the tip's radius of curvature, which ranges from 0.02 to 50 µm, while the horizontal resolution depends on the scan speed and data sampling rate. The stylus profiler moves a small-tipped probe across the sample surface, recording height variations. The vertical motion of the stylus is typically detected by a linear variable differential transformer (LVDT), which converts this signal into height data. The stylus's lateral movement, including distance and speed, is preset through an operation program, allowing simultaneous acquisition of the surface height profile [108].

The four-point probe method measures the conductivity or resistivity of thin films or layered materials. This method typically uses four collinear probes spaced 1 mm apart, with tungsten metal tips. A high-impedance current source supplies current through the outer two probes, while the inner two probes detect the voltage drop using a voltmeter. Separating the current and voltage electrodes eliminates contact resistance and additional voltage drops, ensuring accurate sheet resistance measurements [83]. During the measurement, the four tips are pressed onto the conductive layer, and the sheet resistance is calculated by the program.

Sheet resistance refers to the resistance of thin films that are uniform in thickness and is defined as:

$$R_{\mathrm{sq}} = \frac{\rho}{t} \tag{3-21}$$

where t is the film thickness, and R_{sq} is the sheet resistance ($\Omega/\square$), directly measured by the four-point probe method. For films in printed electronics, sheet resistance measurement is most commonly used. Volume resistivity can be calculated as follows:

$$\rho = \frac{\pi}{\ln 2} \times \frac{V}{I} \times t \times k \tag{3-22}$$

where ρ is the volume resistivity, V is the measured voltage, I is the source current, t is the sample thickness, and k is a correction factor based on the ratio of the probe to the wafer diameter and the ratio of wafer thickness to probe separation. The correction factors can be found in standard four-point probe resistivity test procedures [176].

4 Arc discharge synthesis of nanoparticles

This chapter outlines the study of continuous optimization in an arc discharge reactor, initially developed during the European BUONAPART-E project (Better Upscaling and Optimization of the Production of Nanoparticles and Nanostructures through Electrical Discharge) from 2012 to 2016. The aim of this European BUONAPART-E project was to synthesize metal nanoparticles with high efficiency and purity. The focus of this research is the synthesis of nanoparticles with specific properties from different materials, including metal (copper, Cu) and ceramic (titanium nitride, TiN), to meet diverse application requirements. The investigation detailed the effects of several process parameters, such as applied current, gas composition, and quench gas rate, on the productivity and primary particle size of copper and titanium nitride nanoparticles. Most parts of this chapter have been published in peer-reviewed journals [41, 43].

4.1 Synthesis of copper nanoparticles (Cu NPs)

Copper nanoparticles (NPs) are considered a promising alternative to silver and gold NPs in the preparation of conductive inks, owing to their high electrical conductivity and significantly lower cost compared to silver and gold. The development of the arc discharge reactor used for synthesizing copper nanoparticles has been previously reported by Stein et al. [180, 179]. This section primarily explores the trade-off between particle yield and size. Additionally, the composition and morphology of the synthesized copper nanoparticles were analyzed and discussed in detail.

4.1.1 Experimental details

Various configurations and process parameters of the arc reactor for metal nanoparticle synthesis have been discussed in detail in the previous work by Stein et al. [180, 179]. Briefly, the arc reactor chamber heats and vaporizes bulk copper granules in a crucible through thermal plasma, transforming them into copper vapor. The generated copper atoms are then rapidly cooled by a flow of inert gas, triggering sequential processes such as nucleation,

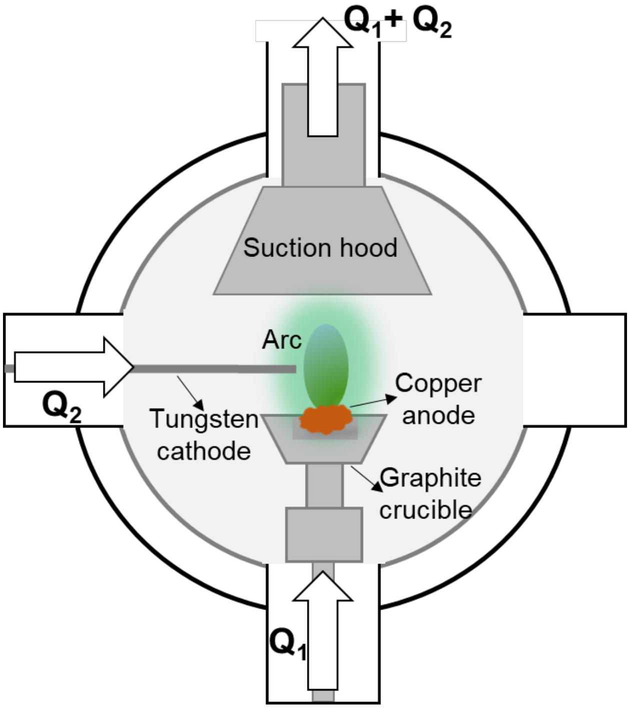

Figure **4-1**: Detailed schematic illustration of the reactor chamber utilized in this work for the synthesis of copper nanoparticles. Reproduced from Fu et al. [43], with permission from Nanotechnology (Copyright 2020).

condensation, and coagulation, resulting in the formation of copper nanoparticles. In this work, the arc reactor with the crucible design 7 from Stein et al. [180], as illustrated in Figure **4-1**, was chosen due to its efficiency in producing the highest rates and smallest sizes of primary copper nanoparticles. Furthermore, the nitrogen arc was selected for its significantly higher production rate compared to other arcs (Ar, He, N_2 mixed with H_2), using N_2 with a purity of at least 99.9995 % as the carrier gas.

As depicted in Figure **4-1**, two gas flows enter the reactor: a main carrier gas flow Q_1 and a cross gas flow (quench gas flow) Q_2. The arc is ignited between the electrode pair in the reactor chamber. The tungsten cathode (WL-15 gold, 98.5 % tungsten and 1.5 % lanthanum oxide) is a rod with a diameter of 1.6 mm, while the anode is a graphite crucible filled with the desired material (copper shot, 0.8–2 mm, 99.5 %, Alfa Aesar, USA). Variations in gas flows Q_1, Q_2, and the applied current were used to obtain copper particles with differing production rates and particle sizes. The specific production parameters employed in this work for obtaining copper nanoparticles will be discussed in Section 4.1.2. The particles produced were directly collected from a filter (PE filter with a PTFE membrane, R&B Filter GmbH, Langenbrettach, Germany) and stored in plastic vials. This collection process was conducted in ambient air, and the vials were stored under the same conditions.

Characterization of the collected copper nanoparticles was conducted using a BET analyzer (Brunauer–Emmett–Teller analyzer, Gemini VII 2390a, Micromeritics Instruments Corporation, GA, USA), which measured the specific surface area to estimate the average primary particle size (BET size) of the copper particles. The microstructure of these nanoparticles was investigated using a Scanning Electron Microscope (SEM, JSM 7500F, Jeol, Tokyo, Japan) with a Secondary Electron (SE) detector. For further analysis, freshly produced Cu NPs underwent examination through a transmission electron microscope (TEM, JEM-2200FS, Jeol, Tokyo, Japan). The elemental composition of the copper nanoparticles was determined using the aforementioned SEM equipped with an Energy-Dispersive X-ray (EDX) spectroscopy system (Quantax, Bruker Nano GmbH, Germany), operating at 10 kV. To ascertain the crystal phases of the copper nanoparticles, X-ray Diffraction (XRD) measurements were carried out using an X-ray diffractometer (type D8 Advance, Bruker, USA), fitted with Cu-Kα radiation at a wavelength of 1.5406 $\mathring{A}$. Utilizing Rietveld refinement with MAUD (Materials Analysis Using Diffraction), the crystal phases of copper nanoparticles were identified, and their average crystallite size could be estimated.

4.1.2 Production and characterization of copper nanoparticles

Variations in production parameters, such as applied current and gas flows, have been employed to investigate the relationship between the production rate and the primary particle size of copper nanoparticles, as illustrated in Figure **4-2**. Depending on these parameters, copper nanoparticles can be synthesized continuously at a rate of 1.2 to 5.5 g/h, while keeping their Brunauer–Emmett–Teller (BET) sizes below 100 nm. The presented production rate is calculated based on the copper powders collected from the filter, not the evaporation rate of copper granules. It has been noted that a larger primary particle size in copper nanoparticles is associated with a higher production rate. In this work, with a fixed electrode distance of approximately 3 mm, the power input of the arc is theoretically proportional to the applied current. Therefore, increasing the applied current enhances the energy delivered to the feedstock material in the graphite crucible, thereby boosting the evaporation rate of the feedstock material. This heightened evaporation rate not only increases the production rate but also significantly enlarges the size of the nanoparticles. This finding is consistent with the results reported by Mahoney et al. [129], who observed larger primary particles and a wider agglomerate size distribution at higher evaporation rates. For example, the production rate for primary particles of 50 nm is four times lower than that for 65 nm particles. Generally, smaller particles have the benefit of requiring lower sintering temperatures. Given the practical requirement for a sufficient mass of Cu samples, copper nanoparticles with a BET size smaller than 60 nm were selected for the development of copper inks in this research.

Figure **4-3** presents transmission electron microscopy (TEM) images of copper nanoparti-

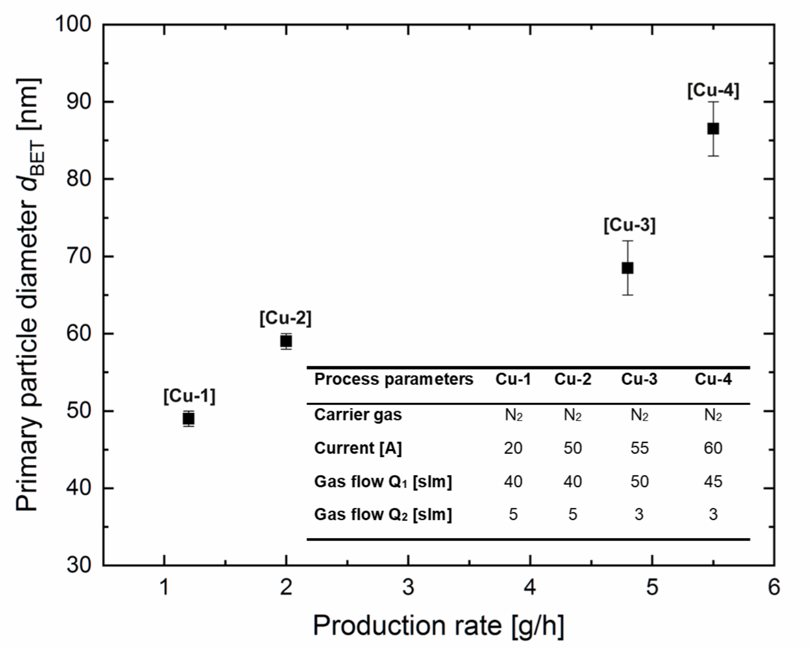

Process parameters	Cu-1	Cu-2	Cu-3	Cu-4
Carrier gas	N_2	N_2	N_2	N_2
Current [A]	20	50	55	60
Gas flow Q_1 [slm]	40	40	50	45
Gas flow Q_2 [slm]	5	5	3	3

Figure **4-2**: Correlation between the production rate and primary particle diameter of the copper nanoparticles. Reproduced from Fu et al. [43], with permission from Nanotechnology (Copyright 2020).

cles directly obtained from the arc reactor and deposited on a TEM grid. These images illustrate that the copper nanoparticles, produced through the arc discharge process, are spherical in shape and exhibit agglomeration. The high-resolution transmission electron microscopy (HRTEM) images in Figure **4-3** (b) show a thin layer on the surface of each copper nanoparticle, with its thickness remaining similar regardless of the primary particle size. This surface layer on freshly synthesized copper nanoparticles (produced within three days) is approximately 2 nm thick. Previous studies have noted that an oxide layer ranging from 2-4 nm on copper nanoparticles is common in wet chemical processes [69, 70]. Therefore, the thin surface layer observed on Cu particles synthesized via gas-phase methods is similar to those produced through wet-chemistry techniques. The formation of this oxide layer on copper nanoparticles, which are generated by the direct evaporation of bulk copper materials, can likely be attributed to impurities in the carrier gas (N_2 with a purity of 99.9995 %) and the ambient conditions of the particle collection process.

Crystallographically, the synthesized copper nanoparticles were examined using X-ray diffraction (XRD), covering a 2θ range of 30°to 80°. As depicted in Figure **4-4** (a), the XRD pattern identifies three reflections at 2θ values of 43.4°, 50.5°, and 74.0°. These diffraction peaks correspond well with the (111), (200), and (220) planes of pure copper, which has a cubic face-centered unit cell and belongs to the Fm3m space group. The average crystallite size (d_{XRD}) of the synthesized copper nanoparticles was determined through the Rietveld refine-

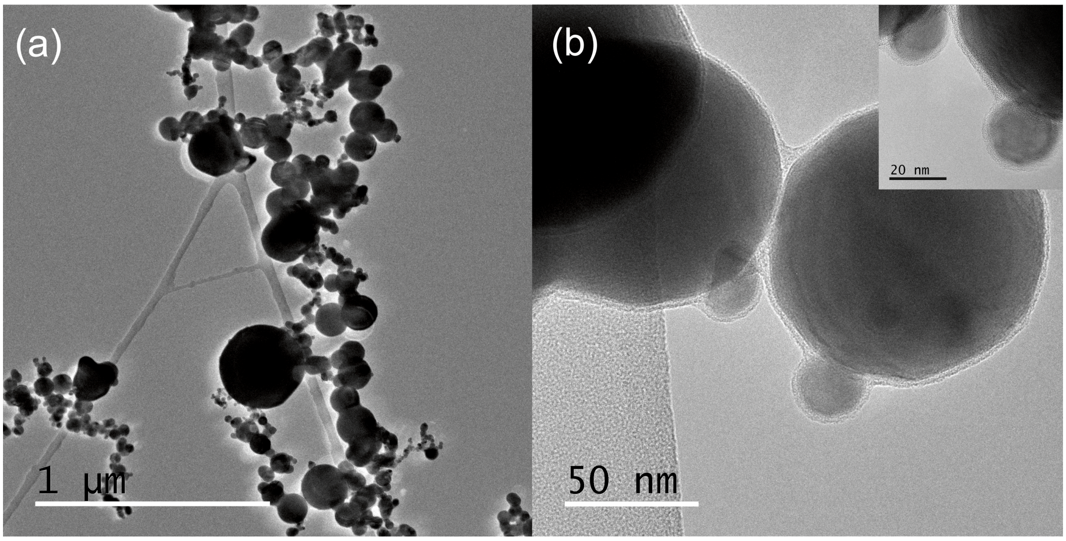

Figure **4-3**: (a) TEM image illustrating the morphology of copper nanoparticles and (b) HRTEM images of the copper nanoparticles synthesized after three days, highlighting a thin oxide layer on the particle surface. Reproduced from Fu et al. [43], with permission from Nanotechnology (Copyright 2020).

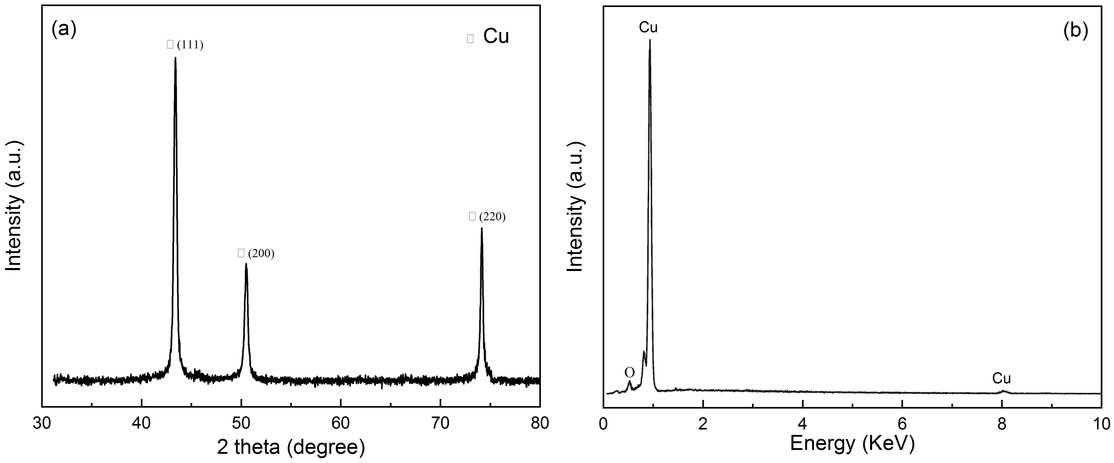

Figure **4-4**: (a) X-ray diffraction pattern and (b) EDX spectrum of copper nanoparticles synthesized after three days. Reproduced from Fu et al. [43], with permission from Nanotechnology (Copyright 2020).

ment method, indicating an average crystallite size of 50 nm. Energy-dispersive X-ray (EDX) spectroscopy, shown in Figure **4-4** (b), reveals oxygen (O) peaks in the synthesized copper particles, indicating an oxide layer on their surface. Notably, the XRD analysis did not detect significant peaks for Cu oxide, likely due to the minimal surface oxides in comparison to the predominant mass of bulk copper [73].

Arc discharge synthesis, as previously highlighted, offers the main advantage of being a continuous process that yields highly pure copper nanoparticles. In contrast to nanoparticles produced using classical chemical methods, those synthesized here lack a surfactant protective layer on their surface. It is well-known that copper nanoparticles are more prone to oxidation under ambient conditions than noble metals like gold and silver. To mitigate oxidation, it is recommended that the synthesized Cu nanoparticles be stored in an inert gas atmosphere with minimal exposure to oxygen.

4.2 Synthesis of titanium nitride nanoparticles (TiN NPs)

Titanium nitride (TiN), known for its superior mechanical and tribological properties, is widely used as a versatile protective material in the manufacturing of metal cutting tools and in aerospace engineering. This section focuses on producing TiN nanoparticles using direct current arc discharge under atmospheric pressure in an environment comprising nitrogen (N_2) and argon (Ar) gases. A thorough investigation was conducted to understand how synthesis parameters such as quench gas velocity, quench gas composition, and applied arc current influence the quality, yield, and size of the nanoparticles generated.

4.2.1 Experimental details

Particle production via arc discharge method

The experimental setup in this work is divided into three main components: nanoparticle production, and both online and offline particle characterization, as illustrated in Figure **4-5**. The arc discharge reactor, a key component of the setup, includes a reactor chamber, a power supply, and a gas supply system. In contrast to many studies that use commercial welding machines as the power source [86, 180, 120], this research utilizes a commercial plasma cutter (S-PLASMA 85 CNC, Expondo GmbH, Berlin, Germany) to create the arc plasma. A notable advantage of this plasma cutter is its ability to support higher carrier gas velocities compared to the welding machines previously used [86, 180]. Additionally, its computerized numerical control (CNC) port allows for real-time arc voltage measurement. The inclusion of a pilot port for pilot arc ignition also streamlines the ignition process, making it less dependent on the distance between the cathode and anode.

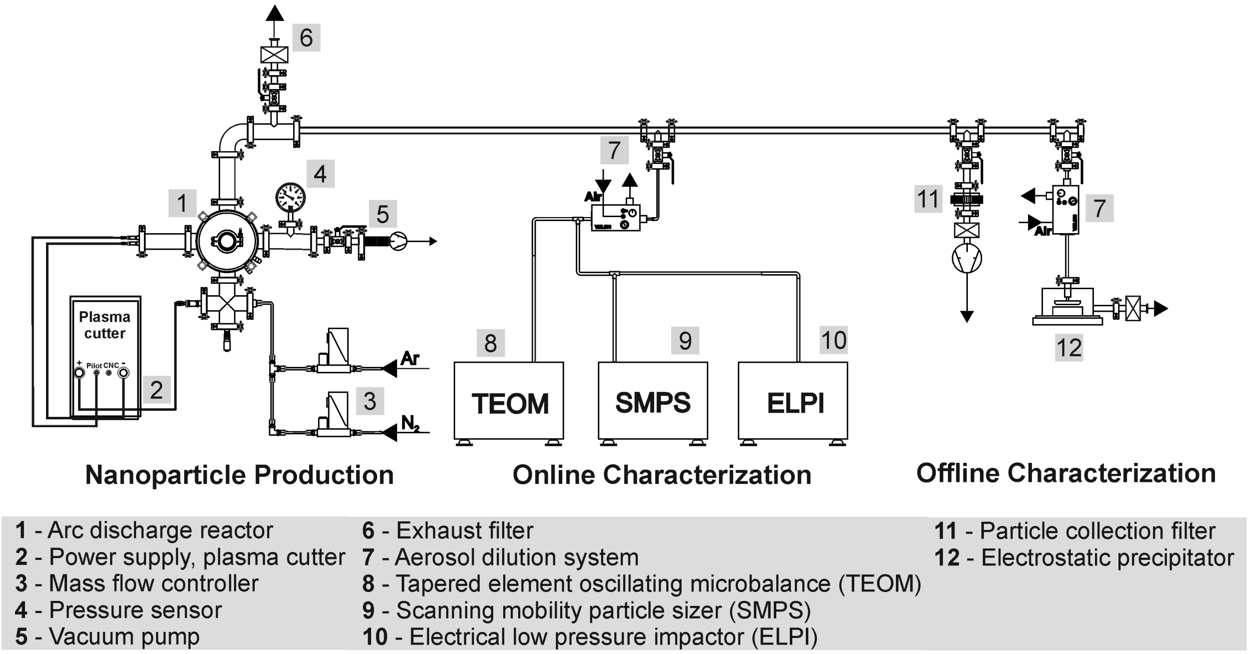

Figure **4-5**: Schematic diagram of the overall experimental setup. This setup is divided into three main parts: nanoparticle production, online characterization, and offline characterization. Reproduced from Fu et al. [41], with permission from Advanced Powder Technology (Copyright 2020).

In the gas supply system of this experiment, argon (Ar) and nitrogen (N_2) gases, each with a purity level of at least 99.99 %, are used as quenching gases. These gases are pre-mixed before their introduction into the reactor chamber. The flow rate of the gases is precisely controlled using thermal mass flow controllers (MFC, EL-Flow, Bronkhorst, Ruurlo, Netherlands), with the total gas flow maintained at 5 slm (standard liters per minute). To minimize oxygen contamination in the particle production process, the reactor chamber is initially evacuated to 50 Pa and then refilled three times with the quenching gas before the plasma arc is ignited. All production processes are conducted under atmospheric pressure, a condition necessitated by most online aerosol characterization devices, which are optimized for measuring aerosols at ambient pressures.

Figure **4-6** features schematic drawings of two reactor chamber configurations used for evaporating a titanium rod (anode) and forming TiN_x nanoparticles. The chamber is a double-walled DN ISO-K 160 structure, equipped for water-cooling, and includes five circumferentially arranged ISO-KF 40 flanges. These KF 40 ports serve various functions: gas inlet, aerosol outlet, electrode arrangements, visual observation, and gas evacuation. Two tungsten electrodes (WL-15 gold: 98.5 % tungsten and 1.5 % lanthanum oxide; 1.6 mm diameter) are installed on the left flange, positioned above the titanium rod anode (6.35 mm diameter,

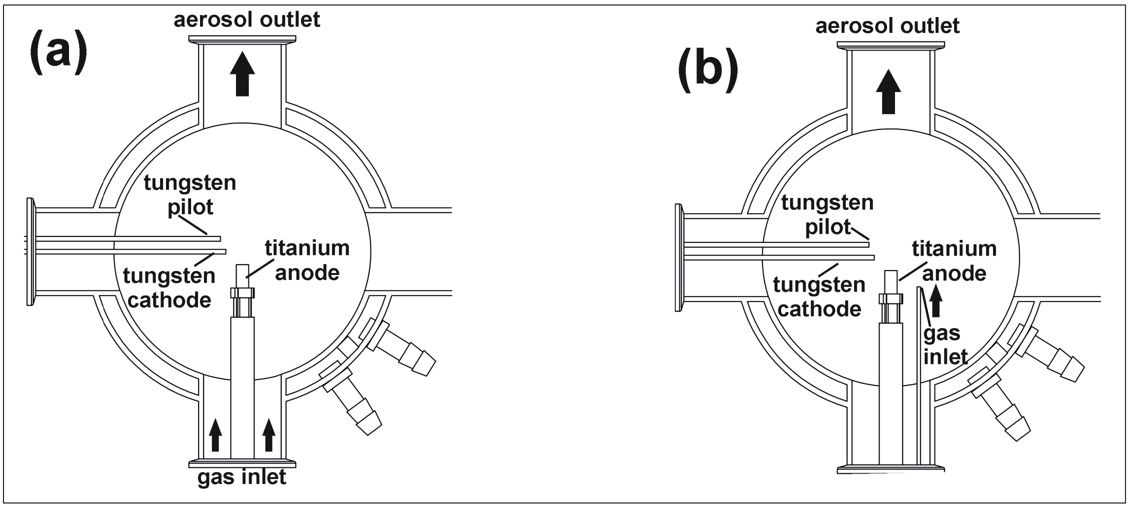

Figure **4-6**: Schematic configurations of the reactor chamber. Chamber (a) depicts the configuration for particle production at a low gas inlet velocity of approximately 0.1 m/s, while chamber (b) shows the configuration used for a high gas inlet velocity of around 40 m/s. Reproduced from Fu et al. [41], with permission from Advanced Powder Technology (Copyright 2020).

Table **4-1**: Overview of experimental parameters for nanoparticle synthesis using the reactor configuration with a high gas inlet velocity. Reproduced from Fu et al. [41], with permission from Advanced Powder Technology (Copyright 2020).

Sample No.	**N_2 [slm]**	**Ar [slm]**	**Total gas flow [slm]**	**Electrode distance [mm]**	**Current [A]**
# 1	**5**	**0**	5	5	20
# 2	**4**	**1**	5	5	20
# 3	**3**	**2**	5	5	20
# 4	**2**	**3**	5	5	20
# 5	**1**	**4**	5	5	20
# 6	**0**	**5**	5	5	20
# 7	4	1	5	5	**12**
# 8	4	1	5	5	**28**
# 9	4	1	5	5	**36**
# 10	4	1	5	5	**44**
# 11	4	1	5	5	**50**

>99.99 % purity, ChemPur GmbH, Karlsruhe, Germany). This 90° electrode arrangement has been previously validated for optimal arc stability [86]. As depicted in Figure **4-6** (a), the upper tungsten electrode connects to the pilot arc port, and the lower one to the cathode port of the plasma cutter. Initially, a pilot arc (limited current <5 A) is ignited between the pilot electrode and cathode. This arc is then transferred to the titanium anode via gas flow, creating a plasma arc (high current >10 A) between the tungsten cathode and titanium anode. The intense thermal energy of the arc plasma continuously evaporates the anode material, leading to nanoparticle formation, which is further discussed in the subsequent section. The distance between the cathode and anode was consistently maintained at 5 mm using a micrometer drive throughout the production processes.

To explore the impact of inlet gas velocity, the gas inlet position was modified, and the gas pipe diameter was reduced (inner diameter: 1.6 mm), as illustrated in Figure **4-6** (b). Additionally, production parameters like gas composition and applied current were systematically varied to examine their effects on particle synthesis. For consistency, each synthesis experiment was repeated at least three times, and the titanium rod (anode) was either renewed or polished whenever production parameters were altered. Table **4-1** summarizes the experimental conditions for the synthesis using reactor configuration illustrated in Figure **4-6** (b).

Online and offline characterization of titanium nitride NPs

The characterization measurements used in this thesis are categorized into two parts: online characterization, which involves direct measurement during synthesis in the gas phase, and offline characterization, which is not continuous and is performed only after collection from a filter. For online characterization of the produced nanoparticles, standard particle measurement devices such as the Scanning Mobility Particle Sizer (SMPS), Tapered Element Oscillating Microbalance (TEOM), and Electrical Low-Pressure Impactor (ELPI) were employed. However, these devices are unsuitable for high particle number concentrations. To address this, an aerosol dilution system with a dilution ratio of 100 (VKL10+VKL10 cascade system, Palas GmbH, Karlsruhe, Germany) was used to reduce the particle number concentration. The particle mass concentration in the produced aerosol (mg/cm^3) was measured using the TEOM (Model 1405, Thermo Fisher Scientific, Waltham, USA). The production rate (mg/h) was then calculated based on the known total aerosol flow (cm^3/h) and the dilution ratio. Additionally, an SMPS was utilized to determine the particle size distribution based on the equivalent mobility diameter. This device comprises a neutralizer, a Differential Mobility Analyzer (DMA 3081, TSI, Minneapolis, USA), and a Condensation Particle Counter (CPC 3775, TSI). The ELPI (ELPI+, Dekati Ltd., Tampere, Finland) was used to gather information on the aerosol size distribution based on the aerodynamic or Stokes diameter.

For offline characterization, methods such as X-ray diffraction (XRD), gravimetric measurement, and scanning electron microscope (SEM) analysis were employed to ascertain various particle characteristics. In SEM analysis (JSM 7500F, Jeol GmbH, Tokyo, Japan), the samples were prepared by depositing particles on carbon-coated TEM grids via electrostatic precipitation [32]. For other offline measurements, the produced aerosol was directed through a filter (PE filter with a PTFE membrane, R&B Filter GmbH, Langenbrettach, Germany) to deposit the particles. The particle production rate (mg/h), as determined by gravimetric measurement, is based on the particles collected from this filter. This measurement was performed using an analytical balance (XS205, Mettler-Toledo AG, Switzerland). Additionally, the collected nanoparticles were utilized for SEM measurement to examine particle microstructures, Brunauer-Emmett-Teller (BET) analysis to estimate the primary particle size, and X-ray diffraction (XRD) to analyze crystal phase composition. The specific surface area of the produced particles was measured using a BET analyzer (Gemini VII 2390a, Micromeritics Instruments Corporation, GA, USA). The 2D-XRD measurements were conducted at beamline BL9 of the synchrotron light source DELTA [105] (TU Dortmund University, Germany), using an image plate detector MAR345 (marXperts, Germany) for photon detection. The experiments were set at a photon energy of 27 keV ($\lambda = 0.45920\,\mathring{A}$), and the nanoparticles were analyzed in transmission mode within a 1.0 mm diameter glass capillary. The sample-to-detector distance, beam center, and detector non-orthogonality were calibrated using fit2d [27], with Si powder as a reference. For comparative purposes, the 2-Theta angle of the patterns was converted to Cu-Kα1. The crystallite size was calculated using the Scherrer equation, employing a Lorentz fit and a Scherrer constant of 0.64.

4.2.2 Effect of quench gas velocity

The quality and quantity of synthesized nanoparticles are known to depend on various process parameters, such as quench gas flow, gas composition, and supply power. This section investigates the effect of quench gas flow on nanoparticle synthesis, with all other parameters held constant (refer to experimental condition No. 2 in Table **4-1**). The quench gas velocity was adjusted by altering the gas inlet position and the diameter of the inlet gas pipe, as illustrated in Figure **4-6**. Figures **4-7** (a) and **4-7** (b) display representative SEM (upper) and STEM (lower) micrographs of the nanoparticles synthesized under high and low gas velocities, respectively. It is observed that the morphology of the nanoparticles is similar in both instances, predominantly cubic, with some exhibiting triangular and polyhedral shapes.

As shown in Figure **4-7**, the majority of primary particles are found to measure between 10 and 15 nm under high gas velocity. In contrast, at lower velocities, their sizes range from 20 nm to 50 nm. Despite variations in the size of agglomerates, primary particles exceeding 30 nm at high velocities or 60 nm at low velocities were not observed in SEM or STEM images.

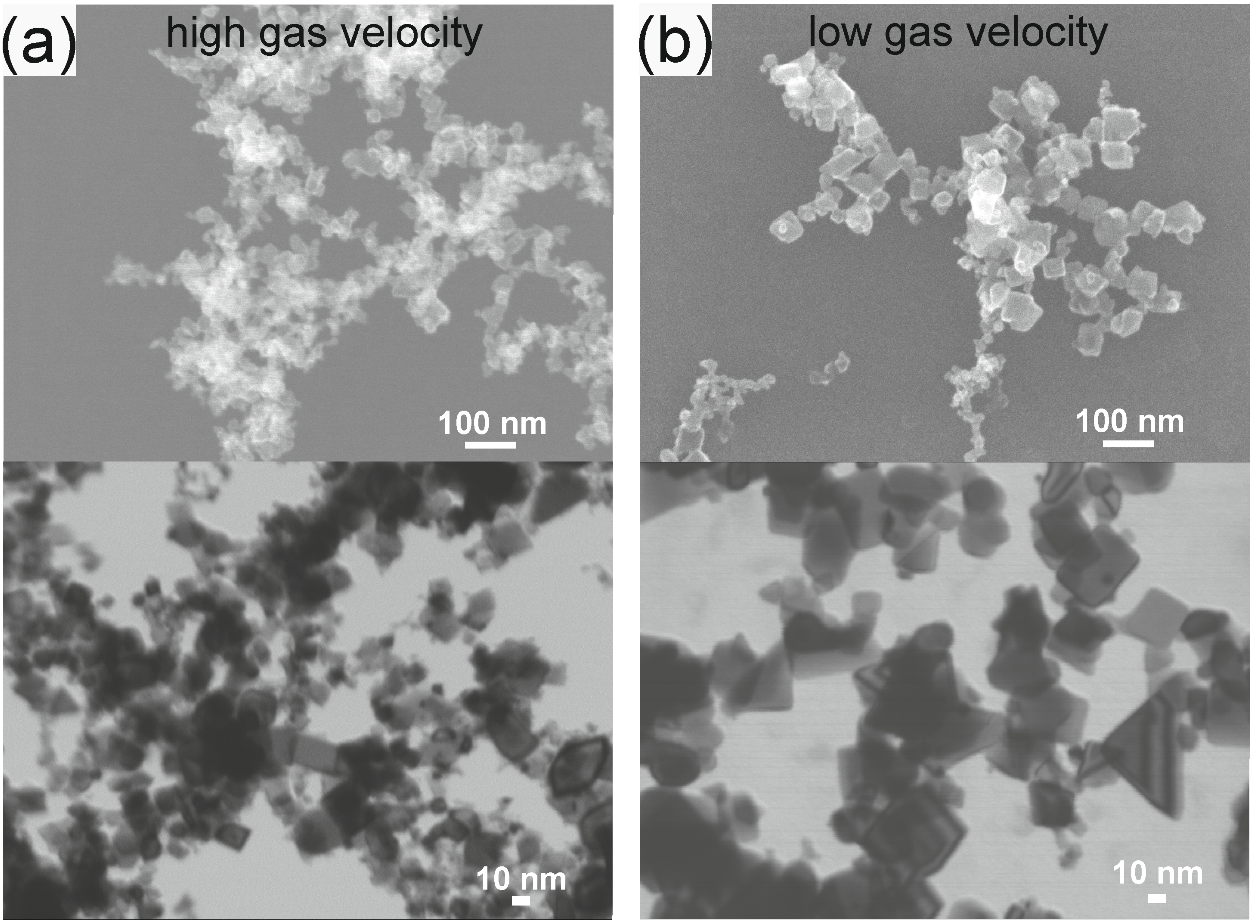

Figure **4-7**: Effect of quench gas velocity on particle size and morphology of the particles produced in arc discharge reactor. SEM and STEM images (a) illustrate results at high gas velocity, while images (b) correspond to low gas velocity, with all other processing parameters constant (20 A, flow rates of 4 slm N_2 and 1 slm Ar, and an electrode distance of 5 mm). Reproduced from Fu et al. [41], with permission from Advanced Powder Technology (Copyright 2020).

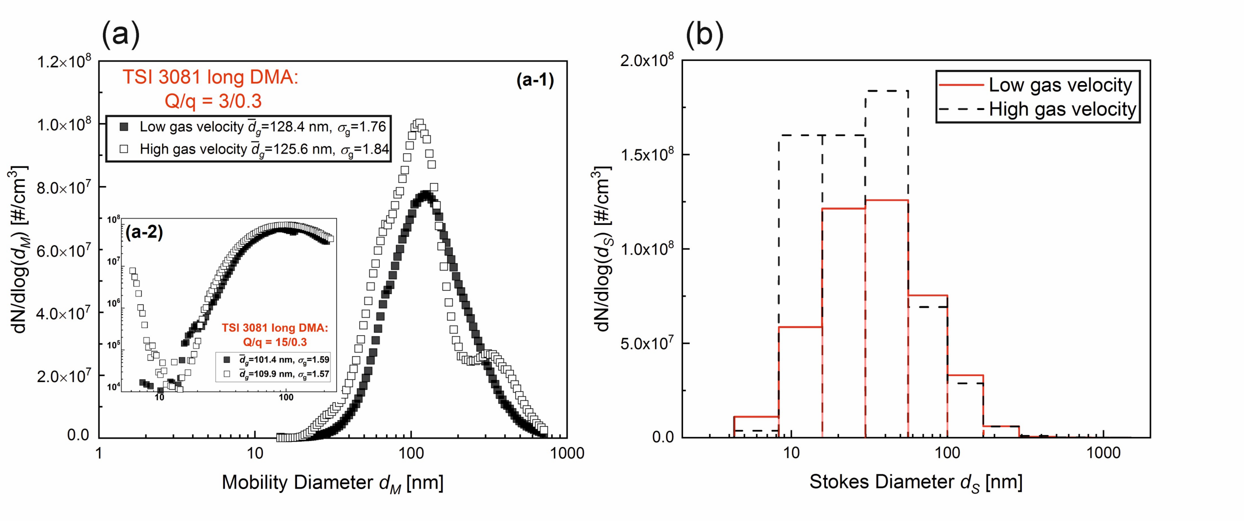

Figure **4-8**: Effect of quench gas velocity on particle size distribution (The dilution factor has been considered) as determined by (a) a scanning mobility particle sizer (SMPS) and (b) an electrical low-pressure impactor (ELPI), with other processing parameters held constant (20 A, 4 slm N_2+1 slm Ar, electrode distance of 5 mm). Reproduced from Fu et al. [41], with permission from Advanced Powder Technology (Copyright 2020).

Consistent with the findings of Chen et al. [21], the quench gas velocity is demonstrated to directly impact the residence time of particles in the formation zone. An increase in gas velocity decreases particle residence time, thereby limiting the processes of coagulation and growth.

Figure **4-8** illustrates the effect of quench gas velocity on particle size distribution. The particle number concentrations as function of electrical mobility diameter and Stokes diameter were determined by SMPS, as shown in Figure **4-8** (a), and by ELPI, as shown in Figure **4-8** (b). The SMPS measurements were conducted at an aerosol flow rate of 0.3 slm (standard liters per minute). This work utilized two sheath-to-aerosol flow rate ratios (Q/q) in the DMA (TSI 3081), specifically 15/0.3 and 3/0.3, enabling the classification of nanoparticles ranging from 6 to 200 nm and 15 to 700 nm, respectively. Figure **4-8** (a-1) reveals that nanoparticles generated under low and high quench gas velocities exhibited geometric mean diameters ($\bar{d}_g$) of 128.4 nm and 125.6 nm, respectively, which significantly exceed the primary particle sizes identified through SEM analysis. This discrepancy suggests that the particles exiting the arc reactor undergo agglomeration, and the size distributions captured by SMPS more accurately reflect agglomerate rather than primary particle sizes. The aerosol particles in both scenarios showed broad size distributions, with geometric standard deviations (σ_g) of 1.76 and 1.84. Additionally, while not shown here, it is noteworthy that the total particle number concentration, when measured at a sheath to aerosol flow rate ratio (Q/q) of 3/0.3, increased by approximately 20 % under high quench gas velocity conditions. In Figure **4-8** (a-2), where a sheath-to-aerosol flow rate ratio (Q/q) of 15/0.3 was applied, a significantly higher number concentration of particles below 10 nm was observed during aerosol synthesis at high gas velocities compared to lower velocities. This increase in the number concentration of sub-10 nm aerosol particles suggests that the shorter residence time, induced by higher quench gas velocities, promotes the formation of smaller particles, aligning with observations from SEM analysis.

To fabricate novel nanocomposite coatings, nanoparticles within specific size ranges need to be injected into a growing physical vapor deposition (PVD) thin film. This process, detailed in a related study [190], requires an aerodynamic lens system to transfer nanoparticles from the arc discharge particle generation process into the PVD coating process. Consequently, an examination of the particle size distribution, specifically based on the Stokes diameter, was conducted to understand the aerodynamic behavior of the synthesized aerosols. As depicted in Figure **4-8** (b), particles exiting the reactor exhibit a wide range of Stokes diameters, spanning from 5 to 1000 nm in both experimental setups, with only a minor portion exceeding 300 nm in diameter. Within the size range of 8 to 50 nm, the concentration of particles is significantly higher at high gas velocities than at low gas velocities. This finding suggests that a higher quench gas velocity is effective in producing nanoparticles with smaller Stokes diameters, indicating a favorable adjustment in the synthesis process for enhanced aerodynamic properties.

It should be highlighted that, in Figure **4-6** (b), the gas flow emerges from one side, resulting in an asymmetrical gas flow. This asymmetry can cause a non-uniform temperature distribution, leading to a wide range of particle sizes. To promote a more consistent increase in quenching gas velocity and decrease the residence time of particles, Figure **4-9** introduces a modified reactor design. This design incorporates an anode material surrounded by four inlet nozzles, as detailed in Appendix A, aimed at enhancing the airflow rate and ensuring even cooling, which is crucial for the production of nanoparticles. For the purposes of this work, the setup depicted in Figure **4-6** (b) was employed for further exploration, particularly because it facilitates the generation of smaller titanium nitride nanoparticles (approximately 10 nm in size), which are preferred for creating TiN/CrN nanocomposite thin films.

4.2.3 Effect of quench gas composition

Different quench gas compositions were employed to evaluate their impact on crystal structure and yield of particles. Figure **4-10** displays the influence of quench gas composition on both the particle production rate (part a) and arc voltage (part b), under fixed process conditions (20 A, 4 slm N_2+1 slm Ar, 5 mm electrode distance). The measurement of the particle production rate was conducted both online, using TEOM, and offline, through gravimetric methods. It is important to note that the reported production rate (mg/h) reflects the quan-

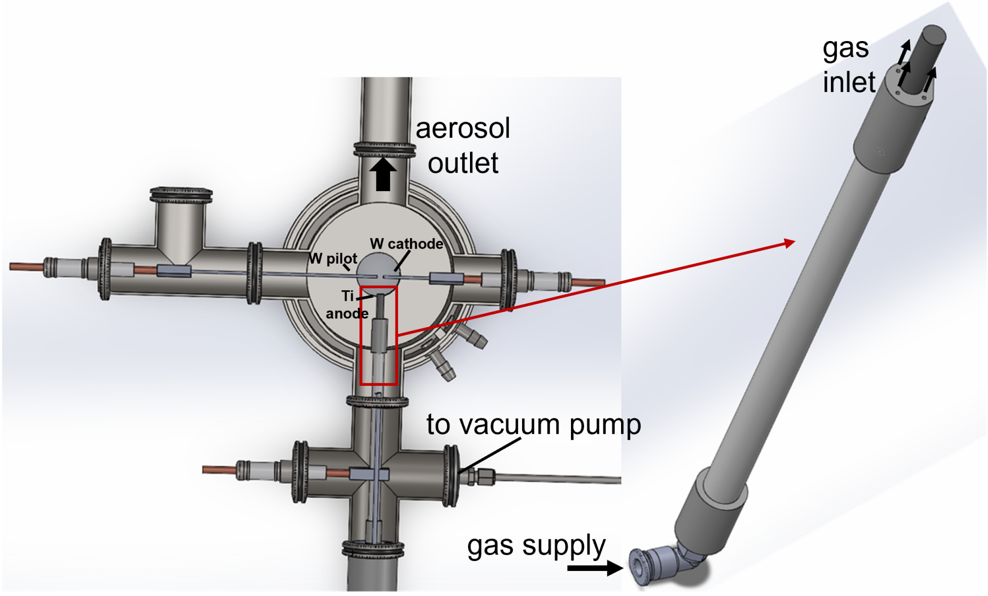

Figure **4-9**: Proposed reactor configuration for uniformly enhancing quenching gas velocity.

tity of particles collected from the filter, not the anode material's evaporation rate. Due to significant particle loss to the reactor walls and housing, the actual particle production rate is markedly lower than the material evaporation rate. As evidenced in Figure **4-10** (a), an increase in N_2 concentration correlates with a higher particle production rate. Specifically, increasing N_2 from 20 % to 100 % triples the TiN_x particle production rate. The increase in particle mass yield can be attributed to the increasing arc voltage. This effect occurs as the nitrogen concentration rises, as demonstrated in Figure **4-10** (b). In this work, the arc voltage between the two electrodes was measured through the CNC port of the plasma cutter. The arc voltage was observed to increase almost linearly with nitrogen content, with the voltage for 100 % Argon being 9 V less than that for 100 % N_2. Ramirez-Argaez's mathematical model indicates that an argon atmosphere produces a low-temperature arc region, attributed to lower Joule heat (due to lower voltage and electric resistance) [162]. Therefore, adding nitrogen to the quench gas enhances arc voltage and, thereby, the power input, while other process variables remain constant. This increased power input leads to more material evaporation, which then enhances the particle production rate. Additionally, the formation of tiny bubbles in the anode feedstock in bi-atomic gases like nitrogen has been suggested as another factor influencing particle production rates [179].

Figure **4-11** (a) and Figure **4-11** (b) illustrate the impact of quench gas composition on the crystal structure of nanoparticles. The X-ray diffraction (XRD) pattern of nanoparticles synthesized using pure nitrogen aligns with the cubic TiN reference pattern (JCPDS 38-1420), indicating that the phase TiN has been formed. Conversely, nanoparticles produced using a mixture of argon and nitrogen also correspond to the TiN reference pattern, but their

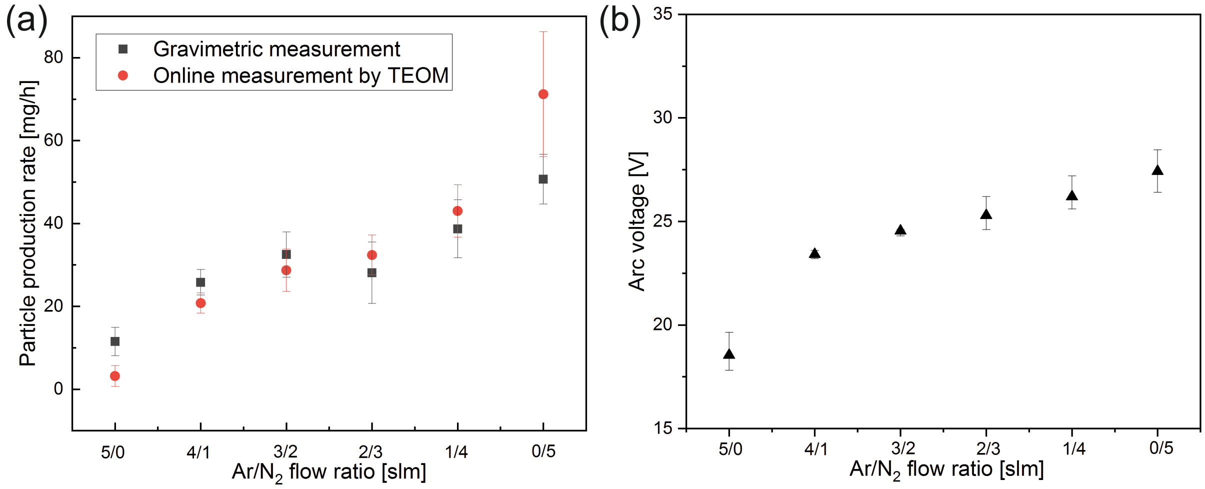

Figure **4-10**: Effect of quench gas composition on particle production rate (a) and arc voltage (b), with constant process parameters (20 A, 4 slm N_2+1 slm Ar, 5 mm electrode distance). Reproduced from Fu et al. [41], with permission from Advanced Powder Technology (Copyright 2020).

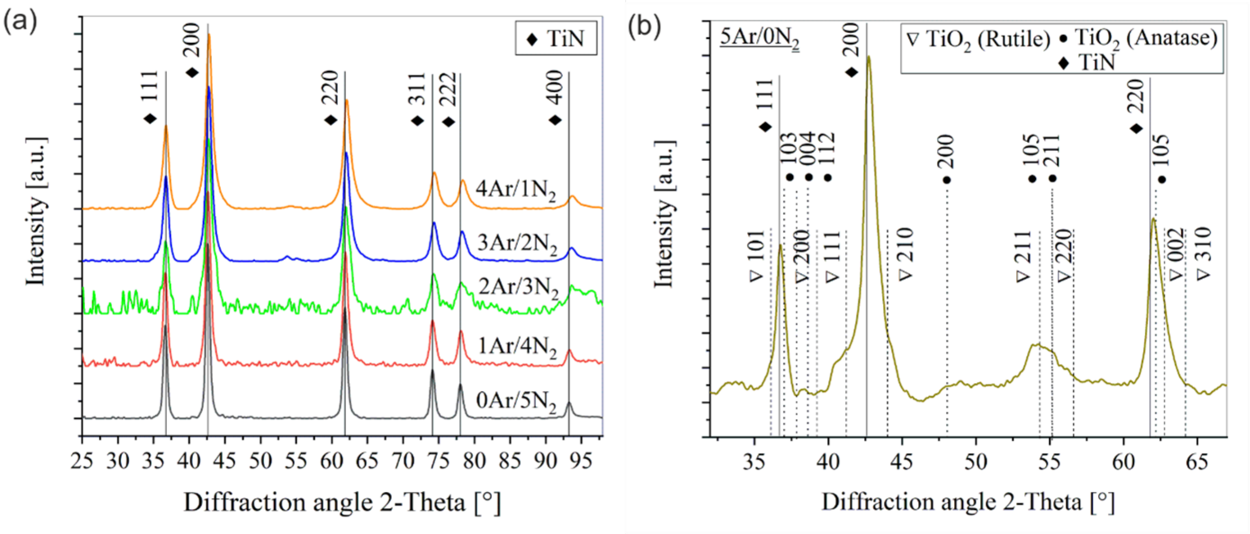

Figure **4-11**: Diffraction patterns of TiN_x nanoparticles synthesized using a quenching gas (a) containing nitrogen and (b) without nitrogen. Reproduced from Fu et al. [41], with permission from Advanced Powder Technology (Copyright 2020).

reflections shift marginally towards higher two-Theta angles as the Ar/N_2 ratio increases. This shift can be attributed to the reduced nitrogen content in nanoparticles formed with a higher proportion of argon in the quench gas.

Figure **4-11** (b) showcases the diffraction pattern of nanoparticles synthesized without nitrogen in the quench gas. Predominantly, these patterns align with the cubic TiN reference. This alignment is partly due to residual TiN_x on the titanium (Ti) anode from earlier TiN_x syntheses. Absent this residual TiN_x, the Ti anode would rapidly melt, forming a droplet and interrupting the arc discharge. Therefore, to maintain stable arc operation when using only argon as the quench gas, the residual TiN wasn't completely removed from the titanium rod. Conversely, for synthesizing pure TiN nanoparticles, any residue on the titanium rod was thoroughly polished away to prevent it from influencing the characteristics of nanoparticles.

In addition to the TiN reflections, Figure **4-11** (b) reveals extra reflections, identifiable as TiO_2. The reference patterns for both the rutile (JCPDS 21-1276) and anatase (JCPDS 21-1272) phases are presented for comparison. It appears these oxides coexist, although precise analysis is challenging due to the broad nature of the reflections. The simultaneous presence of TiN and TiO_2 might stem from the high affinity of titanium for both nitrogen and oxygen, as indicated in various studies [187]. Additionally, the formation of TiO_2 phases may occur during the particle handling process. This can be further investigated by minimizing prolonged exposure to ambient air. Unlike other studies where TiO_2 phases in TiN nanoparticles were identified using XRD and XPS [122], such phases were not detected in the TiN nanoparticles produced in this work. The TiN nanoparticles created here differ from those synthesized via vapor phase reaction between $TiCl_4$ and NH_3, which contained additional byproducts like NH_4Cl [52]. Furthermore, TiN nanoparticles made using atmospheric pressure microplasma also exhibited oxide phases attributable to rutile and anatase [122]. According to these researchers, adding nitrogen to the process gases can reduce the oxide quantity, yet even with a 9 % hydrogen presence, oxide formation is not completely inhibited.

Figure **4-12** displays the trend in crystallite size of TiN_x nanoparticles, showing an increase in size as the nitrogen content in the quench gas rises. The size ranges from 4.0 ± 0.7 nm with a 5Ar/0N_2 ratio to 23.6 ± 3.1 nm for a 0Ar/5N_2 ratio. Comparatively, TiN nanoparticles produced through an atmospheric pressure microplasma process exhibit sizes around 10 nm [122], which aligns with the sizes of TiN nanoparticles synthesized in this work with Ar/N_2 ratios ranging from 4/1 to 2/3. Moreover, notable alteration in the lattice parameter occurs when changing the quench gas composition from 5Ar/0N_2 slm to 4Ar/1N_2 slm, where the lattice parameter rises from $4.170 \pm 0.034\,\mathring{A}$ to $4.226 \pm 0.006\,\mathring{A}$. With pure nitrogen as the quench gas, the lattice parameter attains a value of $4.240 \pm 0.003\,\mathring{A}$, closely matching the TiN reference value of $4.242\,\mathring{A}$ (JCPDS 38-1420), as depicted in Figure **4-12**.

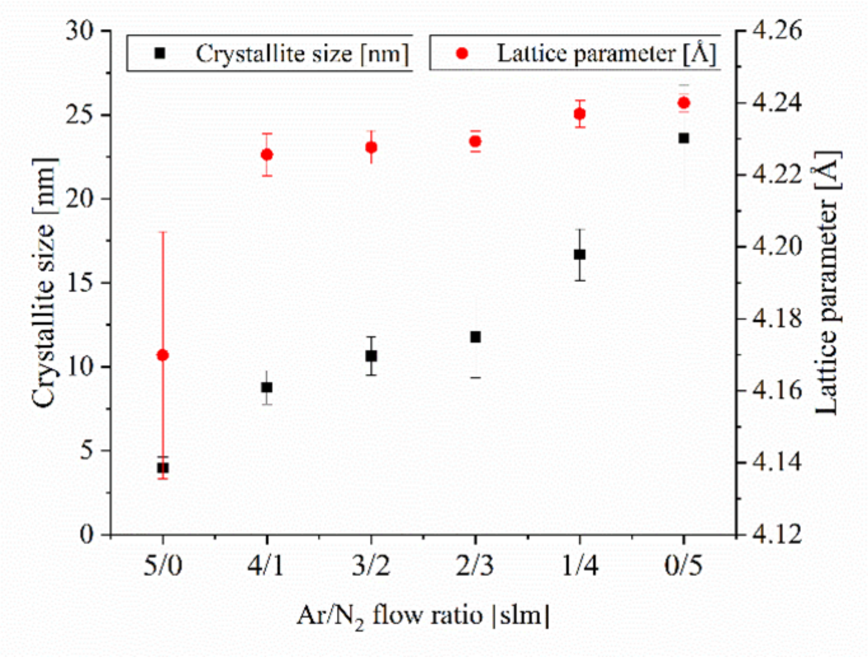

Figure **4-12**: Effect of quench gas composition on the crystallite size (left axis) and lattice parameter (right axis) of TiN$_x$ nanoparticles. Reproduced from Fu et al. [41], with permission from Advanced Powder Technology (Copyright 2020).

4.2.4 Effect of applied arc current

Figure **4-13** (a) displays how the particle production rate (mg/h) varies with applied arc current, maintaining constant electrode distance (5 mm) and quench gas composition (1 slm Ar and 4 slm N_2). The rates were measured using both TEOM and gravimetric methods. An increase in arc current has been linked to a rise in the production rate of titanium nitride nanoparticles. As discussed earlier, with all other variables constant, a higher arc current emits more electrons from the cathode, striking the anode at high velocity. This interaction leads to resistive heating on the anode surface, elevating its temperature. Consequently, a higher arc current causes an increase in the anode surface temperature, leading to more material evaporation and particle production. Notably, the particle production rate approximately increased tenfold when the arc current was raised from 12 to 50 A.

Although numerous studies have indicated that higher arc currents may lead to an increase in the primary particle size, this effect can significantly vary across different materials [129, 178, 130]. For instance, Stein et al. [178] observed that the primary size of copper nanoparticles rose by nearly 30 nm when the arc current increased from 15 A to 45 A. However, as illustrated in Figure **4-13** (b), the primary particle size measured by BET shows only a slight change (no more than 3 nm) when the arc current is raised from 12 A to 50 A. Conversely, the geometric mean size of agglomerates, determined by SMPS, exhibits an almost linear growth with

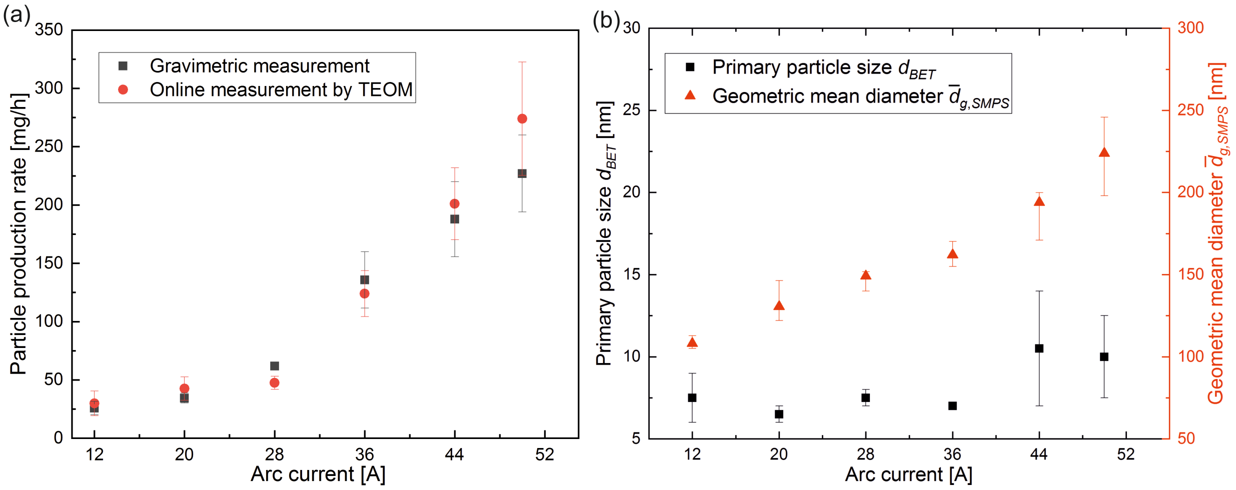

Figure **4-13**: Variations in particle production rate with applied arc current (a), and comparative analysis of primary particle size (d_{BET}) and geometric mean diameter ($\bar{d}_{g,SMPS}$) at different arc current settings (b). Reproduced from Fu et al. [41], with permission from Advanced Powder Technology (Copyright 2020).

increasing arc current, ranging from 108 nm at 12 A to 224 nm at 50 A.

It's also worth noting, though not shown here, that the total particle number concentration for productions over 28 A rises significantly, aligning well with the observed enhancements in production rates. In summary, the increase in the production rate of titanium nitride nanoparticles primarily manifests as a rise in both the agglomerate size and the total particle number concentration. Increasing the applied current from 12 A to 50 A has a minimal effect on the primary particle size of titanium nitride nanoparticles. This suggests that the coagulation and sintering rate of titanium nitride at the temperatures present in the agglomeration zone is relatively low, thereby preventing substantial crystal growth within the agglomerates.

4.2.5 Mechanism of deposit growth on the cathode tip

Figure **4-14** presents images of the electrode within the arc reactor chamber after an hour of operation in both Ar plasma and Ar-N_2 plasma. Notably, the titanium anode undergoes a color shift from grayish to golden due to nitriding, contrasting with the absence of color change observed during Ti particle synthesis. For the production of titanium nitride nanoparticles, a mixture of N_2 and Ar was introduced into the high-temperature arc region. This, however, necessitated manual intervention approximately every 20 minutes to maintain arc continuity over several hours. This instability arises from the gradual accumulation of deposits on the cathode tip during synthesis. Although these deposits do not extinguish the arc, due to the high electrical conductivity of titanium nitride, they do lead to a reduction

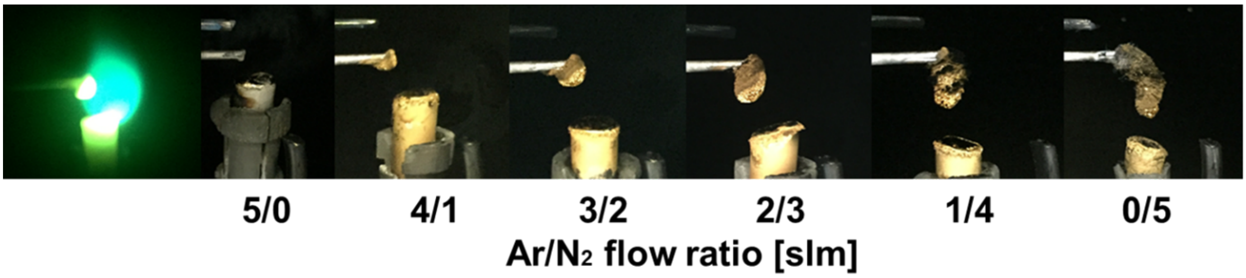

Figure **4-14**: Optical images show changes of electrodes after one-hour production at 20 A and 5 mm distance between anode and cathode.

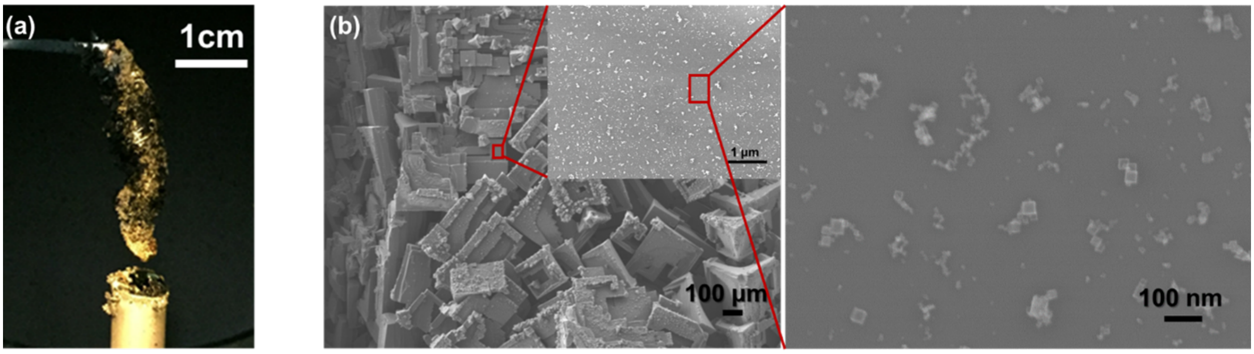

Figure **4-15**: (a) A representative photograph displays the cathode deposits after three hours of synthesis (low gas velocity, 5 slm N_2, 20 A). (b) The corresponding SEM images demonstrate that the cathode deposits form through the nucleation and growth process.

in the electrode gap. This reduction could potentially result in a short circuit between the cathode and anode. Furthermore, in the TiN NP synthesis, the rate of deposit formation accelerated with an increased nitrogen ratio in the quench gas. As evidenced in Figure **4-10** (a), a higher nitrogen content correlates with an increased nanoparticle production rate. Consequently, it's evident that the rate of cathode deposit growth is directly proportional to the particle production rate.

Furthermore, increasing the quench gas velocity cannot reduce or remove the deposit. This suggests that the deposit does not consist of nanoparticle agglomerates held together by Van der Waals forces. The deposit on the cathode tip was examined using a scanning electron microscope (SEM), as depicted in Figure **4-15** (b). Analysis confirms that the cathode deposits formed during the TiN nanoparticle synthesis are titanium nitride crystals, with sizes ranging from 0.3 to 1 mm. Cubic nanoparticles, predominantly with primary particle sizes less than 20 nm, are observed on the surface of these titanium nitride crystals. However, the adherence of these particles appears to be an inherent part of the gas phase process. These findings collectively indicate that the formation of the cathode deposits occurs during

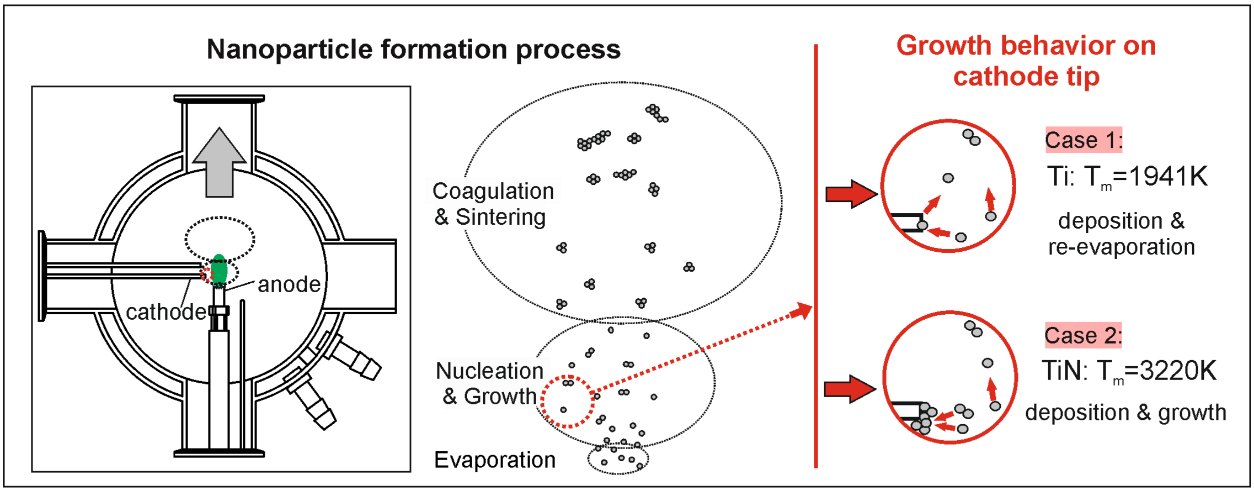

Figure **4-16**: Schematics illustrating the nanoparticle formation and deposit growth behavior on the cathode tip. Adapted from Fu et al. [41], with permission from Advanced Powder Technology (Copyright 2020).

the nucleation and growth stages of the synthesis process.

Regular operator intervention is necessary to ensure continuous operation of the arc for several hours and maintain a constant electrode distance. However, frequent manual intervention is not feasible for industrial-scale applications. Therefore, a thorough understanding of both particle and cathode deposit formation in arc discharge synthesis is essential. This knowledge could aid in optimizing the synthesis process, especially for maintaining stable arc operation. Figure **4-16** offers a potential explanation for the growth behavior of cathode deposits.

The synthesis of metal (case 1 in Figure **4-16**) and metal nitrides (case 2 in Figure **4-16**) nanoparticles via the arc discharge method involves gas-phase synthesis processes: generation of supersaturated vapor, nucleation, condensation, coagulation, and sintering [104]. Metal vapors, produced due to high temperatures, are quickly transported to the quench region by the quench gas flow. For the production of metal nitride nanoparticles, nitrogen is incorporated into the gas flow. The rapid cooling of titanium or titanium nitride vapor in the quench region by the room-temperature carrier gas leads to the formation of a supersaturated vapor. This supersaturated state promptly initiates cluster nucleation and condensation, followed by particle growth. Typically, particles from gas-phase reactors are non-spherical. Primary particles, formed through nucleation and growth, coagulate and form agglomerated particles upon collision, as depicted in Figure **4-16**.

The formation of deposits on the tungsten cathode tip is likely due to the temperature at the cathode tip. Cunha et al. [28] used numerical and experimental methods to estimate that the maximum temperature of lanthanated tungsten at 200 A DC is 3100 K, which lies between the melting points of titanium metal (1941 K) and titanium nitride (3220 K). During the formation of TiN_x nanoparticles, the cathode tip temperature might not be high enough to re-evaporate the deposits, accumulating titanium nitride crystals. Several recent studies support this explanation. For instance, the tungsten cathode temperature reached as high as 3200 K with an arc current of 40 A in an atmosphere of 400 torr of N_2 [208]. This temperature was experimentally monitored using an IR (infrared) camera and calibrated with a thermocouple attached to the cathode. Furthermore, Stein et al. [179] reported that no deposits were observed on the tungsten cathode tip during the synthesis of Cu, Zn, Ag nanoparticles (which have melting points below 1500 K) via arc discharge.

During arc plasma synthesis, the cathode functions as a thermionic emitter. This means that at high temperatures, the thermal energy provided to the electrons is sufficient to overcome the work function of the cathode material, leading to electron emission from the cathode electrode surface. Specifically, the cathode tip is heated by the heat flux of the arc plasma, which induces electron emission from the hot tungsten cathode. The temperature of the cathode, corresponding to this process, can be estimated using the Richardson-Dushman equation. This equation relates the current density J (A/mm^2) of thermionic emission to the temperature of the emitting material, as referenced in [127]:

$$J = A_0 T^2 exp(-\frac{W_\mathrm{A}}{k_B T}) \tag{4-1}$$

where A_0 is Richardson constant (120 $A \cdot \mathrm{mm}^{-2} \cdot K^{-2}$), T is the temperature in K of cathode surface, W_A is the work function of cathode material (4.55 eV for pure tungsten), $\mathrm{k_B}$ is the Boltzmann constant (8.62×10^{-5} $\mathrm{eV} \cdot \mathrm{K}^{-1}$), and J is the electron current density (A/mm^2). The electron current density J can be expressed as the arc plasma current I (A) divided by the emitting area of the cathode tip, which is $\pi d_\mathrm{cat}^2/4$ (with d_cat being the cathode tip diameter). Therefore, the Richardson-Dushman equation can be reformulated as follows in the equation:

$$I = \frac{\pi d_\mathrm{cat}^2 A_0 T^2}{4} exp(-\frac{W_\mathrm{A}}{k_B T}) \tag{4-2}$$

Using the above equation, the relationship between the cathode tip temperature and factors such as arc current and cathode tip diameter can be illustrated, considering work functions (W_A) of 2.8 eV, 3.4 eV, 3.5 eV, and 4.5 eV, as depicted in Figure **4-17**. This work employs lanthanated tungsten, notable for its lower work function (2.7 eV) compared to pure tungsten (4.5 eV). Table **4-2** summarizes the work functions for various types of tungsten, including pure, thoriated (ThO_2-doped), and lanthanated (La_2O_3-doped). A lower work function in an electrode reduces the necessary voltage to initiate an arc, thereby facilitating arc ignition. In

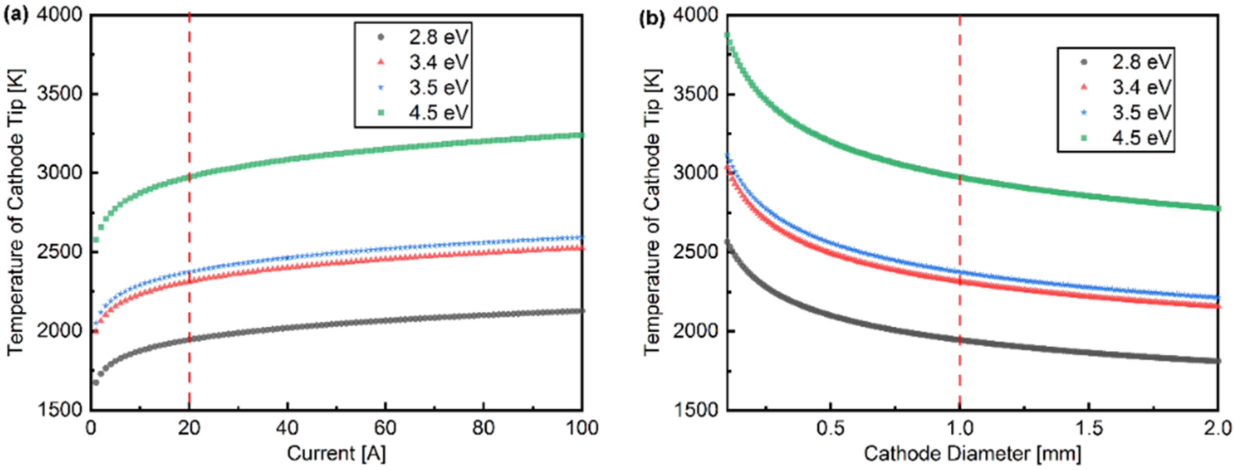

Figure **4-17**: Calculated temperature of cathode tip for $W_\mathrm{A} = 2.8\,\mathrm{eV}$, $3.4\,\mathrm{eV}$, $3.5\,\mathrm{eV}$, $4.5\,\mathrm{eV}$ as a function of current I (with constant cathode diameter 1.0 mm) (a) and as a function of cathode diameter (with constant current 10 A) (b).

Table **4-2**: Summary of the work function of pure tungsten, thoriated (doped with ThO_2) tungsten, and lanthanated (doped with La_2O_3) tungsten, as reported by Hoebing et al. [63].

Element	**Work function** $W_\mathbf{A}$ **/eV**	**Work function on Tungsten** $W_\mathbf{A}$ **/eV**
Tungsten (**W**)	4.52	–
Thorium (**Th**)	3.4	3.0
Lanthanum (**La**)	3.5	2.7

welding, tungsten electrodes are often doped with oxides to decrease the work function and enhance electron emission. Conversely, as found in pure tungsten (4.5 eV), a higher work function can maintain a higher cathode tip temperature, which might help avoid cathode deposits, as indicated in Figure **4-17**. For operational stability, it is vital to refine the synthesis process to achieve stable arc operation without manual intervention. As suggested by the Richardson-Dushman equation, strategies to elevate the cathode tip temperature might involve using pure tungsten as an electrode, decreasing the electron-emitting area, or increasing the arc current.

4.3 Summary

Arc discharge synthesis is industrially relevant due to its low cost and scalability potential. The synthesis of copper nanoparticles in the gas phase via the arc discharge method was investigated to examine the balance between particle yield and size. Copper nanoparticles were continuously synthesized at a production rate of 1.2 to 5.5 g/h. Both the production rate and the average primary particle size depend on production parameters such as applied current and carrier gas flow. The freshly produced copper nanoparticles were found to have a surface oxide layer of 2 nm, comparable to those produced through wet-chemistry techniques. For their further application in conductive inks, copper nanoparticles with a Brunauer-Emmett-Teller (BET) size smaller than 60 nm were selected to meet the practical requirements for a sufficient mass of Cu samples.

Titanium nitride nanoparticles were produced through direct current arc discharge in an atmospheric-pressure environment composed of N_2 and Ar. The investigation focused on how synthesis parameters such as quench gas velocity, composition, and arc current influence the quality, yield, and size of the particles. Higher quench gas velocities resulted in particles with primary sizes of 10-15 nm, while at lower velocities, particles of 20-50 nm were produced, as determined by SEM analysis. XRD results indicated that the produced particles, regardless of the nitrogen composition in the quench gas, exhibited nearly identical TiN phases, with crystallite sizes increasing by about 20 nm with higher nitrogen levels. The composition of the quench gas significantly affected both arc voltage and particle production rate; a rise in nitrogen concentration from 20 % to 100 % tripled the production rate. Additionally, increasing the arc current from 12 A to 50 A led to a tenfold increase in yield, although it had a limited effect on primary particle size, according to BET measurements. The particle production rate increased primarily due to larger agglomerate sizes and higher agglomerate number concentrations. Furthermore, a mechanism to explain the growth of deposits on the cathode tip was proposed, supported by experimental observations and previous studies.

5 Conductive films prepared from arc synthesized Cu NPs

One application of metal nanoparticles is in the production of conductive inks used for printing electronic devices. Metallic copper nanoparticles are considered an economical alternative to gold and silver nanoparticles due to their high conductivity. As demonstrated in Chapter 4, high-purity metallic copper nanoparticles can be produced in high yields using arc discharge methods. However, unlike copper nanoparticles (Cu NPs) synthesized through traditional chemical methods, our synthesized particles lack a surfactant as a protective layer on their surface. Consequently, it is uncertain whether they are suitable for use in conductive inks. This chapter investigates the feasibility of fabricating conductive inks with particles synthesized via the arc discharge method. A ball milling technique was employed to produce copper conductive inks and explored the impact of milling parameters on ink stability. Additionally, a sintering method was developed to eliminate ink residues and copper oxides, thereby enhancing the electrical conductivity of the copper films. The research detailed in this chapter has been published in the peer-reviewed journal *Nanotechnology* [43].

5.1 Experimental details

The entire experimental process used in this work for fabricating copper conductive thin films is summarized in Figure **5-1**. Copper nanoparticles (Cu NPs), synthesized through the arc discharge method, were directly collected from a filter. These nanoparticles were then used to prepare conductive copper inks and films. The synthesis and characterization of Cu NPs have been thoroughly discussed in the previous section (Section 4.1). This chapter presents the procedure for preparing Cu inks and thin films. Additionally, the newly developed reductive sintering method is also demonstrated.

5.1.1 Preparation of copper conductive inks

Copper nanoparticles (2.8 g) collected from the arc reactor were added to a mixed solvent consisting of ethanol (2.1 g), glycerol (1.05 g), and isobutanol (1.05 g), achieving a metal loading of 40 wt. % in the ink. Glycerol, isobutanol, and ethanol, all of analytical grade, were

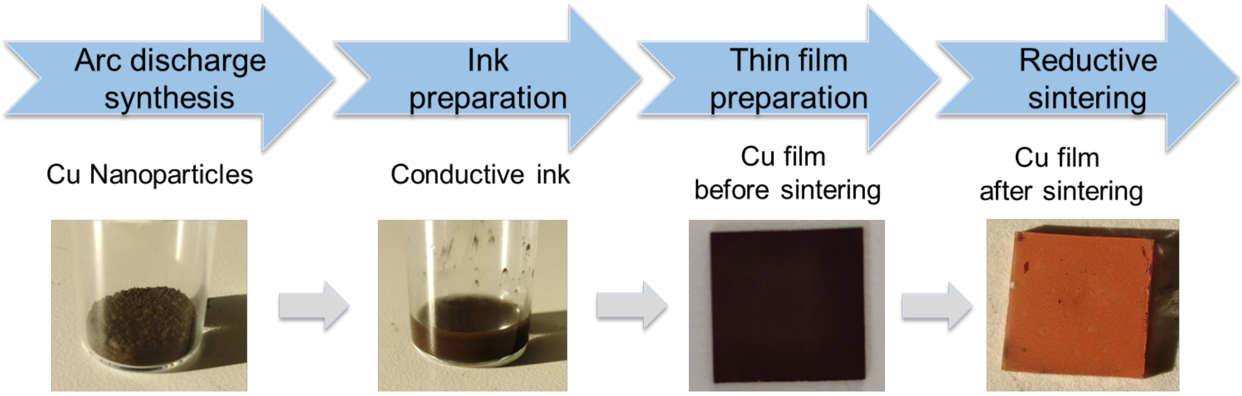

Figure **5-1**: Comprehensive experimental procedure for preparing highly conductive copper thin films

used without further purification. To deagglomerate the copper particles in the solvents, a high-energy ball mill (Mixer Mill MM400, Retsch GmbH, Germany) was utilized. Zirconia grinding beads, each with a diameter of 300 µm, were added to assist in reducing the copper agglomerates. The grinding jars used in this work have a 10 ml capacity. The ball milling parameters (milling time, vibrational frequency, and bead-to-copper powder weight ratio) were varied to obtain a relatively stable conductive ink. Table **5-1** details the milling parameters and corresponding ink components. After ball milling, the ink was extracted using a suction syringe connected to a standard cannula (0.8×80 mm). Due to the high particle loading of the prepared inks, observing sedimentation visually is challenging. Therefore, a gravimetric method was applied to assess the stability of the copper inks. 50 µl of dispersion was extracted from the upper layer of the inks every 24 hours and weighed it using an analytical balance (XS205, Mettler-Toledo AG, Switzerland), with the first measurement taken five hours after collecting the produced inks. A reference dispersion (Table **5-1**) without Cu nanoparticles was also prepared and weighed. The copper mass fraction is calculated using the following equation:

$$\omega_{\mathrm{Cu}} = \frac{m_{\mathrm{ink}} - m_{\mathrm{ref}}}{m_{\mathrm{ink}}} \times 100\,\% \tag{5-1}$$

where ω_{Cu} is the copper mass fraction of the ink, m_{ink} and m_{ref} are the corresponding weight of 50 µl dispersion, respectively. The prepared inks were then used to produce thin copper films on glass chips (10mm×10mm) using the spin coating technique (Spin 150, SPS Europe B.V., Putten) in ambient air. All samples were accelerated rotationally to 6000 rpm during spin coating and continuously spun for one minute at this speed.

Table **5-1**: Dispersion components and ball milling parameters applied in this work. Reproduced from Fu et al. [43], with permission from Nanotechnology (Copyright 2020).

	Reference	**Ink-1**	**Ink-2**
Ethanol [wt. %]	30 %	30 %	30 %
Isobutanol [wt. %]	15 %	15 %	15 %
Glycerol [wt. %]	15 %	15 %	15 %
Copper NPs [wt. %]	–	40 %	40 %
Milling frequency [Hz]	–	30	30
Milling time [min]	–	180	50
Beads volume [ml]	–	4	1.5

5.1.2 Post-deposition treatment – Thermal sintering

Without sintering, the electrical conductivity of nanoparticle-based thin films is typically extremely low, often only one-millionth that of bulk metal. This is due to the absence of a continuous metallic structure. To address this, a sintering process was employed to eliminate ink residues and reduce the copper oxide content in the thin films, thereby forming a film with a continuous metallic state. As shown in Figure **5-2** (a), Cu nanoparticles and films were sintered using a laboratory-built sintering setup. In this setup, N_2 (with a minimum purity of 99.9995 %) served as the carrier gas, and analytical grade formic acid was used as the reducing agent in the bubbler. Figure **5-2** (b) displays the image of the custom-built bubbler, where the gas initially enters the formic acid solution through three thin tubes, each with a diameter of 0.8 mm, to facilitate gas bubbling. It then exits into the sintering furnace. The samples (copper nanoparticles and films) were annealed in a tubular furnace (MTF 12/38/250, Carbolite, England) at various temperatures, ranging from 200 °C to 300 °C, for 60 minutes. A ceramic boat served as the sample holder, placed in the middle of the tube furnace during the sintering process. The reductive gas flow (Q_1) of 50 sccm (Standard Cubic Centimeters per Minute) and the dilution gas flow (Q_2) of 500 sccm were regulated using mass flow controllers (MFC, EL-Flow, Bronkhorst, Ruurlo, Netherlands).

5.1.3 Analysis and measurement of copper particles and thin films

The characterization of Cu nanoparticles freshly synthesized via the arc discharge reactor is detailed in Chapter 4, Section 4.1. This chapter also describes the morphological changes of the particles after ball milling and sintering. The microstructures of both the ground copper particles and the sintered copper films were examined using a Scanning Electron Microscope

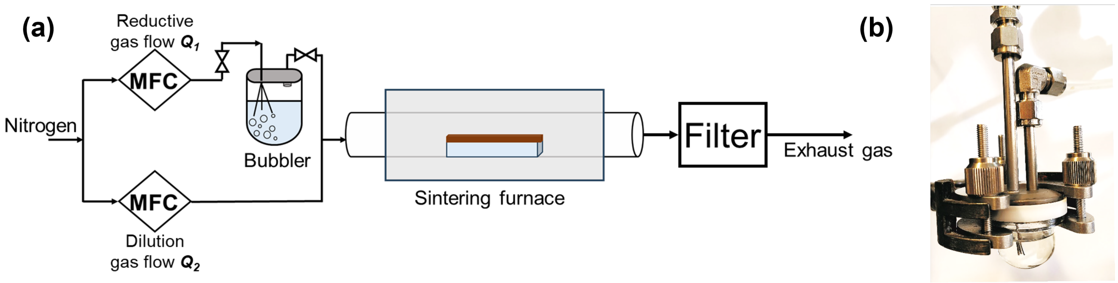

Figure **5-2**: (a) Experimental setup of sintering under reducing atmosphere with a dilution system and (b) Image of the self-built bubbler. Adapted from Fu et al. [43], with permission from Nanotechnology (Copyright 2020).

(SEM, JSM 7500F, Jeol, Tokyo). Elemental analysis for copper films was conducted using the same SEM, which is equipped with an Energy-Dispersive X-ray (EDX) Spectroscopy (Quantax, Bruker Nano GmbH, Germany) at 10 kV. X-ray Diffraction (XRD) measurements, employing a D8 Advance X-ray diffractometer (Bruker, USA) with $Cu{-}K\alpha$ radiation (1.5406 $\mathring{A}$), were used to confirm the crystal phases of copper films.

The electrical resistivity of the sintered copper films was calculated by multiplying the film thickness with its sheet resistance. This thickness was measured, both before and after sintering, using a stylus profilometer (XP-2000 Profilometer, Ambios Technology, CA, USA). To determine the sheet resistance of these sintered films, a four-point probe method (Keithley 4200 SCS, Cleveland, USA) was applied. The electrical conductivities reported in this work are averaged values derived from at least five separate measurements.

5.2 Effect of ball milling parameters on the ink stability

To explore their potential in the electronic printing of conductive patterns, the copper nanoparticles produced were used to create conductive inks through a ball milling technique. Since nanoparticles generated in the gas phase tend to form large agglomerates, the ball milling technique was employed to break down these agglomerates into smaller units, allowing them to be more stably dispersed in the solvents. While keeping the solvents used and the metal loading (40 wt. % Cu) constant, key milling parameters (as listed in Table **5-1**), including milling time and the volume of grinding beads, were varied to achieve a stable copper dispersion. For the purposes of this work, it was essential that the conductive ink remained stable for at least three days, meaning it should not exhibit significant precipitation.

Due to the high metal loading of the prepared dispersions, visually assessing their stability is challenging. In this work, the stability of the ink was evaluated by monitoring changes in the copper mass content in the upper layer of the dispersion. The gravimetric method employed

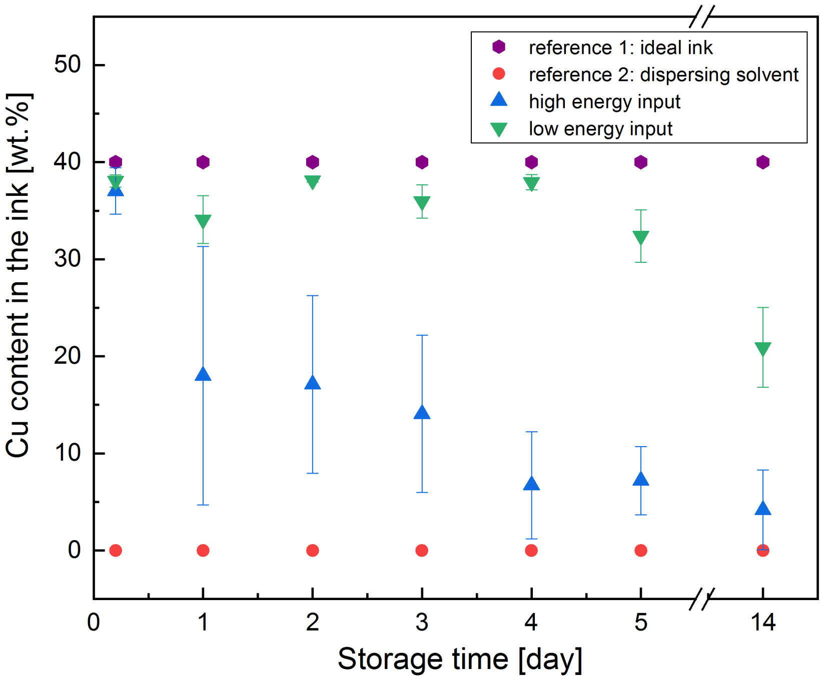

Figure **5-3**: Variation in copper mass content in the upper dispersion of copper inks prepared by low-energy milling (30 Hz, 50 minutes, 1.5 ml zirconia grinding beads) and high-energy milling (30 Hz, 180 minutes, 4 ml zirconia grinding beads), respectively. Reproduced from Fu et al. [43], with permission from Nanotechnology (Copyright 2020).

for this assessment is described in Section 5.1.1. Ideally, in the ink, Cu nanoparticles should remain homogeneously dispersed in the solvent, maintaining constant Cu mass content over time, indicating no particle sedimentation. However, over prolonged storage, Cu nanoparticles may collide due to Brownian motion, form larger agglomerates, and eventually settle under the influence of gravity. Thus, less stable inks will show a significant change in mass in the upper layer of the dispersion within a relatively short period. Figure **5-3** illustrates the variations in copper mass content in the upper layer of the dispersions for the produced copper inks. These inks were prepared using two different milling intensities: low-energy milling (Ink-2: 30 Hz, 50 minutes, 1.5 ml zirconia grinding beads) and high-energy milling (Ink-1: 30 Hz, 180 minutes, 4 ml zirconia grinding beads). It is observed that inks prepared with low-energy milling exhibited relatively better dispersion stability. As shown in Figure **5-3**, inks subjected to high-energy milling demonstrated significant precipitation after just one day of storage, with their metal loading decreasing to 20 wt. %. In contrast, the copper inks prepared with lower energy input maintained relatively stable conditions for up to five days, as indicated by a metal loading of over 30 wt. % in the upper dispersion. However, after five days, a noticeable change in mass was observed in the upper layer, and the metal loading dropped to approximately 20 wt. % after two weeks of storage. For further experiments involving the preparation of copper films In this work, copper inks produced via low-energy milling (Ink-2 from Table **5-1**) were utilized. Additionally, to ensure consistency, the inks were used within five days of preparation, maintaining a metal loading above 30 wt. %.

To investigate the reasons behind varying dispersion stabilities, SEM images were utilized to analyze the microstructure of copper nanoparticles after ball milling, as depicted in Figure **5-4**. Notably, the copper nanoparticles exhibit severe deformation and irregular geometry after high-energy milling, as illustrated in Figure **5-4** (b). This deformation is likely a result of the high-energy milling process and the inherent mechanical properties of the copper nanoparticles. As outlined by Joseph et al. [75] and Gertsman et al. [46], pure copper (a face-centered cubic, FCC, metal) demonstrates high ductility due to its efficient crystallographic slip system. In contrast, copper oxides (such as red cuprous oxide Cu_2O and black cupric oxide CuO) are brittle and tend to fracture when ground. Due to the minor presence of copper oxides, copper particles exhibit significant ductility. Under high-energy milling conditions (30 Hz, 180 minutes, 4 ml zirconia grinding beads), these freshly synthesized copper particles experience plastic deformation and re-weld into larger agglomerates. Conversely, particle agglomerates resulting from low-energy milling showed less plastic deformation compared to particles directly obtained from the arc reactor, as shown in Figure **5-4** (a). This observation suggests the existence of a threshold between milling energy input and the extent of deagglomeration for dispersed particles in the ink preparation process. Exceeding this threshold, higher energy input might cause nanoparticle deformation and re-welding. However, sufficient energy is still required to break down soft agglomerates for stable ink formation. Furthermore, the average size of copper agglomerates milled with high-energy input is noticeably larger than that of particles milled with lower energy. This difference could also account for the reduced stability of copper inks milled under high-energy conditions. However, even after low-energy milling, complete separation of copper aggregates into single primary nanoparticles is not achieved, as shown in Figure **5-4** (c). The presence of these agglomerates can expedite particle sedimentation, thereby reducing ink stability. In this work, the prepared copper inks have not been optimized for long-term storage. For their future use as conductive inks, it is crucial to decrease the size of these copper agglomerates further to enhance ink stability.

Two strategies can be considered to enhance the stability of copper ink. Firstly, adding suitable stabilizers or capping agents could be beneficial, especially considering that the Cu nanoparticles, generated through the arc discharge method, do not have surfactants or ligands on their surface. Choosing the right liquid vehicle compositions for ink formulation might also help minimize particle agglomeration in the dispersion. Secondly, conducting a

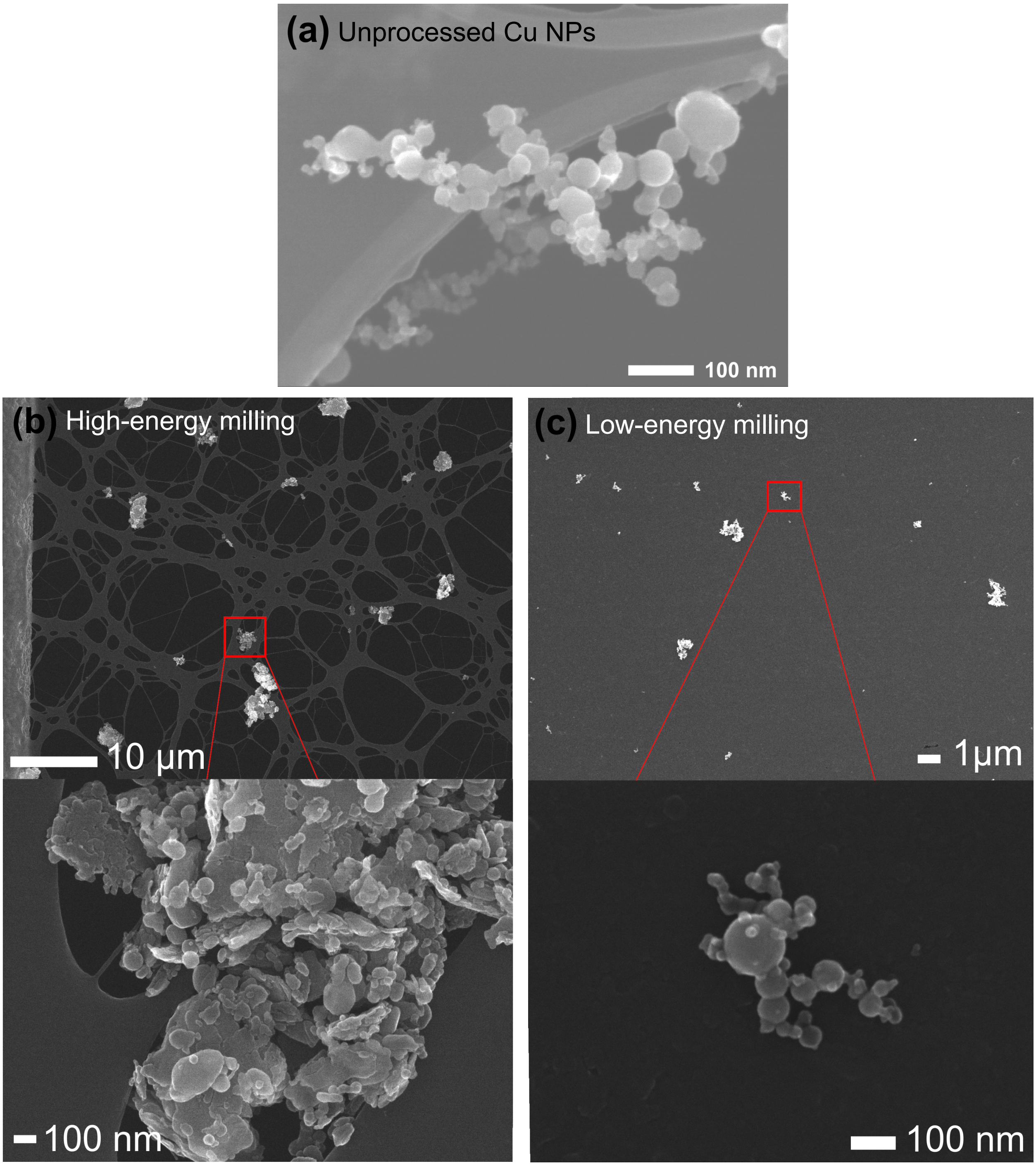

Figure **5-4**: SEM images showing the microstructures of (a) unprocessed particles collected from the arc reactor, (b) copper particles after milling with high-energy input (30 Hz, 180 minutes, 4 ml zirconia grinding beads); (c) copper particles after milling with low-energy input (30 Hz, 50 minutes, 1.5 ml zirconia grinding beads). Reproduced from Fu et al. [43], with permission from Nanotechnology (Copyright 2020).

detailed examination of milling parameters and exploring alternative methods for ink preparation is essential. It's important to highlight that this research primarily aims to establish the synthesized copper nanoparticles as a feasible alternative to silver and gold nanoparticles, as well as chemically synthesized copper nanoparticles, within the realm of printed electronics. Therefore, it's crucial to conduct an in-depth investigation into ink properties that are key to printing performance, including printability, viscosity, wettability, adhesion to various substrates, and long shelf life, tailored to specific application needs.

5.3 Effect of sintering atmosphere on copper nanoparticles

Printed patterns created using nanoparticle inks are expected to exhibit high electrical conductivity, ideally close to that of bulk metal. However, a significant improvement in the electrical conductivity of these printed patterns is only achieved when there is a continuous interconnection between the metallic nanoparticles. Therefore, post-printing thermal treatment, such as in a sintering furnace, is typically employed to bond these nanoparticles and form a connected structure. As discussed in Chapter 4 (Section 4.1.2), even freshly synthesized copper nanoparticles (after three days) are covered with a two-nanometer surface oxide layer. This oxide layer can diminish the electrical conductivity of the printed patterns. Additionally, the presence of copper oxides, which have higher melting points (Cu_2O at 1232 °C and CuO at 1326 °C) compared to copper (1085 °C) [206], necessitates higher sintering temperatures. Consequently, sintering in a reducing atmosphere is used to decrease or eliminate the copper oxide surface layer.

To explore the impact of the sintering atmosphere on copper nanoparticles, specific experiments were conducted. The copper nanoparticles, prepared as described, were sintered under a nitrogen atmosphere and a diluted reducing gas for 60 minutes at 300 °C. The nitrogen atmosphere had a gas flow of 500 sccm (Standard Cubic Centimeters per Minute). The setup for sintering under a diluted reducing gas is shown in Figure **5-2**, where the reducing gas flows through the bubbler at 50 sccm, with a nitrogen dilution gas flow of 500 sccm. Formic acid was chosen as the reducing agent in the bubbler, as it reacts with copper oxides, and the resulting organic copper salt is reduced to elemental copper during the sintering process [31]. Kim et al. [88] reported that a gaseous mixture of 70 % formic acid and 30 % alcohol as the reducing gas achieved printed copper patterns with low resistivity (approximately $4\,\mu\Omega \cdot \mathrm{cm}$). However, this method resulted in partially etched copper films. To mitigate this etching issue, a dilution gas flow was therefore introduced to minimize the etching of reduced copper nanoparticles during sintering under the reducing gas.

Figure **5-5** illustrates the microstructural evolution of copper nanoparticles after sintering under both nitrogen and reducing atmospheres, as observed through scanning electron microscopy. Sintering under a nitrogen atmosphere resulted in only partial necking between

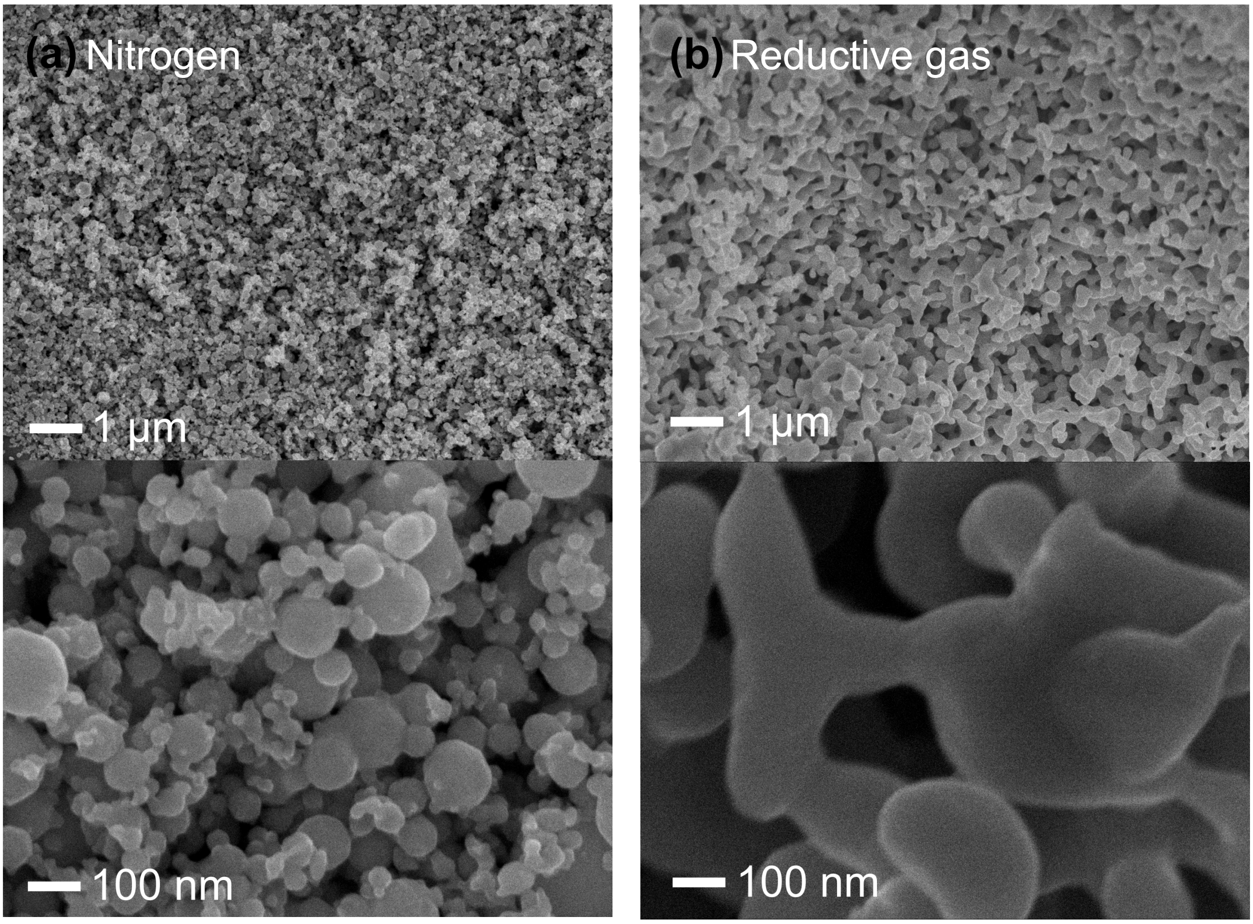

Figure **5-5**: SEM images of copper nanoparticles: (a) sintered under a nitrogen atmosphere; (b) sintered under diluted reducing atmosphere. Reproduced from Fu et al. [43], with permission from Nanotechnology (Copyright 2020).

smaller-sized nanoparticles, as evident in Figure **5-5** (a). In contrast, as shown in the scanning electron microscopy images in Figure **5-5** (b), copper nanoparticles formed a connected structure when sintered under diluted reducing gas. These microstructural findings indicate that using formic acid as the reducing agent effectively removes the oxide layer on the surface of the copper nanoparticles. Consequently, this allows for efficient sintering of the nanoparticles without the need to increase the sintering temperature.

5.4 Electrical resistivity of sintered copper thin films

The effect of sintering temperature on the electrical resistivity of printed copper films was thoroughly analyzed, as shown in Figure **5-6**. All copper films prepared from Ink-2 (as summarized in Table **5-1**) were sintered in a reducing atmosphere for one hour. The electrical resistivity of these films showed a significant decrease, from 46.3 ± 1.4 µΩ·cm to 5.4

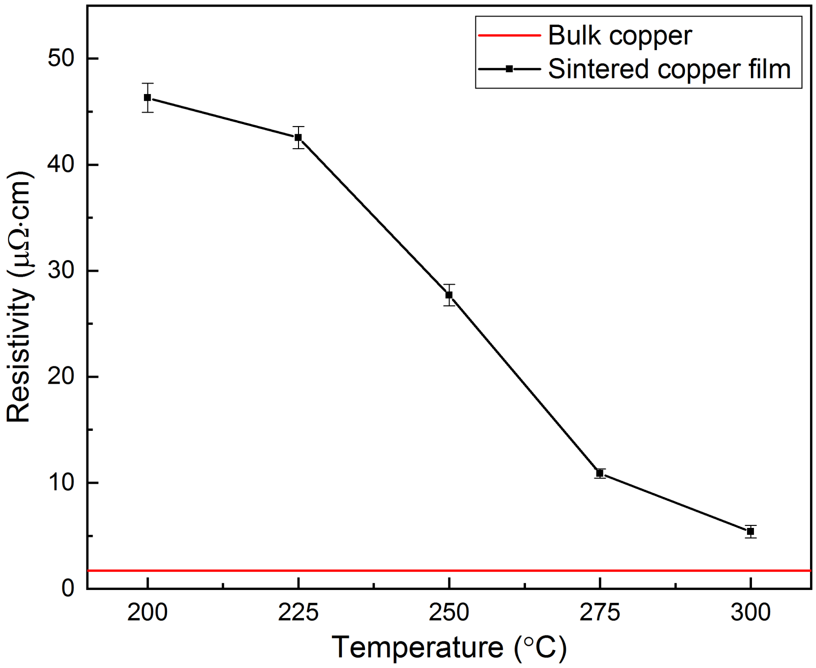

Figure **5-6**: Electrical resistivity of copper films sintered at varied temperatures, while all the copper films were sintered for one hour under diluted reducing gas. Reproduced from Fu et al. [43], with permission from Nanotechnology (Copyright 2020).

± 0.6 μΩ·cm, as the sintering temperature was raised from 200 °C to 300 °C. The minimum resistivity observed in films sintered at 300 °C suggests that the reducing gas was effective in removing surface oxides from the copper particles, thereby improving the electrical conductivity of the sintered films. Conversely, films sintered at lower temperatures exhibited higher electrical resistivity, likely due to the retention of organic residues from the ink formulation. This is particularly relevant for solvents like glycerol, which has a boiling point of 290 °C and may not fully evaporate at sintering temperatures below 290 °C. The commonly used methods for synthesizing copper nanoparticles predominantly involve the chemically controlled reduction of copper precursors. The synthesis of copper nanoparticles in the gas phase and their use in conductive inks have been less frequently reported. For a more comprehensive comparison, Table **5-2** compiles various studies focused on the electrical resistivity of printed copper patterns fabricated using chemically synthesized nanoparticles. For instance, Jeong et al. [70] and Park et al. [152] achieved electrical resistivities greater than $10\,\mu\Omega\cdot\text{cm}$ by sintering printed copper films at 325 °C under vacuum. Kang et al. [80] attained a low electrical resistivity of $3.67\,\mu\Omega\cdot\text{cm}$ by sintering printed electrodes in nitrogen at 200 °C, attributing this low resistivity to multiple printing layers, which helped reduce pre-existing

Table **5-2**: Comparison of the electrical resistivity of printed copper films with published reports. Adapted with permission from Fu et al. [43], as published in Nanotechnology (Copyright 2020).

Author	**Particle size**	**Thickness**	**Sintering**	**Resistivity**
Kamyshny et al. [78]	Bulk copper	–	–	1.72 µΩ · cm
Kang et al. [80]	10 nm	3736 nm	200 °C, Nitrogen	3.67 µΩ · cm
Jeong et al. [70]	~ 60 nm	–	325 °C, vacuum 10^{-3} Torr	11.5 µΩ · cm
Park et al. [152]	~ 45nm	–	325 °C, vacuum 10^{-3} Torr	17.2 µΩ · cm
Kim et.al. [88]	7 nm	–	200 °C, reducing atmosphere	4 µΩ · cm
This work [43]	~ 50 nm	~ 1000 nm	300 °C, reducing atmosphere	5.4 µΩ · cm

cracks and create a uniform thin layer. Similarly, Kim et al. [88] utilized formic acid as a reducing agent during sintering and achieved a low resistivity of 4 µΩ · cm at 200 °C, using 7 nm Cu nanoparticles, which are more conducive to low-temperature sintering due to their higher surface atom proportion compared to larger nanoparticles [80].

In this work, copper nanoparticles with an average diameter of 50 nm, as measured by Brunauer-Emmett-Teller (BET) analysis, were utilized to prepare copper films. These films were then sintered at 300 °C in a reducing atmosphere, resulting in a low electrical resistivity of 5.4 µΩ · cm. This resistivity is approximately three times higher than that of bulk copper, leading to the conclusion that copper inks made from gas-phase synthesized particles are competitive with those prepared from chemically reduced copper nanoparticles in terms of printed pattern resistivity.

Figure **5-7** presents SEM micrographs showcasing the surface morphology of copper films before and after sintering. These images confirm that the copper nanoparticles have fused to form a continuous film structure. Nevertheless, numerous pores were detected in the sintered films, which could act as non-conductive impurities within the conductive film. This might explain why the electrical resistivity of the copper films is 5.4 µΩ · cm, approximately three times higher than that of bulk copper (1.7 µΩ · cm), despite the removal of copper oxides. The research discussed in Chapter 6 focuses on addressing the issue of porosity in the sintered films, aiming to minimize their porosity and consequently lower the electrical resistivity of the copper films.

Energy Dispersive X-ray (EDX) spectroscopy was utilized to ascertain the elemental composition of the copper films. The EDX spectra, as shown in Figure **5-8** (a), reveal the presence of oxygen and carbon in addition to copper in the unsintered copper films. However, after

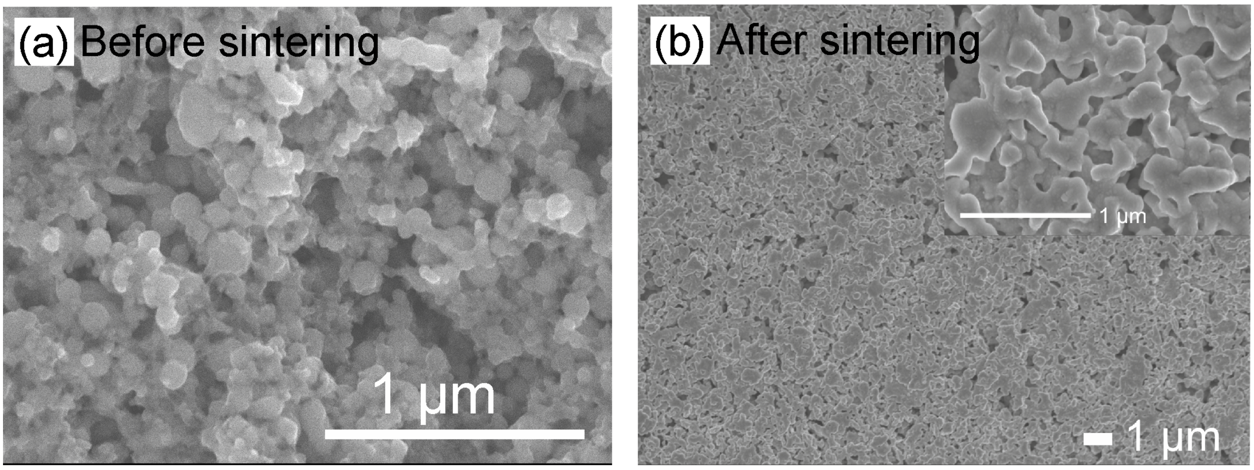

Figure **5-7**: (a) SEM image of a copper film before sintering; (b) SEM images of copper films after sintering, while the sintering parameters were maintained constant (300 °C, 1 hour, diluted reducing gas). Adapted from Fu et al. [43], with permission from Nanotechnology (Copyright 2020).

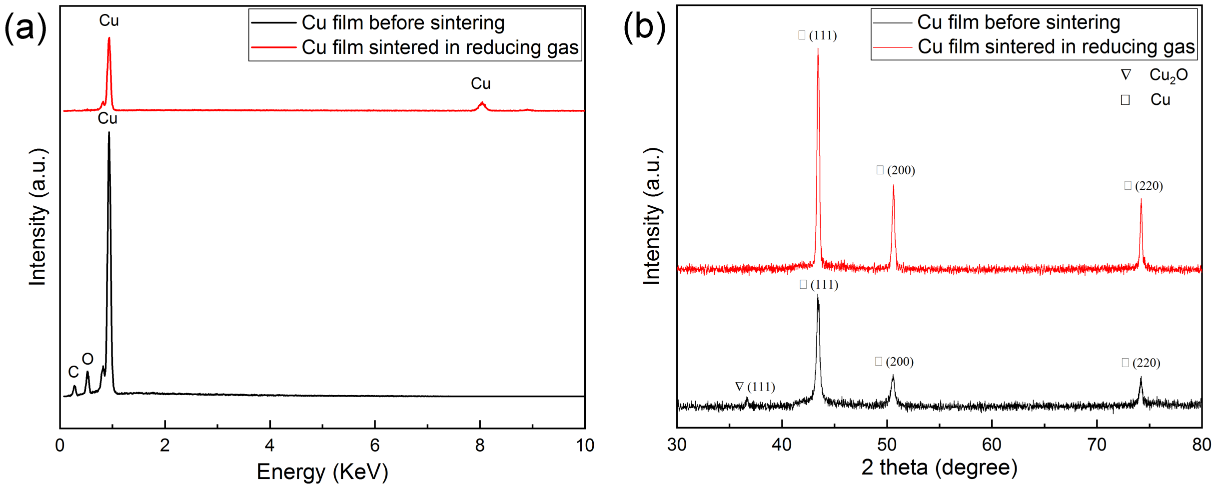

Figure **5-8**: (a) XRD patterns of copper films before and after sintering; (b) EDX spectra of copper films before and after sintering, while the sintering parameters were maintained constant (300 °C, 1 hour, diluted reducing gas). Adapted from Fu et al. [43], with permission from Nanotechnology (Copyright 2020).

sintering in a reducing atmosphere at 300 °C for one hour, the EDX spectrum exhibited only the presence of copper, signifying the complete removal of organic residues from the copper inks during sintering. Additionally, X-ray Diffraction (XRD) was employed to determine the crystalline phases of the prepared copper films. The XRD data of the spin-coated copper film before sintering, as seen in Figure **5-8** (b), predominantly shows diffraction at 43.4°, 50.5°, and 74.0°, characteristic of copper with face-centered cubic (FCC) symmetry. A minor peak at 36.6°, corresponding to the (111) plane of Cu_2O, was also observed. Notably, XRD analysis of freshly synthesized nanoparticles did not show characteristic Cu_2O peaks, indicating that copper oxides mainly form during the ball milling and spin coating processes, which are conducted in ambient air. In contrast, after sintering in reducing gas, the Cu_2O diffraction peak vanishes from the XRD data, leaving only copper diffractions. This outcome further confirms that formic acid effectively reacts with and removes the surface oxide of the copper nanoparticles.

Sintering in a reducing atmosphere can potentially pose an etching issue, particularly in flexible electronics that utilize bendable substrates such as plastic or paper. As previously mentioned, minimizing the oxidation of copper nanoparticles can be achieved by storing them in an inert gas and reducing their exposure to oxygen. Nonetheless, the formation of a thin oxide layer on the surface of the particles is almost unavoidable. This layer must be reacted with and removed to achieve high electrical conductivity in copper films. An alternative approach to sintering in a reducing atmosphere is to incorporate a reducing agent during the copper ink preparation process, followed by sintering the printed pattern in a nitrogen atmosphere or under vacuum. Notably, Deng et al. [31] have successfully developed an antioxidative copper paste using lactic acid as the reducing agent. The resulting copper films, sintered in nitrogen, exhibited antioxidative properties.

5.5 Summary

The synthesis of nanoparticles via transferred arc discharge is industrially significant due to its cost-effectiveness and scalability potential. In this chapter, it is shown that copper nanoparticles synthesized through the arc discharge method are suitable for use in printed electronics, particularly regarding their electrical conductivity. To assess their applicability in electronic printing, a ball milling technique was applied to prepare copper conductive inks. The effect of ball milling parameters on the dispersion stability and particle morphology in the inks was detailed investigated. Copper inks prepared with lower energy input (30 Hz, 50 minutes, 1.5 ml zirconia grinding beads) demonstrated improved dispersion stability, attributed to the reduced size of agglomerates. These inks were then used to produce thin films via spin coating. The use of formic acid as a reducing agent proved effective in reacting with the surface oxide of the copper nanoparticles, facilitating the formation of a connected structure in the sintered film. The copper films sintered in a diluted reducing gas exhibited a low electrical resistivity of 5.4 ± 0.6 $\mu\Omega \cdot \mathrm{cm}$, indicating their potential as substitutes for silver or gold inks. Furthermore, it can be concluded that conductive inks made from gas-phase synthesized copper nanoparticles are competitive with those made from chemically synthesized copper nanoparticles.

6 Highly conductive copper films prepared by multilayer sintering

The primary challenges in producing highly electrically conductive copper (Cu) films lie in managing the oxide content and reducing the porosity of these sintered films. In Chapter 5, the potential of using nanoparticles synthesized via arc discharge for preparing copper inks was established, and a developed reducing sintering method was used to eliminate the oxide content in copper films effectively. This chapter aims to enhance further the electrical conductivity of printed copper films by preparing a denser copper film, realized by reducing film porosity. To achieve this, a multilayer-sintering method that involves repeating coating and thermal sintering processes up to four times was developed. Using this method, one can systematically explore the relationship between porosity and electrical resistivity in the sintered copper films, guided by experimental findings. The work detailed in this chapter has been published in the peer-reviewed journal *Nanotechnology* [42].

6.1 Experimental details

This research is a continuation of the work presented in the previous chapter. The comprehensive procedure for fabricating copper (Cu) thin films using copper nanoparticles synthesized through arc discharge was outlined in the preceding section. Detailed information on the synthesis and characterization of these Cu nanoparticles is available in Chapter 4 (Section 4.1), and the reducing sintering method is elaborated on in Chapter 5 (Section 5.1). This section focuses on the experimental aspects critical for refining the sintering process. This includes the preparation of inks to control film thickness, the implementation of a multiple sintering process, and the characterization of the thin films.

6.1.1 Fabricating copper inks

Since the optimization of conductive inks relies on specific product requirements, this work focuses on modifying existing ink formulations to produce copper films with varying thicknesses, rather than optimizing ink performance. The thickness of films created through

Table **6-1**: Formulations of copper inks used in the multilayer sintering study. Reproduced with permission from Fu et al. [42], as published in Nanotechnology (Copyright 2023)

	Ink-1	**Ink-2**	**Ink-3**
Ethanol [wt. %]	37.5	37.5	37.5
Isobutanol [wt. %]	18.75	18.75	18.75
Glycerol [wt. %]	18.75	6	3
Ethylene glycol [wt. %]	–	12.75	15.75
Copper NPs [wt. %]	25	25	25
Total weight of the ink [g]	8	8	8

spin-coating depends on the concentration of solid materials and solvent properties like viscosity and evaporation rate. The glycerol to ethylene glycol ratio in the inks was adjusted to vary the thickness of the resulting Cu films, exploiting their significant difference in viscosity. The compositions of these inks are detailed in Table **6-1**. Each prepared Cu ink contains 25 wt. % metal loading and uses analytical-grade ethanol, isobutanol, glycerol, and ethylene glycol, without further purification.

Copper nanoparticles (Cu NPs) collected from the arc discharge reactor were initially mixed with the solvents listed in Table **6-1**. This mixture was stirred using a magnetic stirrer (MR Hei-Standard, Heidolph Instrument, Germany) at 1000 rpm and 30 °C for one hour. Subsequently, the mixture was sonicated for an hour using an ultrasonic processor (UP100H, Hielscher Ultrasonics GmbH, Germany) to disperse any agglomerates, with an amplitude setting of 100 and a cycle of 0.9. The sonication took place in an ice-water bath to prevent ink overheating. The resulting inks could pass through a 0.7 µm syringe filter but not a 0.45 µm one, indicating agglomerate sizes between 450 nm and 700 nm. These inks remained stable for three days at room temperature. If necessary, a 15-minute re-sonication after three days allowed for their reuse.

6.1.2 Sintering and characterizing copper thin films

Copper films were initially fabricated using a spin coating machine (Spin 150, SPS Europe B.V., Putten, Netherlands). 10 µL of the previously prepared inks was carefully dispensed drop by drop onto a 10 mm × 10 mm glass substrate (Menzel Cover Glasses, Thermo Fischer Scientific, U.S.). The substrates were accelerated to 7000 rpm during the spin coating process and maintained at this speed for two minutes. This was followed by a thermal treatment (thermal sintering) to evaporate the organic solvents and transform the copper particles into a cohesive metallic layer. The sintering procedure, detailed in Section 5.1.2 of the previous chapter, employed nitrogen (with a minimum purity of 99.995 %) as the carrier gas and formic acid of analytical grade as the reducing agent. In this work, all copper films underwent sintering at 300 °C in a diluted reducing atmosphere, with a consistent gas flow rate. The sintering duration was varied to examine its impact on the electrical resistivity of the copper films. To minimize film porosity, a single-layer copper film was first sintered for an hour. This was followed by an additional spin coating and sintering for another hour to produce a two-layer film. These steps were repeated to obtain three- or four-layer sintered film samples.

The electrical resistivity of the sintered copper (Cu) films was determined by measuring the sheet resistance and film thickness. The sheet resistance was measured using a four-point probe method with a Keithley 4200 SCS (Keithley Instruments, Cleveland, USA), and the film thickness was determined using a stylus profilometer (XP-2000, Ambios Technology, CA, USA). Measurements for both thickness and sheet resistance were taken at three different locations on each film sample, and their averages were calculated from these values. Additionally, the surface and cross-sectional microstructures of the sintered Cu films were examined using a secondary electron (SE) detector in a scanning electron microscope (SEM, JSM 7500F, Jeol, Tokyo, Japan). Elemental analysis of the copper films was performed using the same SEM, equipped with an energy-dispersive X-ray (EDX) spectrometer (Quantax, Bruker Nano GmbH, Germany), operating at 10 kV.

Furthermore, the porosity of the Cu thin films was determined using image analysis software, ImageJ, applied to selected low-resolution SEM images at magnifications of 5000x and 10000x. The SEM images were initially converted into binary black-and-white images through a manual threshold setting. In these binary images, black areas represent pores, while white areas indicate the dense copper film. Consequently, the surface porosity of the film was calculated by dividing the total area of the pores by the overall image area. For this analysis, at least five SEM images at each magnification level were used to assess the average porosity of each film sample accurately.

6.2 Effect of sintering time on the resistivity of single-layer Cu films

Generally, Cu films prepared by direct printing/deposition techniques exhibit low electrical conductivity due to the presence of ink dispersants and pores among nanoparticles (NPs). As a result, post-deposition treatment of Cu films is necessary to eliminate ink solvents and ensure continuous interconnection among copper particles. The effective removal of ink residues and Cu oxides after reducing sintering at 300 °C for one hour has been confirmed based on the film components measurement by EDX and XRD. However, the evolution of film porosity and film resistivity remains unclear. Therefore, the electrical resistivity of the Cu

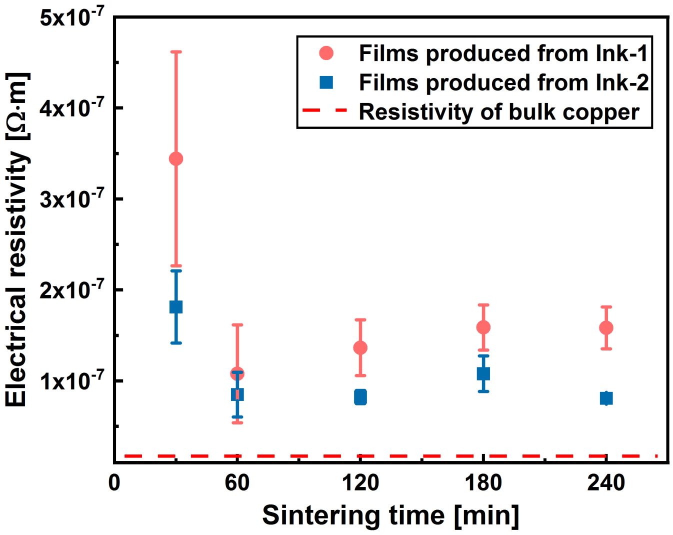

Figure **6-1**: Electrical resistivity of the Cu films as a function of sintering time, where the sintering temperature is kept constant at 300 °C. Reproduced from Fu et al.[42], with permission from Nanotechnology (Copyright 2023).

films was investigated as a function of sintering time to determine if extended sintering time aids in reducing film porosity. In this work, all prepared Cu films were thermally sintered in a reductive atmosphere at 300 °C. The electrical resistivity of the Cu films was examined in relation to sintering time, ranging from 30 minutes to 240 minutes. For each sintering duration, one-layer Cu films were prepared using two different 25 wt. % Cu inks (Ink-1 and Ink-2 in Table **6-1**), where the ratio of the dispersion solvents glycerol and ethylene glycerol was varied. As shown in Figure **6-1**, the electrical resistivity significantly decreased from $34.4\,\mu\Omega\cdot\mathrm{cm}$ after 30 minutes to $10.8\,\mu\Omega\cdot\mathrm{cm}$ after 60 minutes for ink 1, and from $18.1\,\mu\Omega\cdot\mathrm{cm}$ after 30 minutes to $8.49\,\mu\Omega\cdot\mathrm{cm}$ after 60 minutes for ink 2. The resistivity of the sintered Cu films reached its minimum value within one hour and remained almost constant, despite the sintering time extending from one hour to four hours for both inks. These findings suggest that the copper nanoparticles are fully sintered, and the impurities, including pores and organic residues, cannot be further reduced or minimized after sintering for one hour.

Figure **6-2** presents optical images of unsintered and sintered Cu films, subjected to various sintering times ranging from 30 minutes to 240 minutes. The unsintered Cu film displays a dark brown color, indicating slight oxidation of the Cu nanoparticles during collection and ink preparation. As the sintering process progresses, the film color transitions from dark brown (unsintered) to brown (30 minutes) and eventually to bronze-red (for one hour or more). The film color stabilizes after one hour of sintering, consistent with the observation that no further conductivity improvements occur with extended sintering times. Additionally, for

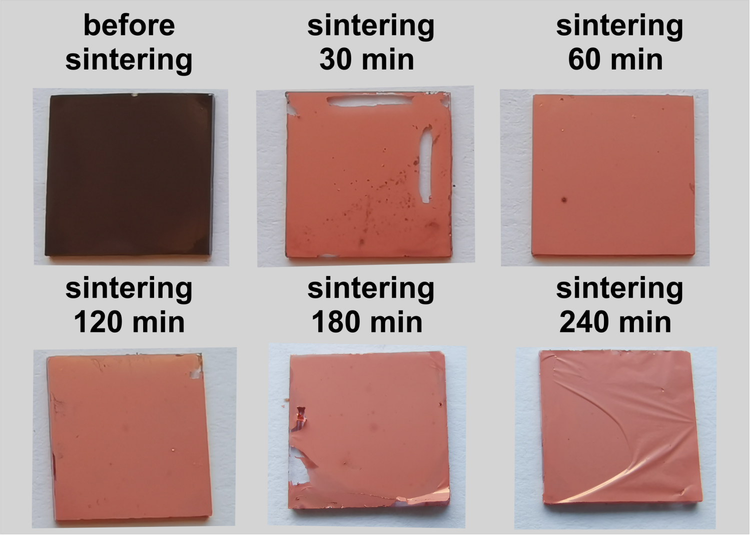

Figure **6-2**: Photos of copper films coated on the glass substrate before or after sintering at various sintering times. Reproduced from Fu et al. [42], with permission from Nanotechnology (Copyright 2023).

samples sintered less than two hours, no delamination was noted. However, delamination varied depending on film thickness, pre-existing cracks, and longer sintering durations.

It is important to note that cracks and delamination are significant issues in intense pulsed light (IPL) sintering, with numerous studies dedicated to addressing these challenges [18, 79, 49, 166]. The causes of delamination can be attributed to several factors. One key factor is material shrinkage due to high-temperature exposure over extended periods during sintering. When Cu nanoparticles are sintered on a rigid substrate, the material volume reduces, creating tensile stress across the thickness of copper layer, potentially leading to crack formation. Another contributing factor is the thermal decomposition or evaporation of organic solvents. An extended duration of the sintering process could provide sufficient time for the internal gases to be released from the sintered film, thereby intensifying the issue of volume shrinkage.

The surface morphologies of the copper films after various sintering durations were examined using SEM micrographs, as illustrated in Figure **6-3**. Figure **6-3** (a) presents an SEM image of the unsintered copper film following a 24-hour drying period in ambient air. In this state, copper particles are visible as agglomerates, where van der Waals forces bind spherical primary particles together. After 30 minutes of sintering (see Figure **6-3** (b)), most Cu particles appear interconnected, although some remain unsintered, evidenced by isolated copper islands and large, unevenly sintered pore boundaries. Extending the sintering to one hour (see Figure **6-3** (c)) shows a clear formation of an electrical percolation path, despite the presence of pores, and the pore boundaries appear smoother, indicating more complete sintering of the Cu particles.

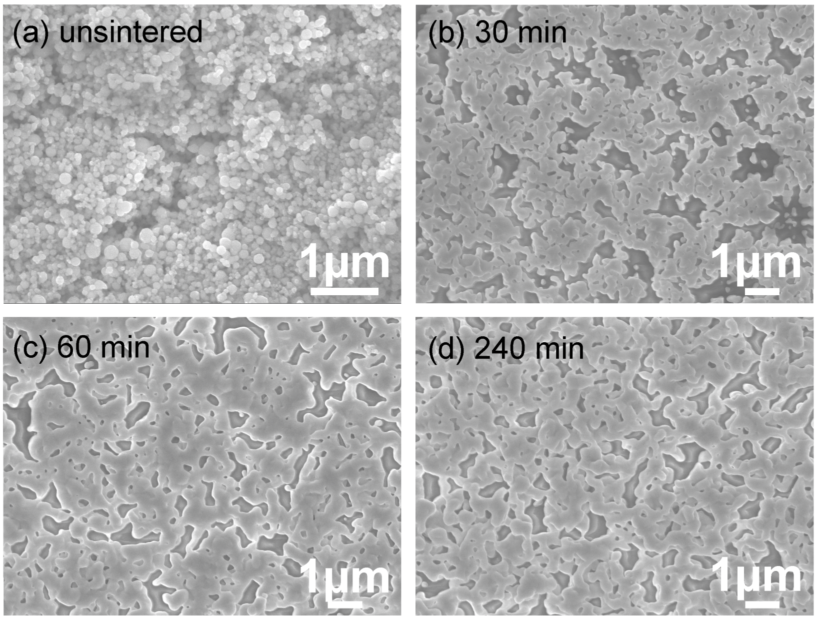

Figure **6-3**: Scanning Electron Microscope (SEM) images illustrating the microstructures of copper films at different stages: (a) before sintering, (b) sintered for 30 minutes, (c) sintered for one hour, and (d) sintered for four hours. Reproduced from Fu et al. [42], with permission from Nanotechnology (Copyright 2023).

In films sintered for four hours (see Figure **6-3** (d)), the structures appear well-sintered, with a slight decrease in pores larger than 1 μm and an increase in smaller pores, less than 1 μm. According to Sherer and Garino [170], films with lower porosity and smaller pores tend to experience more stress from a rigid substrate, a concept that aligns with the observed delamination of films after four hours of sintering. To minimize film delamination, all samples in subsequent studies were sintered for one hour.

6.3 Effect of copper film thickness on morphology and resistivity

Prior studies utilized copper inks with a 40 % metal loading, resulting in an average thickness of single-layer copper films around 1000 nm. In such thick films, refilling pores is challenging as nanoparticles struggle to penetrate and reach the underlying layers. Therefore, examining the impact of single-layer thickness on film resistivity is essential. Considering different printing/deposition methods require specific ink characteristics, this work primarily aimed to produce copper films of varied thicknesses. Under consistent spin coating process parameters, the thickness of the deposited Cu layer is influenced by the properties of the coating inks, such as metal loading and ink viscosity. This study developed three types of 25 wt. %

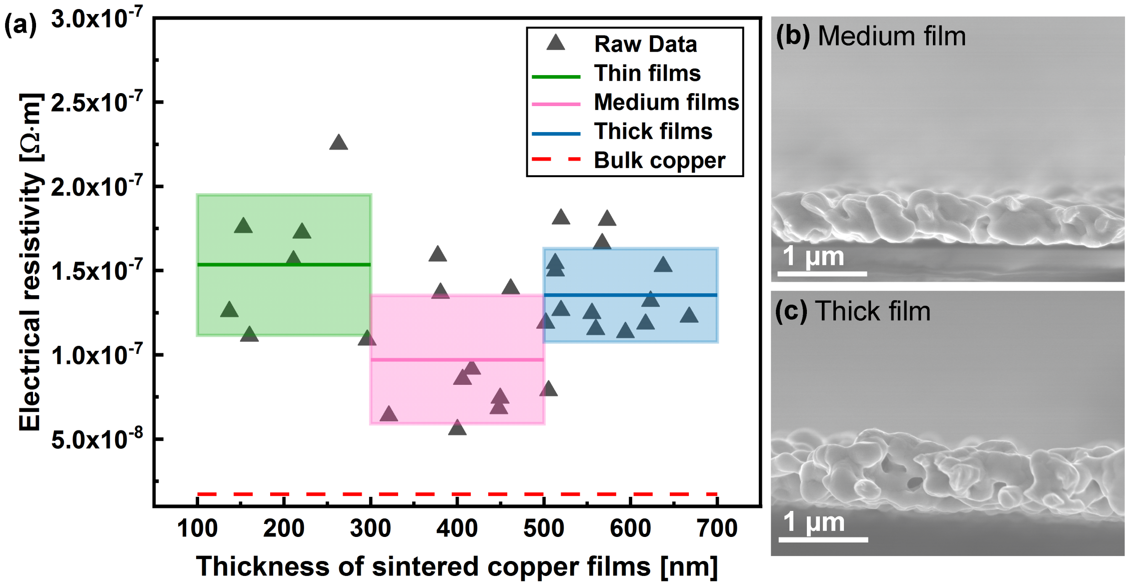

Figure **6-4**: (a) Electrical resistivity of copper films sintered for one hour across different thicknesses, accompanied by typical cross-sectional micrographs of a sintered Cu film with medium thickness (b) and a thicker film (c). Reproduced from Fu et al. [42], with permission from Nanotechnology (Copyright 2023).

concentrated Cu inks, adjusting the glycerol to ethylene glycerol ratio to achieve varying viscosities, as detailed in Table **6-1**. Typically, Ink-1 produced the thickest films at about 600 nm, Ink-2 resulted in medium-thickness films of around 400 nm, and films from Ink-3 were the thinnest at approximately 200 nm.

The electrical resistivity of the one-layer sintered copper films was analyzed in relation to film thickness, as shown in Figure **6-4** (a), with all sintering conducted at 300 °C for one hour. The single-layer sintered Cu films were categorized based on thickness: thin (100-300 nm), medium (300-500 nm), and thick (500-700 nm). The average electrical resistivities for these categories were $15.3\,\mu\Omega\cdot\text{cm}$, $9.70\,\mu\Omega\cdot\text{cm}$, and $13.5\,\mu\Omega\cdot\text{cm}$, respectively, with medium-thickness films exhibiting the lowest resistivity. Cross-sectional microstructures of medium and thick sintered Cu films, shown in Figures **6-4** (b) and **6-4** (c), reveal complete interconnection of Cu nanoparticles in both cases, though thicker layers exhibit more pores. These pores in thicker films may result from gases trapped during the thermal decomposition of ink constituents. Thinner films (< 500 nm) rarely contain trapped pores as decomposed organic additives can escape quickly to the film surface. Consequently, thicker films (500-700 nm) demonstrate higher electrical resistivity than medium films. Figure **6-4** (a) illustrates the considerable variation in the electrical resistivity of the sintered films. This variation could be due to the agglomerate size and homogeneity in the inks not being optimally adjusted.

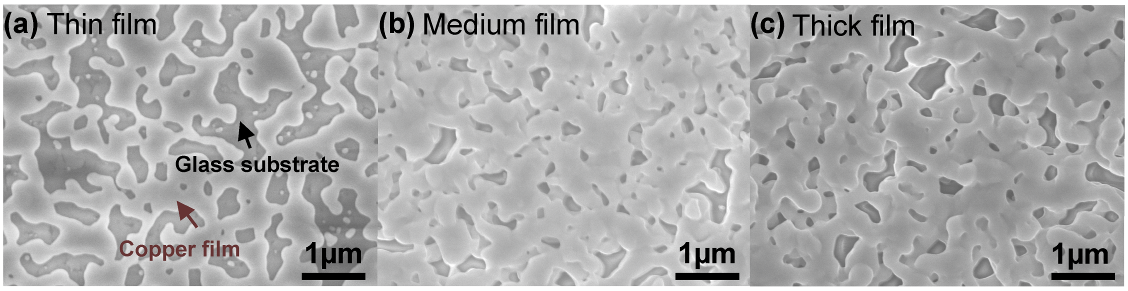

Figure **6-5**: Scanning Electron Microscope (SEM) images displaying the microstructures of films sintered for one hour at various measured thicknesses: (a) 153 nm, (b) 449 nm, and (c) 617 nm. Reproduced from Fu et al. [42], with permission from Nanotechnology (Copyright 2023).

The presence of these agglomerated particles in the inks can result in uneven surface profiles and contribute to the development of small cracks within the films.

To explore the causes of varying resistivities, Scanning Electron Microscope (SEM) analyses were conducted to examine the surface microstructures of films with different thicknesses, as shown in Figure **6-5**. The dominant presence of silicon in the glass substrate facilitated the identification of pores in the sintered copper films through elemental mapping analysis using an Energy-Dispersive X-ray (EDX) spectrometer. As seen in Figure **6-6**, areas identified as sintered copper nanoparticles, which appeared bright, were confirmed by comparing the distributions of silicon and copper elements. Notably, the copper film with a thickness of 153 nm (Figure **6-6** (a)) exhibited a larger number of pores, primarily larger than 1 µm in size. This higher porosity in the thinner films is likely the reason for their increased electrical resistivity. Figures **6-6** (b) and **6-6** (c) show copper layers with similar surface microstructures, characterized by smaller pores, mostly less than 0.7 µm in size. Additionally, it was observed that the ink layers were thick enough to cover any pre-existing cracks or voids, thereby ensuring continuous connectivity between the copper nanoparticles.

In the research presented in Chapter 5, copper inks with a 40 wt. % metal content were utilized to create single-layer films approximately 1000 nm thick. X-ray Diffraction (XRD) analysis of the copper films, conducted before and after sintering, revealed the disappearance of copper oxide diffraction peaks after sintering. This indicates the complete removal of copper oxides in a reducing gas atmosphere. Considering that all films used in the present study are thinner than 1000 nm, it is presumed that impurities resulting from copper oxidation are negligible after a reducing sintering process at 300 °C for one hour. Consequently, the variations in electrical resistivity are attributed to the differing porosities of the sintered films. The results depicted in Figure **6-4** (a) demonstrate that the resistivity of the film does not have a linear relationship with the thickness. An increase in the film thickness does not

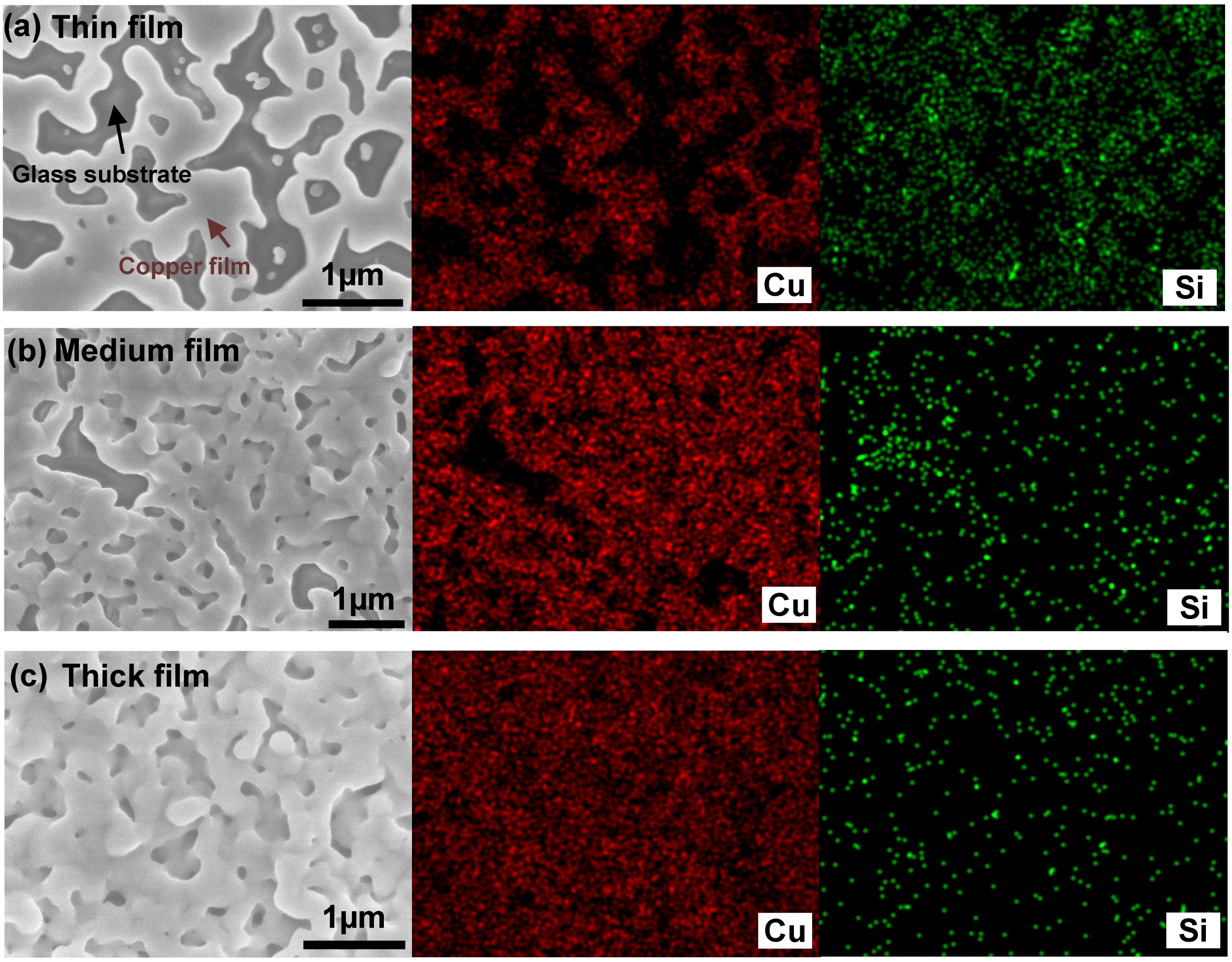

Figure **6-6**: Scanning Electron Microscope (SEM) images and corresponding elemental maps showcasing copper (Cu) and silicon (Si) distributions in a sintered Cu film at varying thicknesses: (a) 153 nm, (b) 449 nm, and (c) 617 nm. Adapted from Fu et al. [42], with permission from Nanotechnology (Copyright 2023).

consistently lead to a decrease in resistivity. Beyond a specific thickness, excessive pores in the copper film might significantly impede electron mobility, thereby affecting electrical conductivity. The threshold thickness is dependent on the properties of the ink, such as metal content, particle size, and the solvents used. In this work, the critical thickness is determined to be around 400 nm, as films exceeding this thickness exhibited higher electrical resistivity.

6.4 Effect of multilayer sintering on film porosity and resistivity

As mentioned earlier, the porosity observed in films post-sintering arises from volume shrinkage due to nanoparticle densification and the evaporation of organic components. This porosity is not substantially diminished by either extending the sintering duration or increasing the thickness of a single layer. Figure **6-6** (a) illustrates that the porosity in thin sintered Cu films is relatively high, with many pores exceeding 1 µm in diameter. Given that most copper agglomerates in the inks used are smaller than 0.7 µm, these larger pores could potentially be filled by applying a second coating followed by sintering. To investigate the potential reduction in porosity, the coating and sintering process was repeated up to four times, resulting in multilayer sintered copper films. Moreover, for effective pore filling in the sintered thin copper films, it is crucial to maintain the thickness of each layer below the critical threshold of 400 nm and as thin as possible. This approach ensures that the Cu particles can penetrate deeply into the base of the film.

In this context, Ink-3 (see Table **6-1**) was utilized to fabricate copper films with an approximate thickness of 200 nm. Figure **6-7** depicts the changes in the electrical resistivity of the copper films following each coating and sintering cycle. The resistivity of the films decreased significantly from $11.17 \pm 2.17\,\mu\Omega\cdot\text{cm}$ in single-layer sintered films to $3.49 \pm 0.35\,\mu\Omega\cdot\text{cm}$ in four-layer sintered films. Notably, this resistivity is about twice that of bulk copper, which is $1.72\,\mu\Omega\cdot\text{cm}$. Moreover, a correlation was observed between the reduction of porosity and the decrease in electrical resistivity in the sintered films. For this work, the surface porosity of the films, as representative of their overall porosity, was considered. This is based on the understanding that metal films exhibit uniform structure and volume shrinkage throughout their thickness after thermal sintering [110]. The porosity of the Cu films was reduced from 33.6 % after single-layer sintering to 3.7 % after four-layer sintering, demonstrating a notable decrease of approximately 30 % through the multilayer sintering approach.

Figure **6-8** presents the surface microstructures of the multilayer Cu films and their corresponding porosity, calculated using image analysis software. The results indicate a significant reduction in porosity for the films subjected to four coating layers and sintering, compared

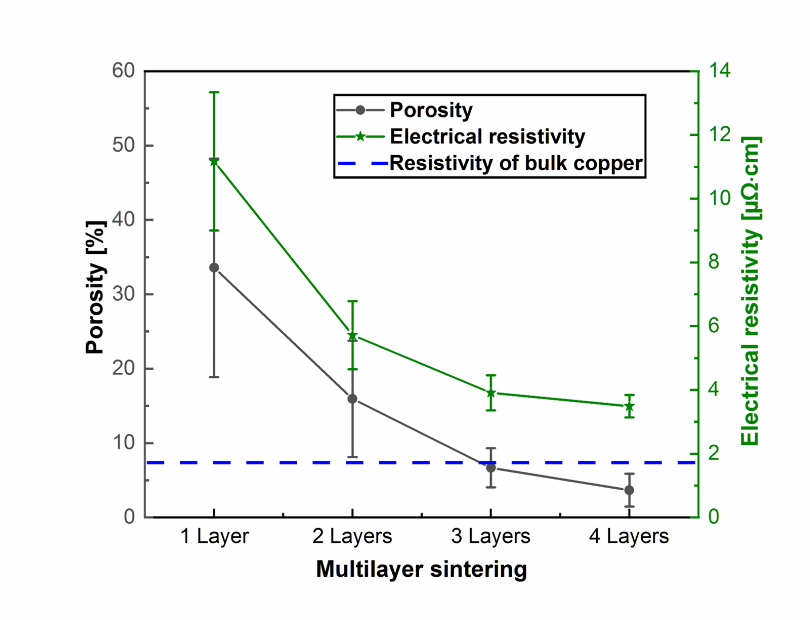

Figure **6-7**: Correlation of porosity and electrical resistivity with the number of coatings and sintered layers in copper films. Reproduced from Fu et al. [42], with permission from Nanotechnology (Copyright 2023).

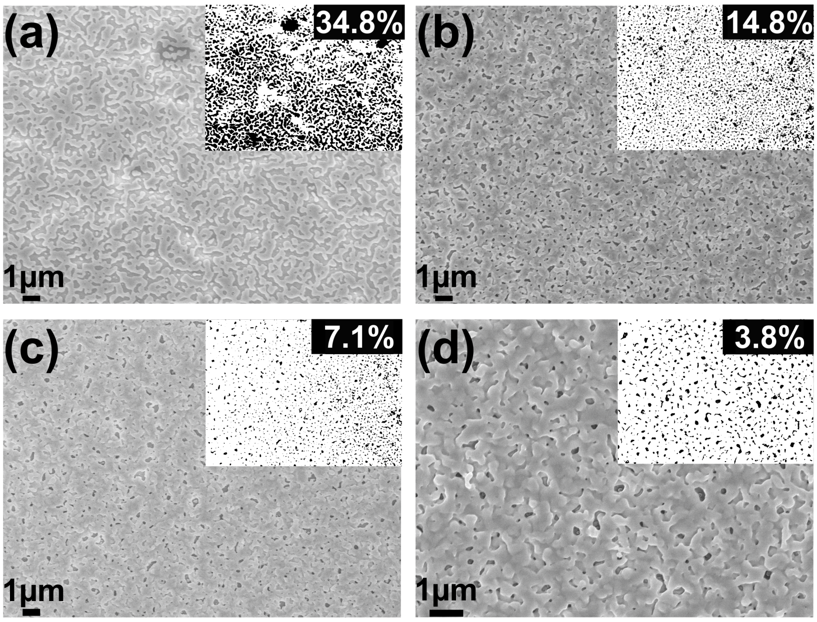

Figure **6-8**: Scanning Electron Microscope (SEM) images along with the calculated porosity of films after being coated and sintered (a) once; (b) twice; (c) three times; (d) four times. Reproduced from Fu et al. [42], with permission from Nanotechnology (Copyright 2023).

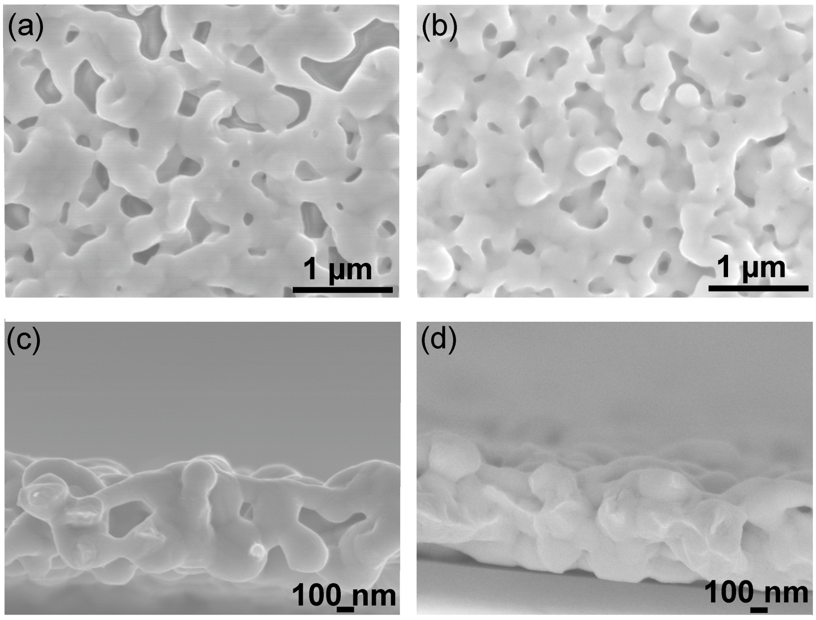

Figure **6-9**: The surface morphologies of Cu films after (a) single-layer sintering and (b) multilayer sintering, (c) and (d) are corresponding cross-sectional images, where their film thicknesses are similar. Reproduced from Fu et al. [42], with permission from Nanotechnology (Copyright 2023).

to those with just one layer. Furthermore, these microstructural analyses confirm that pores in the films can be effectively filled by successive coating and sintering, especially when the ink particles are smaller than the existing pores.

Cross-sectional micrographs of Cu films post-multilayer sintering were analyzed to enhance the understanding of the densification process. Figures **6-9** (a) and **6-9** (c) illustrate Cu films sintered with a single layer using Ink-1 in Table **6-1**, resulting in a thicker film (500-700 nm). In contrast, Figures **6-9** (b) and **6-9** (d) demonstrate that multilayer sintering of films of a similar thickness (approximately 600 nm) leads to a relatively uniform and dense microstructure. This increased density is responsible for the reduction in electrical resistivity observed.

This research observed that copper films with a porosity of less than 5 % were predominantly produced after four times of coating and sintering, as illustrated in Figure **6-8** (d). After the fourth layer of coating and sintering, most pores were found to be smaller than 450 nm. This suggests that only particles or agglomerates under 450 nm can effectively fill these pores. However, the inks used in this work have not been fully optimized, with agglomerate sizes ranging between 450 nm and 700 nm. Given that the influence of oxygen content was addressed in previous research, it can be inferred that this multilayer sintering approach is applicable to various inks and sintering techniques. Further refinement of ink properties, such as reducing agglomerate sizes, holds the potential for further decreasing film porosity.

In this work, the sintered copper thin films have attained an average electrical conductivity of 2.9×10^7 S/m, which is 50 % of the conductivity of bulk copper, with an average porosity of 3.7 %.

6.5 Summary

Copper nanoparticles are emerging as a promising alternative to silver and gold nanoparticles in the field of printed electronics. The primary obstacles in fabricating highly conductive copper films lie in managing the oxide content and porosity of the sintered films. Our prior research demonstrated that impurities such as copper oxides in copper films can be effectively removed by sintering in a reducing gas atmosphere at 300 °C. Given that pore formation in sintered copper films is unavoidable, a multilayer sintering method, involving up to four cycles of repeated coating and sintering, was developed for this work to mitigate film porosity and reduce resistivity. Three different viscosities of 25 wt. % copper inks were produced and utilized to fabricate thin copper films via spin coating. This approach facilitated the preparation of copper films with single-layer thicknesses varying from 100 nm to 700 nm. The results indicated that adjusting the sintering time or increasing the thickness of a single layer could only marginally reduce film porosity and electrical resistivity. Significantly, copper films that underwent four-layer coating and sintering demonstrated a marked decrease in porosity to 3.7 %, in contrast to an average porosity of 33.6 % observed in single-layer sintered films. The reduction in porosity of the sintered copper films was found to align closely with the decrease in their electrical resistivity, confirming the effectiveness of the multilayer sintering method in addressing issues related to porosity. Following the four-layer sintering process, the films attained an electrical resistivity of $3.49 \pm 0.35\,\mu\Omega \cdot \text{cm}$, which is double that of bulk copper, while the single-layer sintered films exhibited a resistivity of $11.17 \pm 2.17\,\mu\Omega \cdot \text{cm}$.

7 Synthesis of TiN/CrN nanocomposite coatings by NP injection

Nanocomposite coatings are highly valued for their potential to combine diverse materials' performance features, offering advanced properties that surpass those of conventional coatings. While CrN and TiN are highly desirable for hard coatings, conventional physical vapor deposition (PVD) processes cannot create a nc-TiN/nc-CrN nanocomposite structure using Cr and Ti as target materials, because Ti and Cr are transition metals with a strong affinity for nitrogen. Instead, these processes yield a single-phase Cr-Ti-N solid solution. To overcome the limitations of material combinations, this chapter introduces a hybrid process for synthesizing nanostructured thin films. Specifically, artificial nc-TiN/nc-CrN nanocomposites were deposited using a hybrid process where TiN nanoparticles and CrN films were synthesized separately but deposited simultaneously during the composite growth. Chapter 4 already discusses the synthesis of TiN nanoparticles using an optimized arc discharge reactor. This section details the technique for combining an arc reactor with a magnetron sputter device. Various aerodynamic lens systems (ALS), essential for in-situ injection of TiN nanoparticles into the vacuum PVD (Physical Vapor Deposition) process, were designed and evaluated through numerical simulations. This work detailed the microstructure and defect evolution in nc-TiN/nc-CrN nanocomposite coatings. Finally, insights into how to further control the nanoparticle properties (such as size and shape) were provided in order to obtain thin films with desired structural properties. Some of the research discussed in this chapter has been published in peer-reviewed journals [190, 191, 193, 192].

7.1 Experimental details

Figure **7-1** illustrates the overall setup for synthesizing TiN/CrN nanocomposite coatings, which comprises three main components: an arc discharge reactor for nanoparticle production, an aerodynamic lens system for particle injection, and a physical vapor deposition (PVD) device for thin film production. Details on arc discharge synthesis are provided in Chapter 4 (Section 4.2). This section delves into the experimental design and construction of aerodynamic lens systems. This section also illustrates how to conduct Computational Fluid Dynamics (CFD) simulations for the designed ALS systems to better understand par-

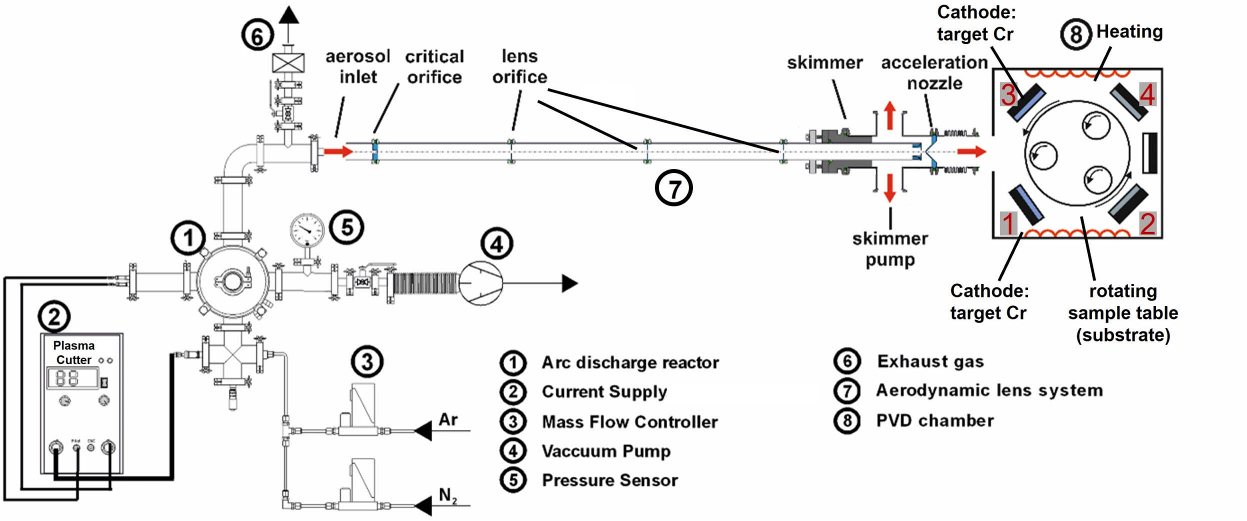

Figure **7-1**: Detailed overview of the experimental setup, including the arc discharge reactor, aerodynamic lens system, and physical vapor deposition (PVD) chamber. Reproduced from Tillmann et al. [190], with permission from Thin Solid Films (Copyright 2019).

ticle transfer behavior. Furthermore, it presents an analysis of the microstructure of the synthesized nanocomposite thin films.

As this work is part of a collaborative project with the Institute of Materials Engineering at TU Dortmund, this section does not focus on the synthesis of thin-film coatings using magnetron sputtering PVD. Detailed experimental methodologies are available in the published literature [189, 191, 190, 192]. Characterization methods for determining the tribological and mechanical properties of the synthesized thin films are not covered in this section; further details are available in the published works.

7.1.1 Design and construction of aerodynamic lens systems

The purpose of the aerodynamic lens system (ALS) used in this work is to focus nanoparticles into a collimated beam for introduction into the PVD process, while allowing the major working gas to be redirected to the side and pumped away. The ALS #1, developed by Kiesler et al. [85], was utilized for this work. The designs of the other two lens systems, ALS #2 and ALS #3, are based on the Aerodynamic Lens Calculator, a design and evaluation tool developed by Wang and McMurry [201, 202] and were modified from the previous study by Kiesler et al. [85].

Figure **7-2** presents a schematic of the particle-beam forming apparatus, including an inlet

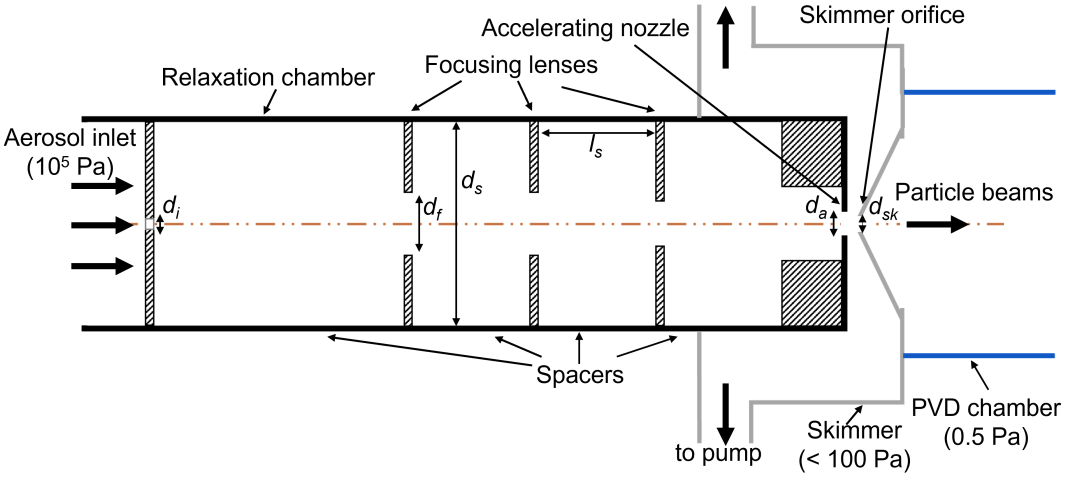

Figure **7-2**: Schematic representation of the aerodynamic lens system used for forming particle beams, which is connected with a physical vapor deposition (PVD) chamber.

Table **7-1**: Geometric specifications of the aerodynamic lens systems used to link the nanoparticle synthesis reactor with the physic vapor deposition (PVD) chamber.

Aerodynamic Lens System (ALS)		**ALS #1**	**ALS #2**	**ALS #3**
Focused particles	d_{TiN} [nm]	30-70	8-20	5-12
Lens Stage number	n	3	3	2
Inlet orifice	d_{i} [mm]	0.3	0.15	0.15
Lens orifice	d_{f} [mm]	6.0; 6.0; 6.0	3.5; 3.5; 3.5	3.0; 4.0
Spacer diameter	d_{s} [mm]	25	25	25
Spacer length	l_{s} [mm]	240; 240; 240; 240	240; 70; 70; 70	240; 85; 85
Accelerating nozzle	d_{a} [mm]	6.0	3.5	4.0
Skimmer orifice	d_{sk} [mm]	0.8	1.0	0.8

Table **7-2**: Boundary conditions applied in Computational Fluid Dynamics (CFD) simulations.

Aerodynamic Lens System (ALS)	**ALS #1**	**ALS #2**	**ALS #3**
Carrier gas	Nitrogen	Nitrogen	Nitrogen
Inlet mass flow rate [a]	0.71 slm	0.16 slm	0.16 slm
Operating temperature	300 K	300 K	300 K
Pressure before inlet nozzle	101325 Pa	101325 Pa	101325 Pa
Pressure after inlet nozzle [a]	475.8 Pa	341.3 Pa	293.8
Pressure at the skimmer pump [b]	88.4 Pa	22.7 Pa	72.2 Pa
Pressure at PVD coating chamber [b]	0.5 Pa	0.5 Pa	0.5 Pa

[a] *Calculated by Aerodynamic Lens Calculator;* [b] *Obtained in the experiment*

orifice, a series of focusing lenses, and an accelerating orifice. The essential geometrical dimensions are summarized in Table **7-1**. The specific configurations of the acceleration nozzles for ALS #2 and ALS #3 are detailed in Appendix B. All orifice designs were created using Computer-Aided Design (CAD) software (SolidWorks, Dassault Systèmes SE, France) and fabricated at the University of Duisburg-Essen. Essentially, the designed ALS is based on the ISO quick flange system, employing stainless steel vacuum tubes (DN25KF) as spacers, which are held together with clamps. The acceleration zone of the lens system is connected to a DN50KF cross, used as a skimmer, with the two perpendicular ports of the skimmer chamber connected to the skimmer pump (Trivac D65B, Oerlikon Leybold Vacuum, Cologne, Germany).

7.1.2 Numerical simulation of particle transfer behavior

Numerical simulations were conducted using CFD Fluent simulation software (Version 6.2, Fluent Inc., Lebanon, NH, USA) to demonstrate the motion of particles within the aerodynamic lens system. The CFD modeling process began with the calculation of the gas flow field. Subsequently, particles were injected into this flow field, and their trajectories were determined. A two-dimensional (axisymmetric) numerical model, replicating the lens geometry, was employed to simulate the compressible, laminar flow of an ideal gas. The boundary conditions applied derive from the experimental operating conditions and the theoretical framework provided by the Aerodynamic Lens Calculator [202], as detailed in Table **7-2**. The gas flow field was determined by numerically solving the continuity, momentum, and energy equations for an ideal gas. Particles were treated as a highly diluted second phase within the perfect gas, rendering particle-particle interactions negligible. Consequently, the presence of particles does not affect the continuous phase (gas phase). The flow field solution thus obtained served as the basis for the subsequent particle trajectory calculations.

Lagrangian particle tracking was employed to predict the trajectories of TiN nanoparticles (ρ_{TiN}= 5200 kg/m^3) with various Stokes diameters. The Stokes diameter d_{S}, which describes the mobility of fractal aggregates, can be estimated using the equation presented by Kiesler et al. [85]:

$$d_{\mathrm{S}} = d_{\mathrm{M}} \cdot k_0 \left(\frac{d_{\mathrm{prim}}}{d_{\mathrm{M}}}\right)^{3-D_{\mathrm{fm}}} \tag{7-1}$$

Where D_{fm} represents the mass fractal dimension, and k_0 is the scaling prefactor. In this work, $D_{\mathrm{fm}} = 2.17$ and $k_0 = 0.97$ [177] were used to estimate the Stokes diameters. For example, the primary diameter estimated by the crystallite size ($d_{\mathrm{prim}} = 9.5\,\mathrm{nm}$) and mobility diameter ($d_{\mathrm{M}} = 348\,\mathrm{nm}$) were determined by X-ray diffraction (XRD) and a Scanning Mobility Particle Sizer (SMPS), respectively. The average Stokes diameter, calculated with the aforementioned equation, is 17 nm [190]. User-Defined Functions (UDFs), developed in a previous study by Kiesler et al. [85], were integrated to account for modifications in the particle drag force due to local gas characteristics such as pressure, mean free path, and relaxation time. Moreover, the impact of Brownian motion on particle movement was considered by applying a randomly distributed external force on the particles [114], calculated using the diffusion coefficient of each particle.

7.1.3 Linking the arc discharge reactor to a magnetron sputter device

For the in-situ injection of TiN nanoparticles into the PVD chamber, connecting both devices is essential. It must be noted that the arc discharge reactor operates at atmospheric pressure (10^5 Pa), whereas the PVD device functions at approximately 0.5 Pa. The TiN nanoparticles (NPs) were synthesized in an arc discharge reactor using a titanium rod (6.4 mm diameter, 99.99 % purity) in a nitrogen/argon gas mixture at a ratio of 4 and an arc current of 20 A. Utilizing the aforementioned aerodynamic lens system, the TiN NPs can be in-situ injected into the PVD chamber and merged with the CrN thin film on the substrate; as illustrated in Figure **7-1**. A distance of 500 mm was maintained between the acceleration nozzle of the aerodynamic lens and the substrate. Before the deposition of the PVD thin film, a baseline test was conducted, where TiN NPs were directly injected into the PVD chamber and deposited onto a Si wafer substrate. The temperatures of the PVD chamber (370 °C and 480 °C) and the bias voltages (-100V, -200V) were varied to examine their effects on the particle distribution on the wafer substrate.

The reference CrN thin film and the nanostructured TiN/CrN thin film were deposited on 100-oriented Si wafers as well as on 1.2343 (AISI H11) steel substrates (diameter 40 mm, thickness 4 mm) using a magnetron sputtering device (CC800/9 Custom, CemeCon AG, Germany). The Institute of Materials Engineering at TU Dortmund conducted all the thin film depositions. A detailed pretreatment of the steel substrates used for this work, including polishing, cleaning, gas ion etching, and metal ion etching, is described in Tillmann et al. [190]. For synthesizing the CrN thin film, two chromium targets (99.95 % purity) mounted on the cathodes surrounding the inlet of the nanoparticle jet (cathodes 1 and 3 in Figure **7-1**) were operated in DC (Direct Current) mode at a power of 4500 W for 8500 seconds using a bias voltage of -100 V. Argon and krypton were used as inert gases, with constant gas flows of 180 sccm (Standard Cubic Centimeters per Minute) and 70 sccm, respectively. A thin film thickness of 3.2 ± 0.2 µm was achieved using the aforementioned PVD deposition parameters. Additionally, a carbon-laminated TEM grid was coated for only 240 seconds to produce a thin film with a thickness of only 80 nm.

7.1.4 Characterization of thin film microstructures

The microstructural evolution of both the reference CrN and the TiN/CrN nanocomposite thin films was examined. For this analysis, a Scanning Electron Microscope (SEM, model JSM-7001F, Jeol, Japan) was used to assess the films' topography and morphology on coated silicon wafer substrates. Further detailed investigations into the morphology and topography of the synthesized thin films were carried out using a Field Emission Transmission Electron Microscope (FE-TEM, model JEM-2200FS, Jeol, Japan), equipped with energy-dispersive X-ray spectroscopy (EDX) at the Interdisciplinary Center for Analytics on the Nanoscale (ICAN) at the University of Duisburg-Essen. For the nanocomposite thin films, cross-sectional lamellae were prepared using a Focused Ion Beam (FIB) technique with the Helios NanoLab 600 (FEI, USA). With support from ICAN, Time-of-Flight Secondary Ion Mass Spectrometry (ToF-SIMS, model 5-100 from IONTOF, Muenster, Germany) was utilized to measure the TiN concentration within the CrN thin film, analyzing its distribution as a function of film depth. Additionally, SEM analysis was conducted to evaluate the particle distribution, systematically examining the samples at intervals of 0.3 mm across the nanoparticle deposit. ImageJ software was then used to quantify the areas covered by nanoparticles.

7.2 Integration of the arc discharge reactor with the PVD chamber

7.2.1 Effect of PVD chamber conditions on the injection of TiN NPs

After integrating the arc discharge reactor with the PVD chamber via ALS #1, the feasibility of injecting TiN nanoparticles directly into the PVD chamber, omitting the CrN thin film deposition, was assessed. Si wafers subjected to a 60-minute deposition were subsequently examined using SEM and XRD to evaluate the impact of chamber pressure, temperature,

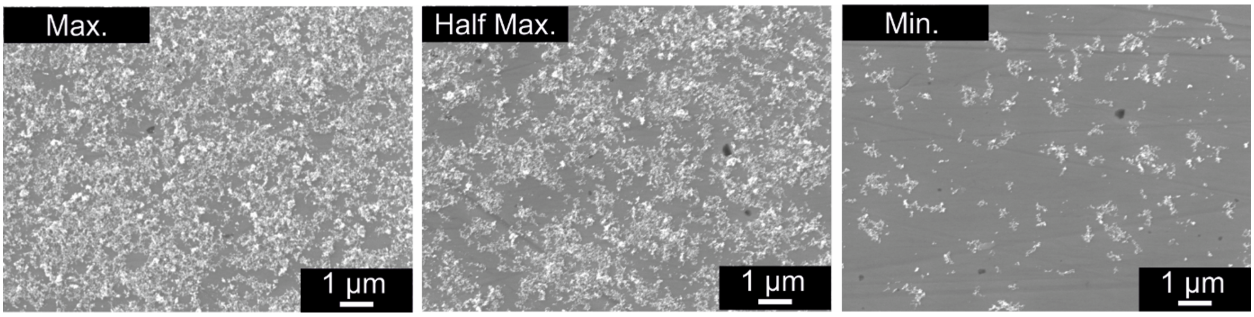

Figure **7-3**: SEM images of the nanoparticle distribution on the substrate at a chamber pressure of 500 mPa. The left images (Max.) display the on-axis location (directly facing the injection axis), while the middle (Half Max.) and right images (Min.) depict the off-axis locations (away from the injection axis). Reproduced from Tillmann et al.[190], with permission from Thin Solid Films (Copyright 2019).

bias voltage, plasma state, and injection distance on the nanoparticles' morphological and structural characteristics. Results indicated that changes in chamber pressure and bias voltage did not affect the TiN nanoparticles' morphology. Notably, an increase in chamber temperature from 25 °C to 480 °C resulted in the partial sintering of the nanoparticles. However, variations in the chamber conditions did not significantly alter the crystallite size of the TiN nanoparticles, which remained consistent at an average of 10.7 ± 1.2 nm across all tested conditions [190].

Figure **7-3** showcases the nanoparticle distribution on the substrate at a chamber pressure of 0.5 Pa, highlighting a gradual decline in coverage from the on-axis location (directly facing the injection axis) to the off-axis locations (away from the injection axis). At a threshold concentration of roughly 5 area-%, it becomes evident that the nanoparticles are not deposited as individual primary particles, but rather as chain-like agglomerates. Analysis of the areas covered by nanoparticles reveals a normal distribution of deposited nanoparticles, as depicted in Figure **7-4**. An increase in chamber temperature or bias voltage leads to more extensive coverage but a reduced peak concentration of nanoparticles. In Figure **7-4** (b), the diminished particle concentration and expanded distribution may result from enhanced Brownian motion at elevated PVD chamber temperatures. Figure **7-4** (c) suggests that nanoparticles exiting the arc reactor may be partially charged. Given plasma's composition of electrons, ions, and neutrals, it is plausible to assume particles produced by arc plasma could acquire both positive and negative charges. This observation underscores the need for additional research to ascertain the charge state of the synthesized nanoparticles and to consider employing a neutralizer or applying a unipolar charger to recondition the particles before their introduction into the PVD chamber.

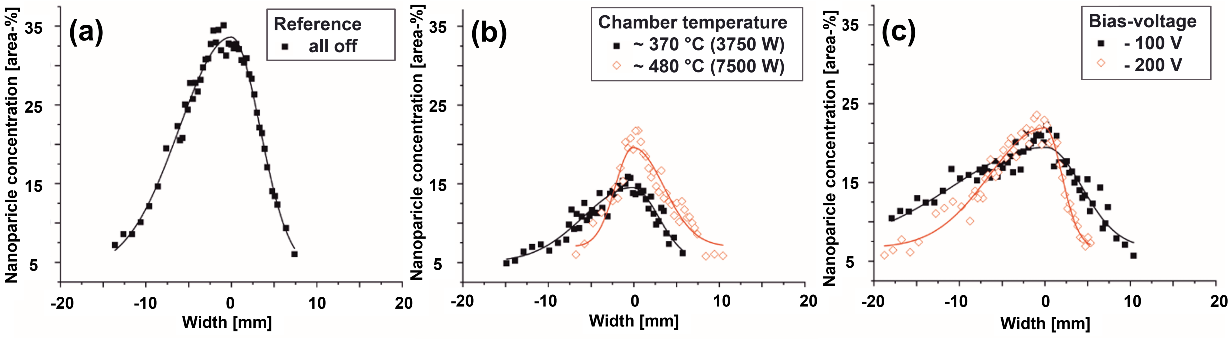

Figure **7-4**: Distribution of TiN nanoparticles on the wafer substrate as influenced by the PVD chamber temperature and substrate bias voltage. Adapted from Tillmann et al. [190], with permission from Thin Solid Films (Copyright 2019).

7.2.2 Transfer efficiency estimation for aerodynamic lens systems

In this work, the size-dependent transmission efficiency of particles through the aerodynamic lens system (ALS) was approximated using CFD calculations. Initially, CFD modeling involves calculating the gas flow field, followed by the injection of particles into this flow and the computation of their trajectories. Figure **7-5** illustrates the predicted contours of absolute pressures and gas velocities within the ALS #1 using nitrogen. Beginning with an external ambient pressure of $p_{\text{Inlet}} = 10^5$ Pa, there was a progressive pressure drop through the aerodynamic lens system to the skimmer, where p_{Skimmer} and p_{Chamber} reached 88 Pa and 0.5 Pa, respectively. These pressures align closely with the theoretical predictions from the Aerodynamic Lens Calculator, with all pressure differences falling within 5 %. Given that the average velocity in a fully developed laminar pipe flow is half the maximum velocity, the gas velocities predicted by Fluent simulations align with those calculated by the Aerodynamic Lens Calculator [202]. Unlike pressure, gas velocity increases at each stage, from $v_1 = 98$ m/s to $v_4 = 174$ m/s, achieving supersonic speeds of 483 m/s in the accelerating nozzle. However, as illustrated in Figure **7-5**, the velocity of the working gas decreases in the PVD chamber relative to the spray distance.

Figure **7-6** illustrates exemplary particle trajectories incorporating Brownian diffusion within the aerodynamic lens system ALS #1, which is tailored for spherical particles with Stokes diameters ranging from 30 to 70 nm ($\rho_{TiN} = 5200$ kg/m^3). The trajectories reveal that nanoparticles 20-70 nm can be focused into narrow beams. Conversely, beams consisting of particles with Stokes diameters of 5 nm and 150 nm experience broadening within the PVD vacuum chamber. To assess the transfer efficiency for particles of various Stokes diameters, 4000 particles were simulated for each size, with the count of particles reaching the PVD chamber outlet being recorded. The transfer efficiency for ALS #1 is depicted in Figure **7-7** (a). Nanoparticles with Stokes diameters of 15-70 nm achieve transfer efficiencies above

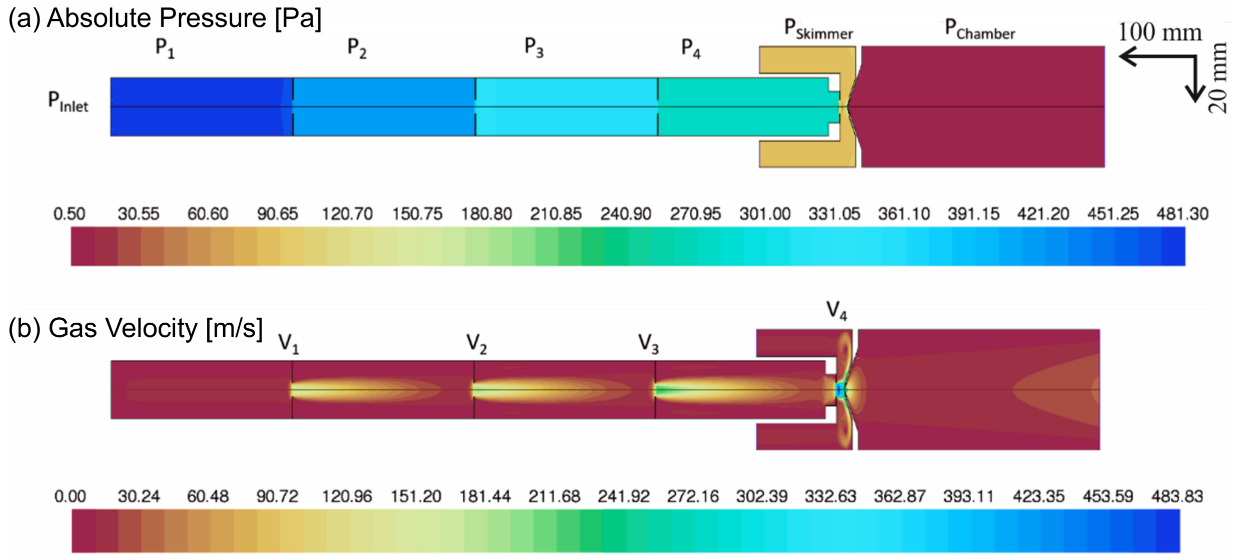

Figure **7-5**: Contour predictions of absolute pressures (Pa) and gas velocities (m/s) within the aerodynamic lens system ALS #1, derived from axisymmetric CFD simulations. Adapted from Tillmann et al. [190], with permission from Thin Solid Films (Copyright 2019).

98.7 %, respectively, when passing through the ALS #1. This indicates that approximately 1.3 % of the particles introduced into the system are retained within the lens assembly. Conversely, the lowest transfer efficiency observed is 11.5 % for particles possessing a diameter of 150 nm. It is noteworthy that the CFD model employed in this work omits the inlet orifice to streamline the computational effort. However, a notable loss of particles at the inlet orifice was observed. It is recommended to enhance the analysis of particle transfer efficiency through the ALS by modeling the inlet orifice and the ALS separately, subsequently integrating their transfer functions for an in-depth evaluation.

Building on ALS #1, two additional aerodynamic lens systems were developed to enhance the transfer of nanoparticles smaller than 15 nm into the PVD chamber: ALS #2 targets particles ranging from 8-20 nm, and ALS #3 is designed for 5-12 nm particles. Table **7-2** provides a detailed comparison of geometric specifications between these new models and the original ALS #1. Notably, the overall length of the lens systems has been reduced to minimize particle loss due to the Brownian motion of smaller particles. Appendix C showcases the predicted contours of absolute pressures and gas velocities, along with exemplary particle trajectories for ALS #2 and ALS #3. CFD simulations were conducted to ascertain the transfer efficiency of these newly developed lens systems, with results presented in Figure **7-7** (b) and **7-7** (c). The lowest transfer efficiency observed for particles ranging from 5-15 nm is 30 % using ALS #1, 80 % with ALS #2, and exceeds 95 % with ALS #3. However, ALS #2 and ALS #3 also exhibit a relatively high transfer efficiency (around 50 %) for particles larger

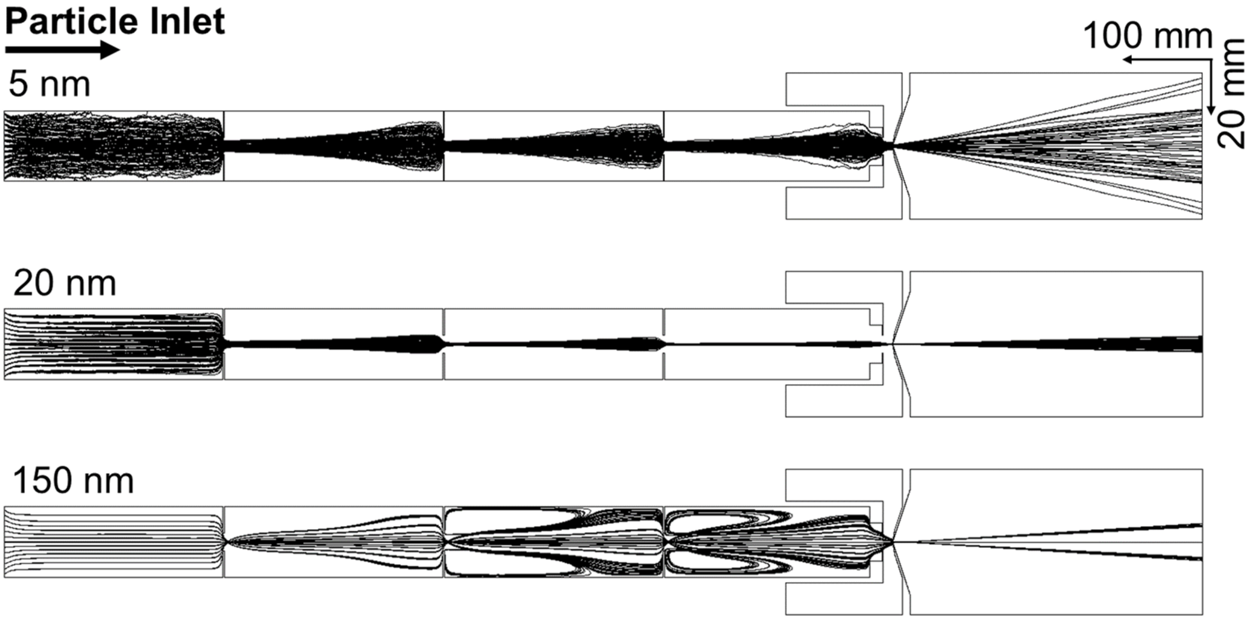

Figure **7-6**: Numerical calculations depict the particle trajectories within the aerodynamic lens system ALS #1, moving from left to right. The visualization is radially expanded by a factor of 3. Adapted from Tillmann et al. [190], with permission from Thin Solid Films (Copyright 2019).

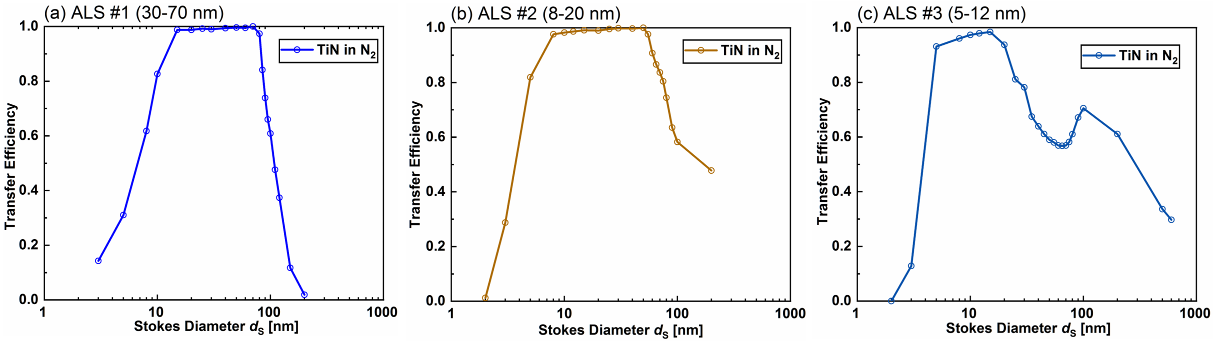

Figure **7-7**: Overview of the transmission efficiency of TiN nanoparticles based on their Stokes diameter through the three aerodynamic lens systems (ALS) utilized in this work, with nitrogen serving as the working gas in the computational fluid dynamics (CFD) simulations than 100 nm, potentially introducing undesirably large particles into the PVD chamber. This discrepancy primarily stems from the limitations of the Aerodynamic Lens Calculator that was used to design the ALS. This Aerodynamic Lens Calculator inadequately predicts the focusing/defocusing effects of the accelerating nozzle and overlooks the Brownian motion of nanoparticles [202]. Consequently, there is a need for further optimization of the ALS designs, particularly regarding the accelerating nozzles, to improve the precision of the ALS transfer functions.

7.3 Structure properties of the TiN/CrN nanocomposite films

7.3.1 Microstructure evolution with embedded nanoparticles

In this section, nanoparticle (NP) injection utilized the ALS #1, which is designed to classify and focus TiN NPs within the 30-70 nm range. The initial characterization of the synthesized nanocomposite coatings, which achieved a film thickness of 3.2 µm after an 8500 s deposition, was conducted using XRD. However, the XRD analysis did not reveal distinct TiN patterns due to the minimal amount of TiN NPs embedded in the CrN thin film. Consequently, to facilitate better detection, a thinner TiN/CrN film was produced by depositing it onto a TEM-Grid for 240 s, resulting in a film approximately 80 nm thick. This deposited thin film on TEM-Grid was characterized by Grazing Incidence XRD (GIXRD) analysis. The analysis confirmed a two-phase structure of CrN and TiN within the novel nanostructured thin films, demonstrating the successful incorporation of TiN NPs [193].

Figure **7-8** presents STEM images of the TiN/CrN nanostructured thin film deposited on a TEM-Grid. Figure **7-8** (a) reveals that the film comprises a sputtered CrN matrix with embedded TiN nanoparticles (NPs), which are introduced not as isolated particles but as chain-like agglomerates. These agglomerates form prior to their introduction into the PVD chamber, a process detailed in section 7.2, and not through interactions within the thin film matrix. The effective integration of TiN NPs into the CrN matrix is further detailed in the micrographs of the CrN and TiN interface and the elemental mapping for Cr, Ti, and N shown in Figures **7-8** (b) and **7-8** (c), respectively. Notably, areas with TiN NPs exhibit a higher nitrogen content, suggesting the formation of a CrN thin film layer around the NPs, potentially creating a core-shell structure. The interface between the CrN thin film and the TiN NPs was examined using HRTEM, as displayed in Figure **7-9**. Comparing the interfaces among CrN crystallites in the reference CrN PVD thin films with those between CrN and TiN crystallites in the nanocomposite coatings reveals no significant increase in defects or porosity. This observation supports the conclusion that the hybrid deposition process does not introduce notable defects at the lateral interfaces between the TiN and CrN crystallites.

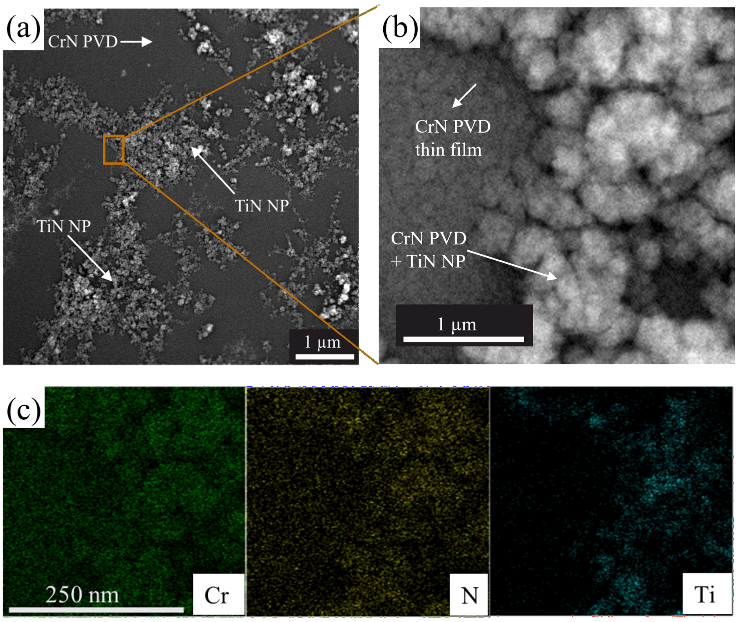

Figure **7-8**: STEM images showcasing (a) an overview of the TiN/CrN thin film deposited on the TEM-Grid, (b) a detailed micrograph of the interface between CrN thin film and TiN nanoparticles, and (c) the corresponding elemental mapping. Adapted from Tillmann et al. [193], with permission from Applied Surface Science (Copyright 2021).

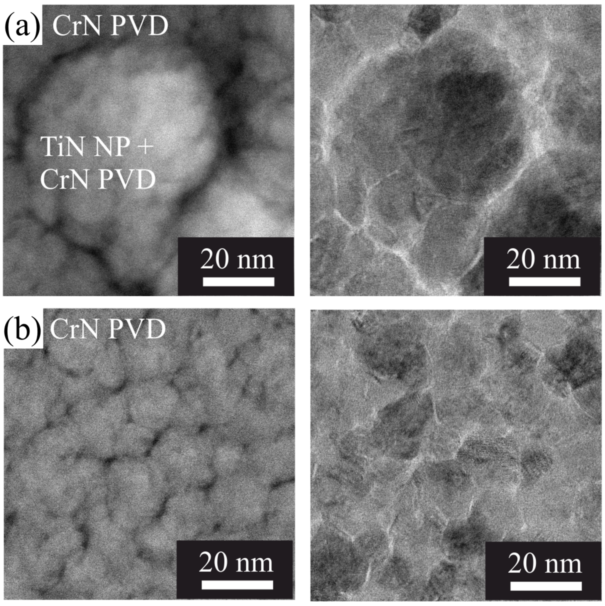

Figure **7-9**: STEM images displaying the TiN/CrN thin film on the TEM-Grid, featuring dark and bright field micrographs at positions (a) with TiN nanoparticles and (b) lacking TiN nanoparticles. Adapted from Tillmann et al. [193], with permission from Applied Surface Science (Copyright 2021).

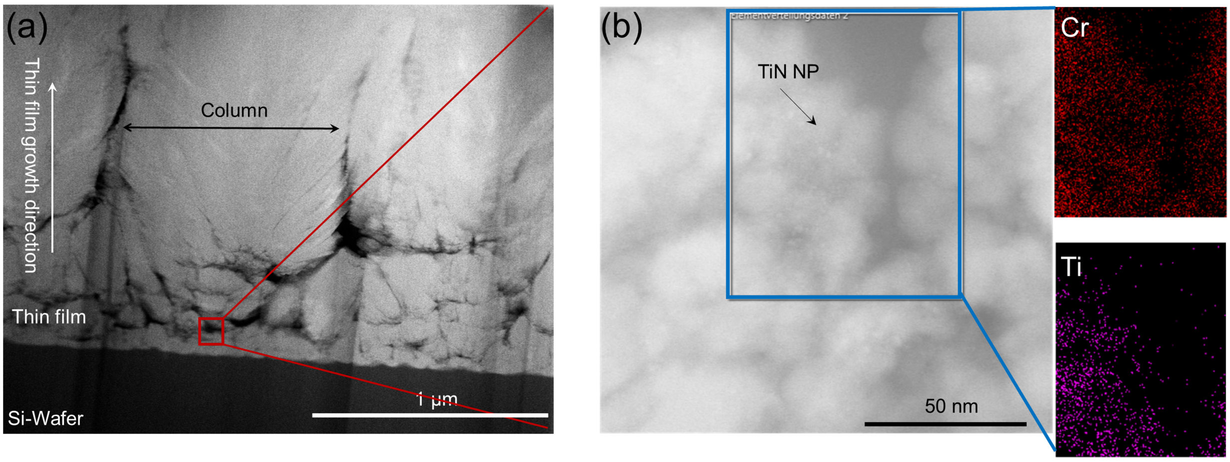

Figure **7-10**: (a) FIB cross-sectional images of the TiN/CrN nanocomposite thin film on a Si wafer substrate and (b) STEM image with the corresponding elemental mapping illustrating the distribution of embedded TiN nanoparticles. Adapted from Tillmann et al. [192], with permission from Surface & Coatings Technology (Copyright 2021).

To examine the microstructure along the vertical direction (corresponding to the direction of thin film growth), a FIB cross-sectional lamella was prepared from a TiN/CrN thin film deposited on a wafer, achieving a thickness of 3.2 µm after an 8500 s deposition period. Figure **7-10** showcases the FIB cross-section of the TiN/CrN thin film on the Si wafer. EDX mapping, illustrated in Figure **7-10** (b), confirms the presence of titanium, indicating the successful incorporation of nanoparticles into the PVD film. However, the growth direction reveals noticeable pores near the TiN nanoparticles, suggesting that the introduction of external nanoparticles disrupts the columnar growth of the CrN film. The observed disruptions in the columnar structure could be attributed to the size of the agglomerates injected (focused within the 30-70 nm range by ALS #1), which surpasses the average crystallite size of CrN (approximately 10 nm). The incorporation of larger TiN particles compared to CrN crystallites enhances the surface roughness of the substrate, leading to a rougher microstructure characterized by disrupted columnar growth and increased porosity within the thin film.

7.3.2 Effect of particle content and size on thin film microstructure

The influence of varying injected particle content was explored by adjusting the rotation rate of the thin film substrate and the power of the Cr cathode within the PVD chamber [192]. Due to the limitations in the sensitivity of current measurement instruments, the precise particle content in the thin film remains difficult to quantify. Nonetheless, EDX mapping for all synthesized TiN/CrN nanocomposite coatings showed that the titanium

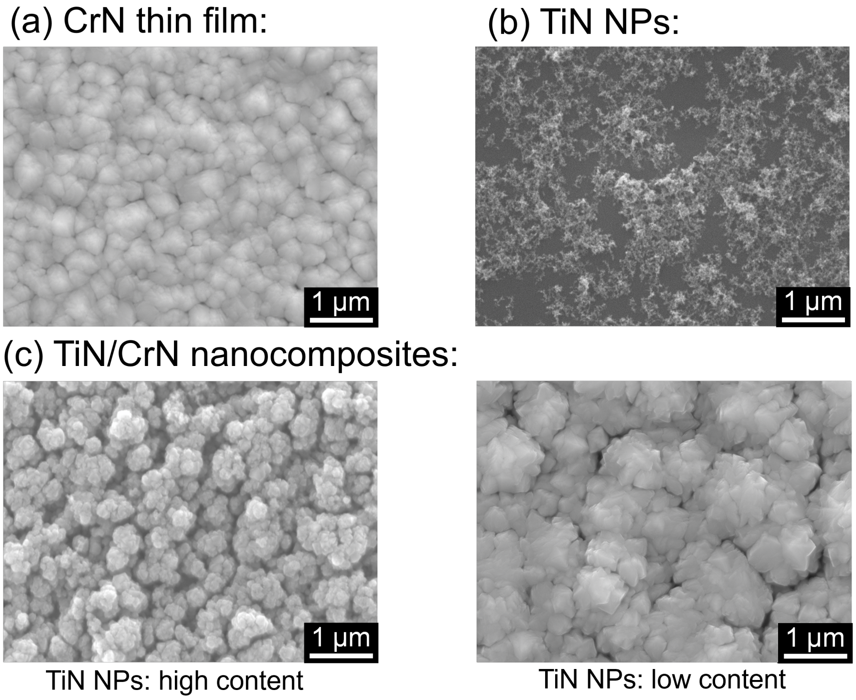

Figure **7-11**: SEM images illustrating the microstructures of (a) a reference CrN thin film, (b) reference as-sprayed TiN nanoparticles, and (c) TiN/CrN nanocomposites featuring varying concentrations of embedded TiN nanoparticles.

element content is less than 1 at. %. Figure **7-11** (c) displays the topology of TiN/CrN thin films with two different concentrations of embedded nanoparticles, alongside Figure **7-11** (a) and **7-11** (b) which present the SEM images of the reference CrN thin film and as-sprayed TiN, respectively. In comparison to the CrN thin film, the surface of the TiN/CrN thin films exhibits a more heterogeneous topography, characterized by a cauliflower-like structure interspersed with pores. This rougher surface texture is attributed to the aggregation of TiN nanoparticles, leading to irregular columnar growth as evidenced by FIB cross-sectional STEM images.

The collaborative research effort focused on the effect of bias voltage on the incorporation of TiN nanoparticles into CrN thin films. Adjusting the bias voltage and employing various power supply modes—direct-current (DC), medium-frequency (MF), and high-power impulse magnetron sputtering (HiPIMS)—enabled an increase in nanoparticle content within the thin films, while keeping the titanium content below 1 at. % [191]. Notably, an increase in nanoparticle content correlated with a decrease in the CrN thin film's crystallite size from 9.4 ± 2.3 nm to 5.5 ± 1.4 nm. This work demonstrated that introducing TiN nanoparticles into the growing CrN film led to a core-shell structure, with the partial coverage of CrN crystallites by TiN nanoparticles disrupting CrN grain growth. This disruption necessitated the renucleation of newly arriving CrN-forming species. With higher TiN content, the growth of CrN is increasingly interrupted, requiring frequent renucleation and resulting in smaller CrN crystallites at elevated TiN nanoparticle concentrations. Theoretically, such smaller grain sizes are expected to restrict dislocation activities, thereby enhancing hardness [154]. Under mechanical stress, these materials are predisposed to grain-boundary sliding, a more energy-intensive process than deformation through dislocation movement, which would lead to increased hardness. However, this work found that the hardness of the synthesized TiN/CrN nanocomposite coatings was lower compared to the reference CrN thin film, likely due to growth defects in the columnar structure, specifically intercolumnar porosity.

To selectively introduce nanoparticles of specific sizes into CrN thin films, nanocomposite coatings were produced employing ALS #2 and ALS #3 for particle transmission. Figure **7-12** displays the topography and morphology of nanocomposite coatings fabricated using all three lens assemblies. The reference CrN thin film exhibits a characteristic dense columnar structure. However, coatings derived using ALS #1 (targeting 30-70 nm NPs) and ALS #2 (focusing on 8-20 nm NPs) show a coarser structure with noticeable disruptions in growth. In comparison, the use of ALS #3 (aimed at 5-12 nm NPs) resulted in a finer structure, closely resembling the CrN reference (left). Coarser layer structures are only observed locally, suggesting the injection of predominantly smaller agglomerates into the process. The variation in film structures with ALS #3 might reflect the combined effects of nanoparticle concentration and the size of the embedded agglomerates. EDX analysis revealed nanoparticle contents of 0.53 ± 0.03 % for ALS #2 and 0.02 ± 0.01 % for ALS #3 within the nanocomposite coatings. Given the limited injection of smaller particles using ALS #3, produced by the arc plasma reactor, it remains unclear which factor—particle concentration or agglomerate size-predominantly influences the coarser film structure.

7.4 Technical challenges in aerodynamic lens systems

The nanoparticle distribution within the CrN layer, varying by depth, was examined through Time-of-Flight Secondary Ion Mass Spectrometry (TOF-SIMS), as illustrated in Figure **7-13** (a). Minimal Ti signals were detected at locations with the least particle concentration (off-axis from the injection orifice), with signal intensity increasing towards areas of maximum particle concentration (on-axis of the injection orifice). Nonetheless, the Ti intensity fluctuates across the depth of the thin film, revealing a non-uniform injection of particles along the vertical film depth (direction of columnar growth) and a diminishing TiN deposition rate as the film thickness increases. Figure **7-13** (b) presents a 3D visualization of the TiN nanoparticle distribution throughout the entire film thickness at the point of highest nanoparticle concentration, showcasing the uneven vertical integration of nanoparticles. The left images (Max.) display the on-axis location (directly facing the injection axis), while the middle (Half Max.) and right images (Min.) depict the off-axis locations (away from the

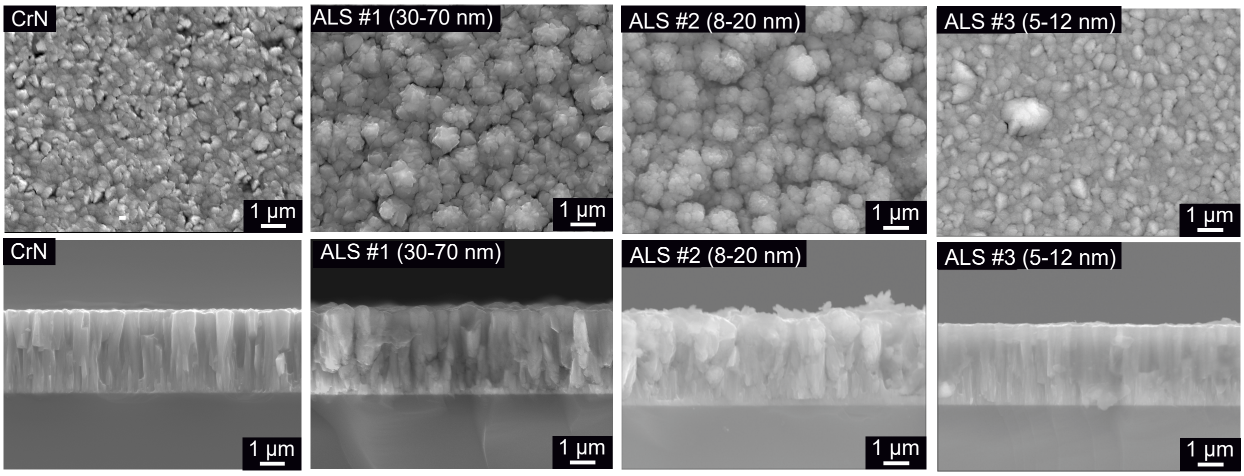

Figure **7-12**: SEM images present a detailed comparison of the surface topography and cross-section morphology between reference CrN PVD thin film and TiN/CrN nanocomposite films. These nanocomposite films were deposited using various aerodynamic lens systems (ALS), showcasing the incorporation of TiN particles with varied sizes into the CrN matrix.

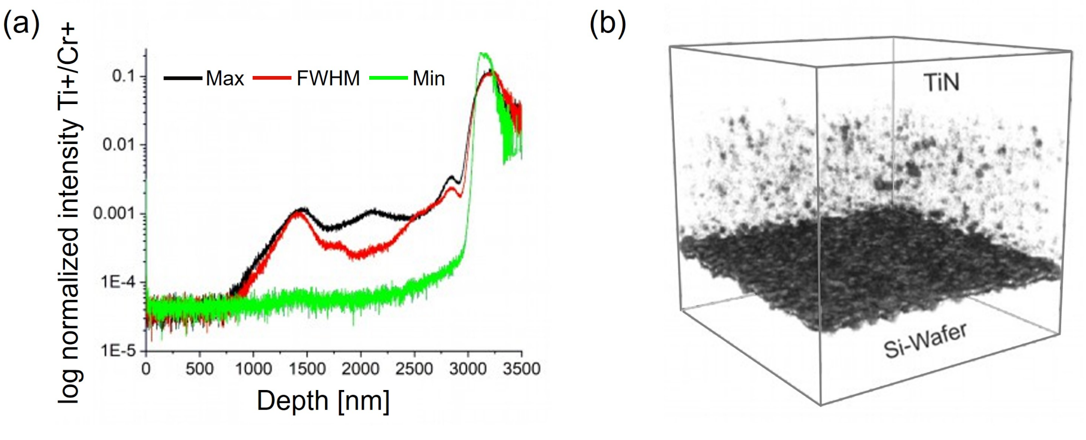

Figure **7-13**: TOF-SIMS analysis of the TiN/CrN thin film shows (a) depth profiles indicating areas of maximum (the on-axis location, directly facing the injection axis), FWHM and minimum particle incorporation areas (off-axis location, away from the injection axis) and (b) a 3D visualization of the TiN distribution.

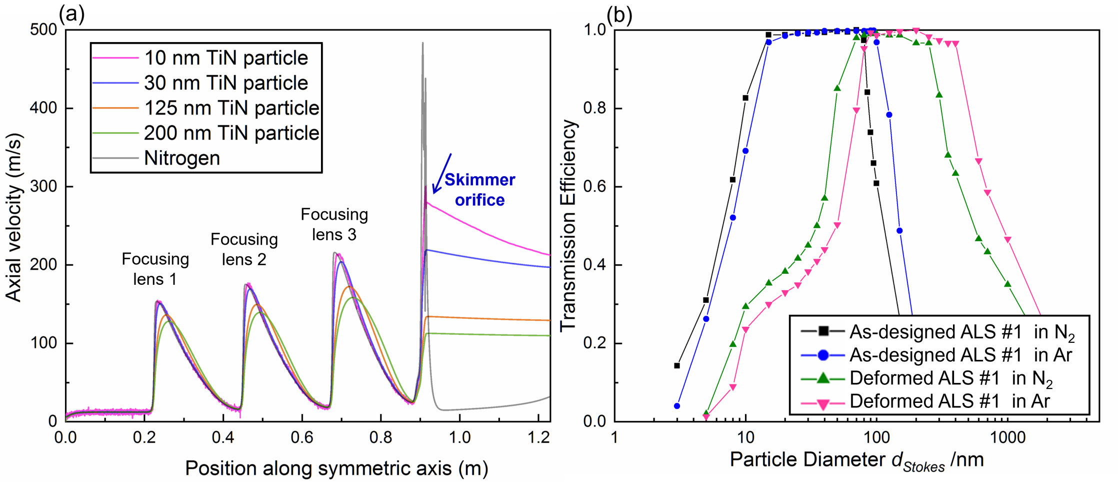

Figure **7-14**: (a) Particle velocity calculations within the aerodynamic lens system ALS #1; (b) Comparative analysis of particle transmission efficiency pre- and post-deformation of critical orifices (inlet and skimmer), based on numerical calculations from a CFD model.

injection axis) The observed gradual reduction in nanoparticle injection during the film's growth process is likely due to the clogging of the orifices (specifically, the inlet and skimmer orifices) within the aerodynamic lens system (ALS). For ALS #1, the inlet and skimmer orifices measure 0.3 mm and 0.8 mm in diameter, respectively. Clogging at the inlet orifice may result from the high particle concentration produced by the arc discharge reactor, while skimmer orifice clogging is likely caused by the densification of particle beams. The small dimensions of these orifices are crucial for efficiently shaping and transporting a particle beam across a significant pressure drop (from 10^5 Pa to 0.5 Pa in this work). An increase in the size of the inlet orifice would lead to a higher gas mass flow rate. Research by Kiesler et al. [85] showed that raising the mass flow rate from 0.1 slm to 4.5 slm increases the required length of the ALS from 0.16 m to over 7.31 m. Additionally, the necessary pumping speed rises quadratically with the mass flow rate, from 1.25 m^3/h to 2553.7 m^3/h for the specified rate increase. To mitigate the clogging issue, it is advisable to dilute the aerosol particle concentration prior to its introduction into the ALS and to employ a system of parallel-arranged multiple lenses to maintain the intended quantity of nanoparticle injection.

When utilizing aerodynamic lens systems (ALS), it is crucial to periodically verify the actual diameters of the lens orifices, particularly the inlet and skimmer orifices, which are typically less than 1.0 mm. Manufacturing these small nozzles often involves tolerances that could impact the actual gas mass flow rates. Additionally, the aerosol inlet and skimmer orifices function as critical nozzles where gas velocity reaches supersonic speeds, leading to high particle velocities. For instance, Figure **7-14** (a) illustrates the numerically calculated particle velocity in ALS #1 with nitrogen as the carrier gas, showing that TiN nanoparticles

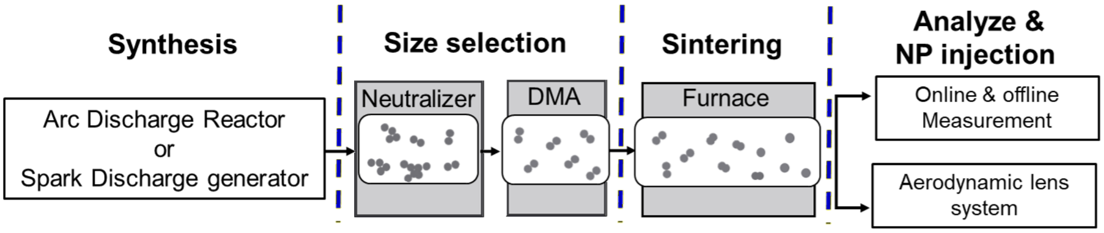

Figure **7-15**: A schematic for manipulating nanoparticle size and shape by selecting specific sizes and densifying agglomerates.

of 10 nm can reach velocities up to 300 m/s at the skimmer orifice. Over time, these critical orifices may become deformed due to the high-speed impact of nanoparticles, resulting in an enlarged orifice diameter. In this work, such deformation was noted in ALS #1, where the inlet orifice expanded from 0.3 mm to 0.56 mm, and the skimmer orifice from 0.8 mm to 1.0 mm. A revised CFD model, incorporating these deformed orifice geometries, was developed to assess the particle transfer efficiency of the altered ALS #1, as shown in Figure **7-14** (b). The findings indicate that the modified ALS #1 is no longer capable of effectively transferring nanoparticles within the intended size range of 30-70 nm. Instead, it now efficiently channels particles ranging from 100-300 nm into the PVD chamber. For subsequent research on aerodynamic lens systems, incorporating robust materials to construct essential orifices may improve their durability and extend their service life.

7.5 Discussion and suggestion for future work

This research has shown that integrating an atmospheric arc reactor with an industrial magnetron sputtering system enables the deposition of nanocomposite coatings from materials typically considered soluble in each other. The size, structure, and quantity of embedded nanoparticles, along with the bias voltage used in the coating process, play crucial roles in defining the topology and morphology of the resultant layers. Nevertheless, the overlapping of various effects, such as the structure and size of the agglomerates and the content of nanoparticles, has constrained the exploration of specific mechanisms in depth. Further investigation is required to understand the impact of the nanoparticles' shape, primary size, and quantity on the evolution of the microstructure. Figure **7-15** outlines a strategy for controlling nanoparticle size and shape through size selection and densification of agglomerates. Specifically, given that nanoparticles produced in the arc discharge reactor may exhibit fractal shapes, the desired particle sizes are initially selected using a Differential Mobility Analyzer (DMA) and subsequently sintered in a high-temperature tube furnace.

To mitigate potential grain growth during the sintering process, TiN nanoparticles could be synthesized using a spark discharge generator (SDG), which typically yields significantly

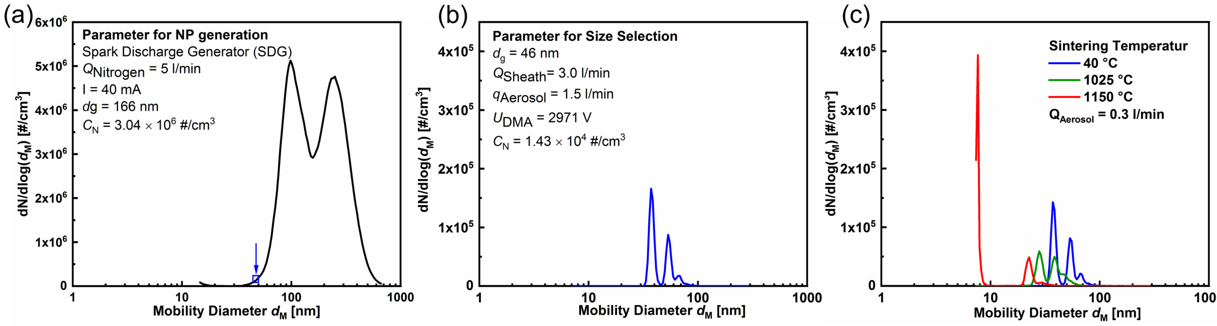

Figure **7-16**: Preliminary studies demonstrating the practicality of the above suggestion. This includes (a) the synthesis of TiN nanoparticles using a spark discharge generator, (b) classifying agglomerates of the targeted size (50 nm), and (c) observing size changes following aerosol sintering at various temperatures.

smaller primary nanoparticles (of several nanometers in size). Figure **7-16** presents preliminary research that demonstrates the viability of this approach. As depicted in Figure **7-16** (a), the SDG produced nanoparticle agglomerates, exhibiting a broad size range. Based on XRD analysis, the synthesized NPs consist of Ti and TiN components. Subsequently, agglomerates around 50 nm in size were selectively filtered in real-time via a DMA and directed through a tube furnace at a flow rate of 0.3 L/min (Figure **7-16** (b)). This process effectively densified most particles to under 10 nm through online sintering at a temperature of 1150 °C (Figure **7-16** (c)). Future studies will aim to closely examine the rate of densification and alterations in particle morphology and size as influenced by variations in sintering temperature and the duration of particle exposure within the tube furnace.

7.6 Summary

To enable unrestricted material combinations, this chapter introduces a novel approach in which produced nanoparticles and magnetron-sputtered thin films are deposited simultaneously on a substrate. Specifically, TiN nanoparticles were fabricated in an arc discharge reactor and independently yet simultaneously incorporated into a growing CrN PVD thin film. For the in-situ injection of TiN nanoparticles into a PVD chamber, a custom-tailored aerodynamic lens system was employed to connect the atmospheric pressure arc discharge reactor to a high vacuum magnetron sputtering device.

This study first examined how the condition of the PVD chamber, including pressure, temperature, bias voltage, and plasma state, influenced particle deposition. The TiN nanoparticles were effectively deposited on the substrates, forming a normal distribution, and injecting into the PVD chamber as chain-like agglomerates rather than isolated primary particles. The research showed that modifying the bias voltage and using different power supply methods—DC, MF, and HiPIMS—significantly affects the rate at which nanoparticles are deposited onto the wafer substrate, indicating the charged nature of nanoparticles produced from the arc reactor.

Further analysis of the microstructural development of both the reference CrN and the TiN/CrN nanocomposite thin films confirmed a two-phase structure, evidencing the successful integration of TiN nanoparticles. High-resolution transmission electron microscopy (HRTEM) examination of the interface between CrN thin films and TiN nanoparticles showed that the hybrid deposition process did not introduce significant defects at the lateral interfaces. Introducing TiN nanoparticles into the CrN film resulted in a core-shell structure that inhibited the re-nucleation of CrN precursors, thereby reducing the average size of CrN grains. This reduction in grain size and increased grain boundaries highlight the potential for creating nanocomposite thin films with improved mechanical properties, such as enhanced hardness and wear resistance.

Cross-sectional microstructure analysis of the thin films revealed pores near the TiN nanoparticles, indicating that introducing external nanoparticles disrupts the CrN film's columnar growth (along the vertical direction). The disruption is attributed to the injection of larger agglomerates, which increases substrate surface roughness and leads to a microstructure characterized by disrupted columnar growth and higher porosity. These growth defects reduce the hardness of the TiN/CrN nanocomposite coatings compared to the reference CrN thin film.

The study also explored how the content and size of particles and agglomerates incorporated into the CrN thin film affect the microstructure of the nanocomposite coatings. An increase in TiN nanoparticle content was associated with a reduction in CrN crystallite size. However, films with higher nanoparticle concentrations exhibited coarser topography and greater porosity. Using a specific aerodynamic lens aimed at injecting smaller particles (5-12 nm TiN nanoparticles) resulted in a finer structure similar to the reference CrN film. The exact influence of particle concentration or agglomerate size on the coarser film structure remains to be determined, necessitating further research to understand how the shape, size, and quantity of injected TiN nanoparticles affect the microstructure of nanocomposite thin films. Insights into technical challenges and research suggestions for future work are also provided, based on the results already available.

8 Conclusions

Arc discharge synthesis holds industrial relevance for its cost-effectiveness and scalability. Utilizing various gas compositions such as oxygen, nitrogen, and argon, the arc discharge process enables the production of a wide array of nanoparticles with high purity and yield, including metals, metal oxides, metal nitrides, and carbides. This dissertation provides an in-depth study of the production of metallic (copper, Cu) and ceramic (titanium nitride, TiN) nanoparticles using an optimized arc discharge reactor, with a focus on how different processing parameters affect the properties of the nanoparticles. Moreover, the study investigates the potential applications of these nanoparticles, notably the utilization of Cu nanoparticles in the development of conductive films and TiN nanoparticles in the fabrication of protective coatings.

Copper nanoparticles (Cu NPs) present a viable alternative to silver and gold nanoparticles for use in conductive inks due to their comparable electrical conductivity and significantly lower cost. The production of Cu NPs using an optimized arc discharge reactor was closely investigated to achieve an optimal balance between yield and particle size. The synthesis process consistently produced Cu NPs at rates ranging from 1.2 to 5.5 g/h, with both the production rate and the average size of the primary particles being influenced by key production parameters, including the applied current and the flow of the carrier gas. The Cu NPs generated exhibited a surface oxide layer thickness of 2 nm, similar to those obtained via wet-chemical synthesis methods. For the purposes of this work, copper nanoparticles with a primary particle size of less than 60 nm were selected to ensure an adequate mass for their subsequent use in conductive ink applications, aligning with the practical needs for effective utilization.

The suitability of arc-synthesized copper nanoparticles (Cu NPs) for printed electronics was evaluated through the use of a ball milling technique to prepare copper conductive inks. A thorough investigation into how ball milling parameters influence dispersion stability and particle morphology of the prepared inks was conducted. Inks formulated with a lower energy input (30 Hz for 50 minutes using 1.5 ml of zirconia grinding beads) demonstrated enhanced dispersion stability, a result of the diminished agglomerate size. These inks were subsequently utilized for the fabrication of thin films through spin coating. The strategic addition of formic acid as a reducing agent effectively interacted with the surface oxide of the copper nanoparticles, promoting the development of a continuous metallic structure within the sintered film. When sintered in a diluted reducing gas environment, the copper films exhibited significantly low electrical resistivity, measured at $5.4 \pm 0.6\,\mu\Omega \cdot \mathrm{cm}$, which is three times that of bulk copper. This result underscores their potential as cost-effective alternatives to commercial silver or gold inks.

The challenge in fabricating highly conductive copper films lies in managing oxide content and porosity. By sintering in a reducing atmosphere at 300 °C, copper oxide impurities within the films can be effectively eliminated. A novel multilayer sintering technique, incorporating up to four cycles of coating and sintering, was devised to lower film porosity and decrease resistivity. Three different copper inks were produced to fabricate films with single-layer thicknesses varying from 100 nm to 700 nm. Although minor adjustments in sintering duration or an increase in layer thickness slightly decreased the porosity, it was the application of a four-layer coating and sintering process that significantly reduced porosity to 3.7 %, a significant reduction from the 33.6 % typical of single-layer sintered films. This reduction in porosity is directly correlated with a notable decrease in electrical resistivity, highlighting the effectiveness of the multilayer sintering strategy. After completing the four-layer sintering, the copper films achieved an electrical resistivity of $3.49 \pm 0.35\,\mu\Omega \cdot \mathrm{cm}$, substantially lower than the $11.17 \pm 2.17\,\mu\Omega \cdot \mathrm{cm}$ observed in single-layer films.

In synthesizing titanium nitride nanoparticles (TiN NPs), the study investigated the effect of synthesis parameters, such as quench gas velocity, composition, and arc current on the particle quality, yield, and size. Findings revealed that using higher quench gas velocities led to the formation of nanoparticles with primary sizes ranging from 10-15 nm, whereas lower velocities produced larger particles, ranging from 20-50 nm. The stoichiometry of TiN NPs was maintained across varying nitrogen compositions in the quench gas, but an increase in nitrogen levels led to a noticeable growth in crystallite sizes, approximately 20 nm. Adjusting the quench gas composition and increasing the arc current significantly influenced the production rate and yield. Specifically, a nitrogen increase from 20 % to 100 % tripled the production rate, and a rise in arc current from 12 A to 50 A enhanced yield tenfold. Additionally, the study presented a mechanism for deposit formation on the cathode tip, enhancing the comprehensive understanding of the synthesis process and facilitating the optimization of its long-term stability.

The optimized parameters for synthesizing titanium nitride (TiN) nanoparticles were utilized to create nanostructured thin films. To address the challenge of limited material combinations and prevent the formation of a single-phase solid solution, a novel hybrid process was developed for depositing artificial TiN/Chromium Nitride (CrN) nanocomposites. This method involved the separate synthesis and simultaneous deposition of TiN nanoparticles and CrN thin films during the growth of the composite. First, the study investigated how various conditions within the Physical Vapor Deposition (PVD) chamber, such as pressure, temperature, bias voltage, and plasma state, affected nanoparticle deposition. It was found that TiN nanoparticles were successfully deposited onto the substrates in a normal distribution, entering the PVD chamber as chain-like agglomerates rather than isolated primary particles. Microstructural analysis of both the reference CrN and the TiN/CrN nanocomposite thin films revealed a two-phase structure, evidencing the successful incorporation of TiN nanoparticles. Examination of the interface between CrN thin films and TiN nanoparticles revealed that the hybrid deposition method did not cause significant defects along the lateral interfaces. However, cross-sectional analysis of the thin films showed the presence of pores adjacent to the TiN nanoparticles, suggesting that the addition of external nanoparticles interferes with the columnar growth pattern (along the vertical direction) of the CrN thin film. These growth irregularities result in a reduction of the hardness in the TiN/CrN nanocomposite coatings when contrasted with the reference CrN thin film.

This study also investigated the impact of incorporating varying contents and sizes of particles into CrN/TiN thin films on their microstructural evolution. It was found that increasing the amount of TiN nanoparticles resulted in a reduction of CrN crystallite sizes, subsequently increasing the number of grain boundaries. This indicates the potential for synthesizing thin films with enhanced mechanical properties. Nonetheless, films with a higher nanoparticle concentration exhibited rougher textures, increased porosity, and thus decreased mechanical properties. Utilizing an aerodynamic lens system to introduce smaller particles (5-12 nm TiN NPs) led to a finer and less porous structure, comparable to the standard CrN film. Nevertheless, the precise mechanisms by which nanoparticle concentration or agglomerate size affects the film structure remain unclear, emphasizing the urgent need for more in-depth research. Such studies would unravel the specific influence of the shape, size, and overall amount of TiN nanoparticles on the microstructural characteristics of nanocomposite thin films. Furthermore, this research outlines the technical challenges encountered with the use of an aerodynamic lens system and leverages the insights obtained from these initial findings to recommend avenues for subsequent investigations.

Bibliography

[1] Abhinav K, V., Rao R, V. K., Karthik, P. S., and Singh, S. P. Copper conductive inks: synthesis and utilization in flexible electronics. *RSC Advances 5*, 79 (2015), 63985–64030.

[2] Alivisatos, A. P. Semiconductor Clusters, Nanocrystals, and Quantum Dots. *Science 271*, 5251 (1996), 933–937.

[3] Allaire, F., and Dallaire, S. Synthesis and characterization of silicon nitride powders produced in a d.c. thermal plasma reactor. *Journal of Materials Science 26*, 24 (1991), 6736–6740.

[4] Arora, N., and Sharma, N. Arc discharge synthesis of carbon nanotubes: Comprehensive review. *Diamond and Related Materials 50* (2014), 135–150.

[5] Athanassiou, E. K., Grass, R. N., and Stark, W. J. Chemical Aerosol Engineering as a Novel Tool for Material Science: From Oxides to Salt and Metal Nanoparticles. *Aerosol Science and Technology 44*, 2 (2010), 161–172.

[6] Banerjee, S., and Tyagi, A. K., Eds. *Functional materials: preparation, processing and applications*, 1st ed ed. Elsevier insights. Elsevier, London ; Waltham, MA, 2012. OCLC: ocn662400135.

[7] Baron, P. A., Kulkarni, P., and Willeke, K., Eds. *Aerosol measurement: principles, techniques, and applications*, 3rd ed. Wiley, Hoboken, N.J, 2011.

[8] Barshilia, H., Deepthi, B., and Rajam, K. Transition Metal Nitride–Based Nanolayered Multilayer Coatings and Nanocomposite Coatings as Novel Superhard. 2010, pp. 427–480.

[9] Ben Aissa, M. A., Tremblay, B., Andrieux-Ledier, A., Maisonhaute, E., Raouafi, N., and Courty, A. Copper nanoparticles of well-controlled size and shape: a new advance in synthesis and self-organization. *Nanoscale 7*, 7 (2015), 3189–3195.

[10] Bica, I. Plasma device for magnetic nanoparticles production. *Journal of Magnetism and Magnetic Materials 201*, 1-3 (1999), 45–48.

[11] Borysiuk, J., Grabias, A., Szczytko, J., Bystrzejewski, M., Twardowski, A., and Lange, H. Structure and magnetic properties of carbon encapsulated Fe nanoparticles obtained by arc plasma and combustion synthesis. *Carbon 46*, 13 (2008), 1693–1701.

[12] Boulos, M. I., Fauchais, P., and Pfender, E. Basic Concepts of Plasma Generation. In *Handbook of Thermal Plasmas.* Springer International Publishing, Cham, 2016, pp. 1–34.

[13] Bredas, J.-L., Marder, S. R., and Reichmanis, E. Preface to the *Chemistry of Materials* Special Issue on -Functional Materials. *Chemistry of Materials 23*, 3 (2011), 309–309.

[14] Brunauer, S., Emmett, P. H., and Teller, E. Adsorption of Gases in Multimolecular Layers. *Journal of the American Chemical Society 60*, 2 (1938), 309–319.

[15] Buesser, B., and Pratsinis, S. E. Design of Nanomaterial Synthesis by Aerosol Processes. *Annual Review of Chemical and Biomolecular Engineering 3*, 1 (2012), 103–127.

[16] Bystrzejewski, M., Cudziło, S., Huczko, A., Lange, H., Soucy, G., Cota-Sanchez, G., and Kaszuwara, W. Carbon encapsulated magnetic nanoparticles for biomedical applications: Thermal stability studies. *Biomolecular Engineering 24*, 5 (2007), 555–558.

[17] Camargo, P. H. C., Satyanarayana, K. G., and Wypych, F. Nanocomposites: synthesis, structure, properties and new application opportunities. *Materials Research 12*, 1 (2009), 1–39.

[18] Chan, H.-J., Huang, B.-C., Wang, L.-W., Liao, K.-H., and Lo, C.-Y. Porosity reduction in inkjet-printed copper film by progressive sintering on nanoparticles. *Thin Solid Films 627* (2017), 33–38.

[19] Chang, H., Lenggoro, I. W., Okuyama, K., and Kim, T.-O. Continuous Single-Step Fabrication of Nonaggregated, Size-Controlled and Cubic Nanocrystalline Y_2O_3: Eu^{3+} Phosphors Using Flame Spray Pyrolysis. *Japanese Journal of Applied Physics 43*, 6R (2004), 3535.

[20] Chang, Y., Young, R. M., and Pfender, E. Thermochemistry of thermal plasma chemical reactions. Part II. A survey of synthesis routes for silicon nitride production. *Plasma Chemistry and Plasma Processing 7*, 3 (1987), 299–316.

[21] Chen, J., Lu, G., Zhu, L., and Flagan, R. C. A simple and versatile mini-arc plasma source for nanocrystal synthesis. *Journal of Nanoparticle Research 9*, 2 (2007), 203–213.

[22] Chen, S., Luo, D., and Zhao, G. Investigation of the Properties of $Ti_xCr_{1-x}N$ Coatings Prepared by Cathodic Arc Deposition. *Physics Procedia 50* (2013), 163–168.

[23] Choi, S., Lee, H., and Park, D.-W. Synthesis of Silicon Nanoparticles and Nanowires by a Nontransferred Arc Plasma System. *Journal of Nanomaterials 2016* (2016), 1–9.

[24] Choi, S., Lee, M.-S., and Park, D.-W. Photocatalytic performance of TiO_2/V_2O_5 nanocomposite powder prepared by DC arc plasma. *Current Applied Physics 14*, 3 (2014), 433–438.

[25] Choi, S., Matsuo, J., and Watanabe, T. Synthesis of AlB_{12} and YB_{66} Nanoparticles by RF Thermal Plasmas. *Journal of Physics: Conference Series 441* (2013), 012030.

[26] Chung, D. D. L. *Functional materials: electrical, dielectric, electromagnetic, optical and magnetic applications: (with companion solution manual).* No. v. 2 in Engineering materials for technological needs. World Scientific, Singapore ; Hackensack, NJ, 2010. OCLC: ocn401147113.

[27] Chung, W.-Y., Lai, Y.-C., Yonezawa, T., and Liao, Y.-C. Sintering Copper Nanoparticles with Photonic Additive for Printed Conductive Patterns by Intense Pulsed Light. *Nanomaterials 9*, 8 (2019), 1071.

[28] Cunha, M. D., Sargsyan, M. A., Kh Gadzhiev, M., Tereshonok, D. V., and Benilov, M. S. Numerical and experimental investigation of thermal regimes of thermionic cathodes of arc plasma torches. *Journal of Physics D: Applied Physics 56*, 39 (2023), 395204.

[29] Dai, L., Xue, Y., Qu, L., Choi, H.-J., and Baek, J.-B. Metal-Free Catalysts for Oxygen Reduction Reaction. *Chemical Reviews 115*, 11 (2015), 4823–4892.

[30] Dekker, J. P., Van Der Put, P. J., Veringa, H. J., and Schoonman, J. Vapour-phase synthesis of titanium nitride powder. *Journal of Materials Chemistry 4*, 5 (1994), 689.

[31] Deng, D., Cheng, Y., Jin, Y., Qi, T., and Xiao, F. Antioxidative effect of lactic acid-stabilized copper nanoparticles prepared in aqueous solution. *Journal of Materials Chemistry 22*, 45 (2012), 23989.

[32] Dixkens, J., and Fissan, H. Development of an Electrostatic Precipitator for Off-Line Particle Analysis. *Aerosol Science and Technology 30*, 5 (1999), 438–453.

[33] Dong, S., Chen, X., Gu, L., Zhang, L., Zhou, X., Liu, Z., Han, P., Xu, H., Yao, J., Zhang, X., Li, L., Shang, C., and Cui, G. A biocompatible titanium ni-

tride nanorods derived nanostructured electrode for biosensing and bioelectrochemical energy conversion. *Biosensors and Bioelectronics 26*, 10 (2011), 4088–4094.

[34] Epp, J. X-ray diffraction (XRD) techniques for materials characterization. In *Materials Characterization Using Nondestructive Evaluation (NDE) Methods*. Elsevier, 2016, pp. 81–124.

[35] Fang, F., Kennedy, J., Manikandan, E., Futter, J., and Markwitz, A. Morphology and characterization of TiO_2 nanoparticles synthesized by arc discharge. *Chemical Physics Letters 521* (2012), 86–90.

[36] Fauchais, P., and Vardelle, A. Pending problems in thermal plasmas and actual development. *Plasma Physics and Controlled Fusion 42*, 12B (2000), B365–B383.

[37] Fedlheim, D. L., and Foss, C. A. *Metal Nanoparticles*, 1st ed. CRC Press, 2001.

[38] Flack, W. W., Soong, D. S., Bell, A. T., and Hess, D. W. A mathematical model for spin coating of polymer resists. *Journal of Applied Physics 56*, 4 (1984), 1199–1206.

[39] Flagan, R. C. On Differential Mobility Analyzer Resolution. *Aerosol Science and Technology 30*, 6 (1999), 556–570.

[40] Friedlander, S. K. *Smoke, dust, and haze: fundamentals of aerosol dynamics*, 2nd ed. Topics in chemical engineering. Oxford University Press, New York, 2000.

[41] Fu, Q., Kokalj, D., Stangier, D., Kruis, F. E., and Tillmann, W. Aerosol synthesis of titanium nitride nanoparticles by direct current arc discharge method. *Advanced Powder Technology 31*, 9 (2020), 4119–4128.

[42] Fu, Q., Li, W., and Kruis, F. E. Highly conductive copper films prepared by multilayer sintering of nanoparticles synthesized via arc discharge. *Nanotechnology 34*, 22 (2023), 225601.

[43] Fu, Q., Stein, M., Li, W., Zheng, J., and Kruis, F. E. Conductive films prepared from inks based on copper nanoparticles synthesized by transferred arc discharge. *Nanotechnology 31*, 2 (2020), 025302.

[44] Gao, W., Wang, Y., Wang, Q., Sun, Z., Guo, J., and Chen, P. Revisiting group 4–7 transition metals for heterogeneous ammonia synthesis. *EES Catalysis 2*, 3 (2024), 780–788.

[45] Georgakilas, V., Perman, J. A., Tucek, J., and Zboril, R. Broad Family of Carbon Nanoallotropes: Classification, Chemistry, and Applications of Fullerenes, Carbon Dots, Nanotubes, Graphene, Nanodiamonds, and Combined Superstructures. *Chemical Reviews 115*, 11 (2015), 4744–4822.

[46] Gertsman, V., Valiev, R., Akhmadeev, N., and Mishin, O. Deformation Behaviour of Ultrafine-Grained Materials. *Materials Science Forum 225-227* (1996), 739–744.

[47] Girshick, S. L., Heberlein, J. V. R., McMurry, P. H., Gerberich, W. W., Iordanoglou, D. I., Rao, N. P., Gidwani, A., Tymiak, N., Fonzo, F. D., Fan, M. H., and Neumann, D. Hypersonic plasma particle deposition of nanocrystalline coatings. In *Innovative Processing of Films and Nanocrystalline Powders*. Imperial College Press and World Scientific Publishing Co., 2002, pp. 165–191.

[48] Goesmann, H., and Feldmann, C. Nanoparticulate Functional Materials. *Angewandte Chemie International Edition 49*, 8 (2010), 1362–1395.

[49] Gokhale, P., Mitra, D., Sowade, E., Mitra, K. Y., Gomes, H. L., Ramon, E., Al-Hamry, A., Kanoun, O., and Baumann, R. R. Controlling the crack formation in inkjet-printed silver nanoparticle thin-films for high resolution patterning using intense pulsed light treatment. *Nanotechnology 28*, 49 (2017), 495301.

[50] Goyal, A., Bansal, S., Samuel, P., Kumar, V., and Singhal, S. $CoMn_{0.2}Fe_{1.8}O_4$ ferrite nanoparticles engineered by sol–gel technology: an expert and versatile catalyst for the reduction of nitroaromatic compounds. *J. Mater. Chem. A 2*, 44 (2014), 18848–18860.

[51] Grammatikopoulos, P., Steinhauer, S., Vernieres, J., Singh, V., and Sowwan, M. Nanoparticle design by gas-phase synthesis. *Advances in Physics: X 1*, 1 (2016), 81–100.

[52] Grillo, A. V., Moura, F. J., Solorzano, G. I., Brocchi, E. A., and Mendoza Oliveros, M. E. Vapour phase synthesis and characterization of tin nanoparticles. *Chemical Engineering Transactions 57* (2017), 1399–1404.

[53] Grouchko, M., Kamyshny, A., and Magdassi, S. Formation of air-stable copper–silver core–shell nanoparticles for inkjet printing. *Journal of Materials Chemistry 19*, 19 (2009), 3057.

[54] Guler, U., Shalaev, V. M., and Boltasseva, A. Nanoparticle plasmonics: going practical with transition metal nitrides. *Materials Today 18*, 4 (2015), 227–237.

[55] Guler, U., Suslov, S., Kildishev, A. V., Boltasseva, A., and Shalaev, V. M. Colloidal Plasmonic Titanium Nitride Nanoparticles: Properties and Applications. *Nanophotonics 4*, 3 (2015), 269–276.

[56] Gurav, A., Kodas, T., Pluym, T., and Xiong, Y. Aerosol Processing of Materials. *Aerosol Science and Technology 19*, 4 (1993), 411–452.

[57] Hafiz, J., Mukherjee, R., Wang, X., McMurry, P., Heberlein, J., and Girshick, S. Hypersonic Plasma Particle Deposition—A Hybrid between Plasma Spraying and Vapor Deposition. *Journal of Thermal Spray Technology 15*, 4 (2006), 822–826.

[58] Hahn, H., and Averback, R. S. The production of nanocrystalline powders by magnetron sputtering. *Journal of Applied Physics 67*, 2 (1990), 1113–1115.

[59] Hall, D. B., Underhill, P., and Torkelson, J. M. Spin coating of thin and ultrathin polymer films. *Polymer Engineering & Science 38*, 12 (1998), 2039–2045.

[60] Han, J. G., Myung, H. S., Lee, H. M., and Shaginyan, L. R. Microstructure and mechanical properties of Ti–Ag–N and Ti–Cr–N superhard nanostructured coatings. *Surface and Coatings Technology 174-175* (2003), 738–743.

[61] Helsper, C., Mölter, W., and Haller, P. Representative dilution of aerosols by a factor of 10,000. *Journal of Aerosol Science 21* (1990), S637–S640.

[62] Hinds, W. C. *Aerosol technology: properties, behavior, and measurement of airborne particles*, 2nd ed. Wiley, New York, 1999.

[63] Hoebing, T., Hermanns, P., Bergner, A., Ruhrmann, C., Traxler, H., Wesemann, I., Knabl, W., Mentel, J., and Awakowicz, P. Investigation of the flickering of La_2O_3 and ThO_2 doped tungsten cathodes. *Journal of Applied Physics 118*, 2 (2015), 023306.

[64] Huang, Q., and Zhu, Y. Printing Conductive Nanomaterials for Flexible and Stretchable Electronics: A Review of Materials, Processes, and Applications. *Advanced Materials Technologies 4*, 5 (2019), 1800546.

[65] Huang, Y., Gu, Y., Zheng, M., Xu, Z., Zeng, W., and Liu, Y. Synthesis of nanocrystalline titanium nitride by reacting titanium dioxide with sodium amide. *Materials Letters 61*, 4-5 (2007), 1056–1059.

[66] Huttel, Y., Martínez, L., Mayoral, A., and Fernández, I. Gas-phase synthesis of nanoparticles: present status and perspectives. *MRS Communications 8*, 3 (2018), 947–954.

[67] Iijima, S. Helical microtubules of graphitic carbon. *Nature 354*, 6348 (1991), 56–58.

[68] Jang, Y.-R., Joo, S.-J., Chu, J.-H., Uhm, H.-J., Park, J.-W., Ryu, C.-H., Yu, M.-H., and Kim, H.-S. A Review on Intense Pulsed Light Sintering Technologies for Conductive Electrodes in Printed Electronics. *International Journal of Precision Engineering and Manufacturing-Green Technology 8*, 1 (2021), 327–363.

[69] Jeong, S., Lee, S. H., Jo, Y., Lee, S. S., Seo, Y.-H., Ahn, B. W., Kim, G., Jang, G.-E., Park, J.-U., Ryu, B.-H., and Choi, Y. Air-stable, surface-oxide free Cu nanoparticles for highly conductive Cu ink and their application to printed graphene transistors. *Journal of Materials Chemistry C 1*, 15 (2013), 2704.

[70] Jeong, S., Woo, K., Kim, D., Lim, S., Kim, J. S., Shin, H., Xia, Y., and Moon, J. Controlling the Thickness of the Surface Oxide Layer on Cu Nanoparticles for the Fabrication of Conductive Structures by Ink-Jet Printing. *Advanced Functional Materials 18*, 5 (2008), 679–686.

[71] Jiang, W., Fu, Q., Wei, H., and Yao, A. TiN nanoparticles: synthesis and application as near-infrared photothermal agents for cancer therapy. *Journal of Materials Science 54*, 7 (2019), 5743–5756.

[72] Jiang, W., and Kobayashi, A. Research of TiN Coatings by Means of Gas Tunnel Type Plasma Reactive Spraying. In *Novel Materials Processing by Advanced Electromagnetic Energy Sources*. Elsevier, 2005, pp. 427–432.

[73] Joo, S.-J., Hwang, H.-J., and Kim, H.-S. Highly conductive copper nano/microparticles ink via flash light sintering for printed electronics. *Nanotechnology 25*, 26 (2014), 265601.

[74] Joo, S.-J., Park, S.-H., Moon, C.-J., and Kim, H.-S. A Highly Reliable Copper Nanowire/Nanoparticle Ink Pattern with High Conductivity on Flexible Substrate Prepared via a Flash Light-Sintering Technique. *ACS Applied Materials & Interfaces 7*, 10 (2015), 5674–5684.

[75] Joseph, G., and Kundig, K. J. A. *Copper: its trade, manufacture, use, and environmental status*. ASM International, Materials Park, Ohio, 1999.

[76] Järvinen, A., Aitomaa, M., Rostedt, A., Keskinen, J., and Yli-Ojanperä, J. Calibration of the new electrical low pressure impactor (ELPI+). *Journal of Aerosol Science 69* (2014), 150–159.

[77] Kakati, M., Bora, B., Sarma, S., Saikia, B., Shripathi, T., Deshpande, U., Dubey, A., Ghosh, G., and Das, A. Synthesis of titanium oxide and titanium nitride nano-particles with narrow size distribution by supersonic thermal plasma expansion. *Vacuum 82*, 8 (2008), 833–841.

[78] Kamyshny, A., and Magdassi, S. Conductive Nanomaterials for Printed Electronics. *Small 10*, 17 (2014), 3515–3535.

[79] Kang, H., Sowade, E., and Baumann, R. R. Direct Intense Pulsed Light Sintering of Inkjet-Printed Copper Oxide Layers within Six Milliseconds. *ACS Applied Materials & Interfaces 6*, 3 (2014), 1682–1687.

[80] Kang, J. S., Kim, H. S., Ryu, J., Thomas Hahn, H., Jang, S., and Joung, J. W. Inkjet printed electronics using copper nanoparticle ink. *Journal of Materials Science: Materials in Electronics 21*, 11 (2010), 1213–1220.

[81] Karthika, S., Radhakrishnan, T. K., and Kalaichelvi, P. A Review of Classical and Nonclassical Nucleation Theories. *Crystal Growth & Design 16*, 11 (2016), 6663–6681.

[82] Kaushik, N., Kaushik, N., Linh, N., Ghimire, B., Pengkit, A., Sornsakdanuphap, J., Lee, S.-J., and Choi, E. Plasma and Nanomaterials: Fabrication and Biomedical Applications. *Nanomaterials 9*, 1 (2019), 98.

[83] Kazani, I., De Mey, G., Hertleer, C., Banaszczyk, J., Schwarz, A., Guxho, G., and Van Langenhove, L. About the collinear four-point probe technique's inability to measure the resistivity of anisotropic electroconductive fabrics. *Textile Research Journal 83*, 15 (2013), 1587–1593.

[84] Kennedy, M. K., Kruis, F. E., Fissan, H., Mehta, B. R., Stappert, S., and Dumpich, G. Tailored nanoparticle films from monosized tin oxide nanocrystals: Particle synthesis, film formation, and size-dependent gas-sensing properties. *Journal of Applied Physics 93*, 1 (2003), 551–560.

[85] Kiesler, D., Bastuck, T., Kennedy, M. K., and Kruis, F. E. Development of a high flow rate aerodynamic lens system for inclusion of nanoparticles into growing PVD films to form nanocomposite thin films. *Aerosol Science and Technology 53*, 6 (2019), 630–646.

[86] Kiesler, D., Bastuck, T., Theissmann, R., and Kruis, F. E. Plasma synthesis of titanium nitride, carbide and carbonitride nanoparticles by means of reactive anodic arc evaporation from solid titanium. *Journal of Nanoparticle Research 17*, 3 (2015), 152.

[87] Kim, D.-W., Kim, T.-H., Park, H.-W., and Park, D.-W. Synthesis of nanocrystalline magnesium nitride (Mg_3N_2) powder using thermal plasma. *Applied Surface Science 257*, 12 (2011), 5375–5379.

[88] Kim, I., and Kim, J. The effect of reduction atmospheres on the sintering behaviors of inkjet-printed Cu interconnectors. *Journal of Applied Physics 108*, 10 (2010), 102807.

[89] Kim, K. S., and Kim, T. H. Nanofabrication by thermal plasma jets: From nanoparticles to low-dimensional nanomaterials. *Journal of Applied Physics 125*, 7 (2019), 070901.

[90] Kim, M., Osone, S., Kim, T., Higashi, H., and Seto, T. Synthesis of Nanoparticles by Laser Ablation: A Review. *KONA Powder and Particle Journal 34*, 0 (2017), 80–90.

[91] Kim, N. R., Lee, Y. J., Lee, C., Koo, J., and Lee, H. M. Surface modification of oleylamine-capped Ag–Cu nanoparticles to fabricate low-temperature-sinterable Ag–Cu nanoink. *Nanotechnology 27*, 34 (2016), 345706.

[92] Kim, S. J., Lee, J., Choi, Y.-H., Yeon, D.-H., and Byun, Y. Effect of copper concentration in printable copper inks on film fabrication. *Thin Solid Films 520*, 7 (2012), 2731–2734.

[93] Kim, T.-H., Choi, S., and Park, D.-W. Effects of NH_3 flow rate on the thermal plasma synthesis of AlN nanoparticles. *Journal of the Korean Physical Society 63*, 10 (2013), 1864–1870.

[94] Kim, T.-H., Ko, E. H., Nam, J., Shim, S. E., and Park, D.-W. Preparation of Hexagonal Boron Nitride Nanoparticles by Non-Transferred Arc Plasma. *Journal of Nanoscience and Nanotechnology 17*, 12 (2017), 9217–9223.

[95] Ko, E. H., Kim, T.-H., Choi, S., and Park, D.-W. Synthesis of Cubic Boron Nitride Nanoparticles from Boron Oxide, Melamine and NH_3 by Non-Transferred Ar–N_2 Thermal Plasma. *Journal of Nanoscience and Nanotechnology 15*, 11 (2015), 8515–8520.

[96] Kodas, T. T., and Hampden-Smith, M. J. *Aerosol processing of materials.* Wiley-VCH, New York, 1999.

[97] Kogure, T. Electron Microscopy. In *Developments in Clay Science*, vol. 5. Elsevier, 2013, pp. 275–317.

[98] Kohli, R. Methods for Monitoring and Measuring Cleanliness of Surfaces. In *Developments in Surface Contamination and Cleaning.* Elsevier, 2012, pp. 107–178.

[99] Kolesnichenko, V. G., Zgalat-Lozinskii, O. B., Varchenko, V. T., Herrmann, M., and Ragulya, A. V. Friction and Wear of TiN–Si_3N_4 Nanocomposites Against ShKh15 Steel. *Powder Metallurgy and Metal Ceramics 53*, 11-12 (2015), 680–687.

[100] Kortshagen, U. R., Sankaran, R. M., Pereira, R. N., Girshick, S. L., Wu, J. J., and Aydil, E. S. Nonthermal Plasma Synthesis of Nanocrystals: Fundamental Principles, Materials, and Applications. *Chemical Reviews 116*, 18 (2016), 11061–11127.

[101] Kringhøj, P., Bøttiger, J., Chevallier, J., Bienk, E., and Rätzke, K. The influence of temperature on the microstructure and mechanical properties of sputtered Cr_2N_x coatings. *Surface and Coatings Technology 149*, 1 (2002), 82–88.

[102] Kroto, H. W., Heath, J. R., O'Brien, S. C., Curl, R. F., and Smalley, R. E. C60: Buckminsterfullerene. *Nature 318*, 6042 (1985), 162–163.

[103] Kruis, F., Fissan, H., and Peled, A. Synthesis of nanoparticles in the gas phase for electronic, optical and magnetic applications—a review. *Journal of Aerosol Science 29*, 5-6 (1998), 511–535.

[104] Kruis, F. E., Kusters, K. A., Pratsinis, S. E., and Scarlett, B. A Simple Model for the Evolution of the Characteristics of Aggregate Particles Undergoing Coagulation and Sintering. *Aerosol Science and Technology 19*, 4 (1993), 514–526.

[105] Krywka, C., Paulus, M., Sternemann, C., Volmer, M., Remhof, A., Nowak, G., Nefedov, A., Pöter, B., Spiegel, M., and Tolan, M. The new diffractometer for surface X-ray diffraction at beamline BL9 of DELTA. *Journal of Synchrotron Radiation 13*, 1 (2006), 8–13.

[106] Kwak, J. H., Chun, S. J., Shon, C.-H., and Jung, S. Back-irradiation photonic sintering for defect-free high-conductivity metal patterns on transparent plastic. *Applied Physics Letters 112*, 15 (2018), 153103.

[107] Lee, D., Yang, S., and Choi, M. Controlled formation of nanoparticles utilizing laser irradiation in a flame and their characteristics. *Applied Physics Letters 79*, 15 (2001), 2459–2461.

[108] Lee, D.-H., and Cho, N.-G. Assessment of surface profile data acquired by a stylus profilometer. *Measurement Science and Technology 23*, 10 (2012), 105601.

[109] Lee, D. J., and Oh, J. H. Shapes and morphologies of inkjet-printed nanosilver dots on glass substrates. *Surface and Interface Analysis 42*, 6-7 (2010), 1261–1265.

[110] Lee, D. J., Park, S. H., Jang, S., Kim, H. S., Oh, J. H., and Song, Y. W. Pulsed light sintering characteristics of inkjet-printed nanosilver films on a polymer substrate. *Journal of Micromechanics and Microengineering 21*, 12 (2011), 125023.

[111] Lee, S. H., Oh, S.-M., and Park, D.-W. Preparation of silver nanopowder by thermal plasma. *Materials Science and Engineering: C 27*, 5-8 (2007), 1286–1290.

[112] Lee, Y., Choi, J.-r., Lee, K. J., Stott, N. E., and Kim, D. Large-scale synthesis of copper nanoparticles by chemically controlled reduction for applications of inkjet-printed electronics. *Nanotechnology 19*, 41 (2008), 415604.

[113] Lee, Y. J., Lee, C., and Lee, H. M. Synthesis of oxide-free aluminum nanoparticles for application to conductive film. *Nanotechnology 29*, 5 (2018), 055602.

[114] Li, A., and Ahmadi, G. Dispersion and Deposition of Spherical Particles from Point Sources in a Turbulent Channel Flow. *Aerosol Science and Technology 16*, 4 (1992), 209–226.

[115] Li, J., Gao, L., Sun, J., Zhang, Q., Guo, J., and Yan, D. Synthesis of nanocrystallin titanium nitride powders by direct nitridation of titanium oxide. *Journal of the American Ceramic Society 84*, 12 (2001), 3045–3047.

[116] Li, J.-G., Ikeda, M., Ye, R., Moriyoshi, Y., and Ishigaki, T. Control of particle size and phase formation of TiO_2 nanoparticles synthesized in RF induction plasma. *Journal of Physics D: Applied Physics 40*, 8 (2007), 2348–2353.

[117] Li, S., Ren, Y., Biswas, P., and Tse, S. D. Flame aerosol synthesis of nanostructured materials and functional devices: Processing, modeling, and diagnostics. *Progress in Energy and Combustion Science 55* (2016), 1–59.

[118] Li, W., Li, W., Wei, J., Tan, J., and Chen, M. Preparation of conductive Cu patterns by directly writing using nano-Cu ink. *Materials Chemistry and Physics 146*, 1-2 (2014), 82–87.

[119] Li, W., Sun, Q., Li, L., Jiu, J., Liu, X.-Y., Kanehara, M., Minari, T., and Suganuma, K. The rise of conductive copper inks: challenges and perspectives. *Applied Materials Today 18* (2020), 100451.

[120] Li, X., Liu, T., Sato, M., and Takahashi, S. Synthesis and characterization of Fe–Ti nanoparticles by nitrogen plasma metal reaction. *Powder Technology 163*, 3 (2006), 183–187.

[121] Lim, J.-W., and Isshiki, M. Electrical resistivity of Cu films deposited by ion beam deposition: Effects of grain size, impurities, and morphological defect. *Journal of Applied Physics 99*, 9 (2006), 094909.

[122] Lin, L., Starostin, S. A., Wang, Q., and Hessel, V. An atmospheric pressure microplasma process for continuous synthesis of titanium nitride nanoparticles. *Chemical Engineering Journal 321* (2017), 447–457.

[123] Liu, P., Ziemann, P. J., Kittelson, D. B., and McMurry, P. H. Generating Particle Beams of Controlled Dimensions and Divergence: I. Theory of Particle Motion in Aerodynamic Lenses and Nozzle Expansions. *Aerosol Science and Technology 22*, 3 (1995), 293–313.

[124] Liu, P., Ziemann, P. J., Kittelson, D. B., and McMurry, P. H. Generating Particle Beams of Controlled Dimensions and Divergence: II. Experimental Evaluation

of Particle Motion in Aerodynamic Lenses and Nozzle Expansions. *Aerosol Science and Technology 22*, 3 (1995), 314–324.

[125] Liu, X., and Dai, L. Carbon-based metal-free catalysts. *Nature Reviews Materials 1*, 11 (2016), 16064.

[126] Luo, G., Du, L., Wang, Y., and Wang, K. Composite Nanoparticles. In *Encyclopedia of Microfluidics and Nanofluidics*, D. Li, Ed. Springer US, Boston, MA, 2014, pp. 1–9.

[127] Mackie, W., and Davis, P. Single-crystal zirconium carbide as a high-temperature thermionic cathode material. *IEEE Transactions on Electron Devices 36*, 1 (1989), 220–224.

[128] Magdassi, S., Grouchko, M., and Kamyshny, A. Copper Nanoparticles for Printed Electronics: Routes Towards Achieving Oxidation Stability. *Materials 3*, 9 (2010), 4626–4638.

[129] Mahoney, W., and Andres, R. Aerosol synthesis of nanoscale clusters using atmospheric arc evaporation. *Materials Science and Engineering: A 204*, 1-2 (1995), 160–164.

[130] Mahoney, W., Kempe, M., and Andres, R. Aerosol Synthesis of Metal and Metal Oxide, Nitride and Carbide Nanoparticles Using an Arc Evaporation Source. *MRS Proceedings 400* (1995), 65.

[131] Mangolini, L., Thimsen, E., and Kortshagen, U. High-Yield Plasma Synthesis of Luminescent Silicon Nanocrystals. *Nano Letters 5*, 4 (2005), 655–659.

[132] Milosevic, O. B., Mancic, L., Rabanal, M. E., Gomez, L. S., and Marinkovic, K. Aerosol route in Processing of Nanostructured Functional Materials. *KONA Powder and Particle Journal 27*, 0 (2009), 84–106.

[133] Mir, S. H., Nagahara, L. A., Thundat, T., Mokarian-Tabari, P., Furukawa, H., and Khosla, A. Review—Organic-Inorganic Hybrid Functional Materials: An Integrated Platform for Applied Technologies. *Journal of The Electrochemical Society 165*, 8 (2018), B3137–B3156.

[134] Munz, R. J., Addona, T., and Da Cruz, A.-C. Application of transferred arcs to the production of nanoparticles. *Pure and Applied Chemistry 71*, 10 (1999), 1889–1897.

[135] Murphy, A. B. Formation of titanium nanoparticles from a titanium tetrachloride plasma. *Journal of Physics D: Applied Physics 37*, 20 (2004), 010.

[136] Murphy, A. B., and Uhrlandt, D. Foundations of High-Pressure Thermal Plasmas. *Plasma Sources Science and Technology 27*, 6 (2018), 063001.

[137] Musil, J. Hard and superhard nanocomposite coatings. *Surface and Coatings Technology 125*, 1-3 (2000), 322–330.

[138] Mäkelä, J. M., Keskinen, H., Forsblom, T., and Keskinen, J. Generation of metal and metal oxide nanoparticles by liquid flame spray process. *Journal of Materials Science 39*, 8 (2004), 2783–2788.

[139] Na, Y.-S., Yoo, H., Kim, T.-H., Choi, J., Lee, W. I., Choi, S., and Park, D.-W. Electrochemical performance of Si-multiwall carbon nanotube nanocomposite anode synthesized by thermal plasma. *Thin Solid Films 587* (2015), 14–19.

[140] Nakamura, K., Kinoshita, A., Watanabe, S., Uemura, N., and Takahashi, K. One-step Synthesis of Magnetic Metal-ceramic Core-shell Nanoparticles by RF Thermal Plasma. *Journal of the Society of Powder Technology, Japan 50*, 7 (2013), 495–501.

[141] Namiki, N., Cho, K., Fraundorf, P., and Biswas, P. Tubular Reactor Synthesis of Doped Nanostructured Titanium Dioxide and Its Enhanced Activation by Coronas and Soft X-rays. *Industrial & Engineering Chemistry Research 44*, 14 (2005), 5213–5220.

[142] Nande, A., Kalyani, N. T., Tiwari, A., and Dhoble, S. Exploring the world of functional materials. In *Functional Materials from Carbon, Inorganic, and Organic Sources*. Elsevier, 2023, pp. 1–19.

[143] Nichols, W. T., Malyavanatham, G., Henneke, D. E., O'Brien, D. T., Becker, M. F., and Keto, J. W. Bimodal Nanoparticle Size Distributions Produced by Laser Ablation of Microparticles in Aerosols. *Journal of Nanoparticle Research 4*, 5 (2002), 423–432.

[144] Novoselov, K. S., Geim, A. K., Morozov, S. V., Jiang, D., Zhang, Y., Dubonos, S. V., Grigorieva, I. V., and Firsov, A. A. Electric Field Effect in Atomically Thin Carbon Films. *Science 306*, 5696 (2004), 666–669.

[145] Oh, J.-H., Kim, M., Lee, Y. H., Hong, S.-H., Kim, T.-H., and Choi, S. Synthesis of Tungsten Carbide Nanomaterials in Triple DC Thermal Plasma Jet System. *Journal of Nanoscience and Nanotechnology 19*, 10 (2019), 6277–6284.

[146] Oh, S.-M., Cappelli, M., and Park, D.-W. Preparation of nano-sized silicon carbide powder using thermal plasma. *Korean Journal of Chemical Engineering 19*, 5 (2002), 903–907.

[147] Oh, S.-M., and Park, D.-W. Preparation of AlN fine powder by thermal plasma processing. *Thin Solid Films 316*, 1-2 (1998), 189–194.

[148] Ostraat, M. L., De Blauwe, J. W., Green, M. L., Bell, L. D., Atwater, H. A., and Flagan, R. C. Ultraclean Two-Stage Aerosol Reactor for Production of Oxide-Passivated Silicon Nanoparticles for Novel Memory Devices. *Journal of The Electrochemical Society 148*, 5 (2001), G265.

[149] Ostraat, M. L., De Blauwe, J. W., Green, M. L., Bell, L. D., Brongersma, M. L., Casperson, J., Flagan, R. C., and Atwater, H. A. Synthesis and characterization of aerosol silicon nanocrystal nonvolatile floating-gate memory devices. *Applied Physics Letters 79*, 3 (2001), 433–435.

[150] Pajor-Świerzy, A., Szczepanowicz, K., Kamyshny, A., and Magdassi, S. Metallic core-shell nanoparticles for conductive coatings and printing. *Advances in Colloid and Interface Science 299* (2022), 102578.

[151] Palchoudhury, S., Baalousha, M., and Lead, J. R. Methods for Measuring Concentration (Mass, Surface Area and Number) of Nanomaterials. In *Frontiers of Nanoscience*, vol. 8. Elsevier, 2015, pp. 153–181.

[152] Park, B. K., Kim, D., Jeong, S., Moon, J., and Kim, J. S. Direct writing of copper conductive patterns by ink-jet printing. *Thin Solid Films 515*, 19 (2007), 7706–7711.

[153] Park, S. T., Kim, T.-H., and Park, D.-W. Influence of injected silver content on synthesis of silver coated nickel particles by DC thermal plasma. *Applied Surface Science 374* (2016), 257–264.

[154] Patscheider, J. Nanocomposite Hard Coatings for Wear Protection. *MRS Bulletin 28*, 3 (2003), 180–183.

[155] Paulitsch, J., Schenkel, M., Zufrass, T., Mayrhofer, P., and Münz, W.-D. Structure and properties of high power impulse magnetron sputtering and DC magnetron sputtering CrN and TiN films deposited in an industrial scale unit. *Thin Solid Films 518*, 19 (2010), 5558–5564.

[156] Pfender, E. Thermal Plasma Technology: Where Do We Stand and Where Are We Going? *Plasma Chemistry and Plasma Processing 19*, 1 (1999), 1–31.

[157] Pogrebnjak, A., Smyrnova, K., and Bondar, O. Nanocomposite Multilayer Binary Nitride Coatings Based on Transition and Refractory Metals: Structure and Properties. *Coatings 9*, 3 (2019), 155.

[158] Ponon, N. K., Appleby, D. J., Arac, E., King, P., Ganti, S., Kwa, K. S., and O'Neill, A. Effect of deposition conditions and post deposition anneal on reactively sputtered titanium nitride thin films. *Thin Solid Films 578* (2015), 31–37.

[159] Prakash, A., McCormick, A. V., and Zachariah, M. R. Tuning the Reactivity of Energetic Nanoparticles by Creation of a CoreShell Nanostructure. *Nano Letters 5*, 7 (2005), 1357–1360.

[160] Pratsinis, S. 18. History of Manufacture of Fine Particles in High-Temperature Aerosol Reactors. In *Aerosol Science and Technology: History and Reviews*, RTI International and D. Ensor, Eds., 1 ed. RTI Press, 2011, pp. 475–508.

[161] R., V. K. R., K., V. A., P. S., K., and Singh, S. P. Conductive silver inks and their applications in printed and flexible electronics. *RSC Advances 5*, 95 (2015), 77760–77790.

[162] Ramírez-Argáez, M. A., González-Rivera, C., and Trápaga, G. Mathematical Modeling of High Intensity Electric Arcs Burning in Different Atmospheres. *ISIJ International 49*, 6 (2009), 796–803.

[163] Rao, N., Girshick, S., Heberlein, J., McMurry, P., Jones, S., Hansen, D., and Micheel, B. Nanoparticle formation using a plasma expansion process. *Plasma Chemistry and Plasma Processing 15*, 4 (1995), 581–606.

[164] Rao, N., Micheel, B., Hansen, D., Fandrey, C., Bench, M., Girshiek, S., Heberlein, J., and McMurry, P. Synthesis of nanophase silicon, carbon, and silicon carbide powders using a plasma expansion process. *Journal of Materials Research 10*, 8 (1995), 2073–2084.

[165] Rosen, Y. S., Lidor, Y., Balter, R., Szeskin, A., Awadallah, A., Shacham-Diamand, Y., and Magdassi, S. Copper interconnections and antennas fabricated by hot-pressing printed copper formate. *Flexible and Printed Electronics 2*, 3 (2017), 035007.

[166] Ryu, C.-H., Joo, S.-J., and Kim, H.-S. Two-step flash light sintering of copper nanoparticle ink to remove substrate warping. *Applied Surface Science 384* (2016), 182–191.

[167] Sahm, T. Flame spray synthesis of tin dioxide nanoparticles for gas sensing. *Sensors and Actuators B: Chemical 98*, 2-3 (2004), 148–153.

[168] Samokhin, A. V., Sinaiskii, V. A., Alekseev, N. V., Troitskaya, E. V., and Tsvetkov, Y. V. Production of titanium nitride nanopowder from titanium hydride based on synthesis in thermal plasma. *Inorganic Materials: Applied Research 5*, 3 (2014), 224–229.

[169] Sankaran, R. M., Holunga, D., Flagan, R. C., and Giapis, K. P. Synthesis of Blue Luminescent Si Nanoparticles Using Atmospheric-Pressure Microdischarges. *Nano Letters 5*, 3 (2005), 537–541.

[170] Scherer, G. W., and Garino, T. Viscous Sintering on a Rigid Substrate. *Journal of the American Ceramic Society 68*, 4 (1985), 216–220.

[171] Schulz, C., Dreier, T., Fikri, M., and Wiggers, H. Gas-phase synthesis of functional nanomaterials: Challenges to kinetics, diagnostics, and process development. *Proceedings of the Combustion Institute 37*, 1 (2019), 83–108.

[172] Shin, M.-S., Lee, K.-H., Kim, J.-G., Choi, S.-Y., Cho, G.-S., and Kim, S.-I. Radio Frequency-Thermal Plasma Synthesis of Metal Nano-Thin Exfoliated Graphite Hybrid. *Journal of Nanoscience and Nanotechnology 15*, 11 (2015), 9045–9051.

[173] Shinde, K. P., Ranot, M., Choi, C. J., Kim, H. S., and Chung, K. C. Plasma-assisted synthesis and study of structural and magnetic properties of Fe/C core shell. *AIP Advances 7*, 7 (2017), 075013.

[174] Siegel, R. W. Nanophase Materials: Synthesis, Structure, and Properties. In *Physics of New Materials*, U. Gonser, R. M. Osgood, H. Sakaki, H. K. V. Lotsch, and F. E. Fujita, Eds., vol. 27. Springer Berlin Heidelberg, Berlin, Heidelberg, 1998, pp. 66–106. Series Title: Springer Series in Materials Science.

[175] Singh, M., Haverinen, H. M., Dhagat, P., and Jabbour, G. E. Inkjet Printing-Process and Its Applications. *Advanced Materials 22*, 6 (2010), 673–685.

[176] Smits, F. M. Measurement of Sheet Resistivities with the Four-Point Probe. *Bell System Technical Journal 37*, 3 (1958), 711–718.

[177] Sorensen, C. M. The Mobility of Fractal Aggregates: A Review. *Aerosol Science and Technology 45*, 7 (2011), 765–779.

[178] Stein, M., Kiesler, D., and Kruis, F. E. Adjustment and Online Determination of Primary Particle Size in Transferred Arc Synthesis of Copper Nanoparticles. *Aerosol Science and Technology 47*, 11 (2013), 1276–1284.

[179] Stein, M., Kiesler, D., and Kruis, F. E. Effect of carrier gas composition on transferred arc metal nanoparticle synthesis. *Journal of Nanoparticle Research 15*, 1 (2013), 1400.

[180] Stein, M., and Kruis, F. E. Optimization of a transferred arc reactor for metal nanoparticle synthesis. *Journal of Nanoparticle Research 18*, 9 (2016), 258.

[181] Stein, M., and Kruis, F. E. Scaling-up metal nanoparticle production by transferred arc discharge. *Advanced Powder Technology 29*, 12 (2018), 3138–3144.

[182] Stokes, D. Environmental scanning electron microscopy (ESEM): principles and applications to food microstructures. In *Food Microstructures*. Elsevier, 2013, pp. 3–26.

[183] Sundgren, J.-E. Structure and properties of TiN coatings. *Thin Solid Films 128*, 1-2 (1985), 21–44.

[184] Suresh, K., Selvarajan, V., and Mohai, I. Synthesis and characterization of iron aluminide nanoparticles by DC thermal plasma jet. *Vacuum 82*, 5 (2008), 482–490.

[185] Tanaka, M., Noda, J., Watanabe, T., Matsuno, J., and Tsuchiyama, A. Formation mechanism of metal embedded amorphous silicate nanoparticles by induction thermal plasmas. *Journal of Physics: Conference Series 518* (2014), 012025.

[186] Teoh, W. Y., Amal, R., and Mädler, L. Flame spray pyrolysis: An enabling technology for nanoparticles design and fabrication. *Nanoscale 2*, 8 (2010), 1324.

[187] Thampi, V. A., Bendavid, A., and Subramanian, B. Nanostructured TiCrN thin films by Pulsed Magnetron Sputtering for cutting tool applications. *Ceramics International 42*, 8 (2016), 9940–9948.

[188] Tian, Y., Jia, Y., Bao, Y., and Chen, Y. Macro-quantity synthesis of AlN nanowires via combined technique of arc plasma jet and thermal treatment. *Diamond and Related Materials 16*, 2 (2007), 302–305.

[189] Tillmann, W., Kokalj, D., and Stangier, D. Influence of the deposition parameters on the texture and mechanical properties of magnetron sputtered cubic MoNx thin films. *Materialia 5* (2019), 100186.

[190] Tillmann, W., Kokalj, D., Stangier, D., Fu, Q., and Kruis, E. Combination of an atmospheric pressured arc reactor and a magnetron sputter device for the synthesis of novel nanostructured thin films. *Thin Solid Films 689* (2019), 137528.

[191] Tillmann, W., Kokalj, D., Stangier, D., Fu, Q., and Kruis, F. E. Bias-voltage effect on the TiN nanoparticle injection into magnetron sputtered CrN thin films towards nc-TiN/nc-CrN composites. *Applied Surface Science Advances 6* (2021), 100149.

[192] Tillmann, W., Kokalj, D., Stangier, D., Fu, Q., and Kruis, F. E. Influence of the PVD process conditions on the incorporation of TiN nanoparticles into magnetron sputtered CrN thin films. *Surface and Coatings Technology 409* (2021), 126935.

[193] Tillmann, W., Kokalj, D., Stangier, D., Fu, Q., Kruis, F. E., Kesper, L., Berges, U., and Westphal, C. On the synthesis and structural evolution of artificial CrN/TiN nanocomposites. *Applied Surface Science 535* (2021), 147736.

[194] Tsai, C.-Y., Hsi, H.-C., Kuo, T.-H., Chang, Y.-M., and Liou, J.-H. Preparation of Cu-Doped TiO2 Photocatalyst with Thermal Plasma Torch for Low-

Concentration Mercury Removal. *Aerosol and Air Quality Research 13*, 2 (2013), 639–648.

[195] Ullmann, M., Friedlander, S. K., and Schmidt-Ott, A. Nanoparticle Formation by Laser Ablation. *Journal of Nanoparticle Research 4*, 6 (2002), 499–509.

[196] Uschakov, , Karpov, I., Lepeshev, , and Petrov, M. Plasma-chemical synthesis of copper oxide nanoparticles in a low-pressure arc discharge. *Vacuum 133* (2016), 25–30.

[197] Ushakov, A. V., Karpov, I. V., and Lepeshev, A. A. Influence of the oxygen concentration on the formation of crystalline phases of ZrO_2 nanoparticles during the low-pressure arc-discharge plasma synthesis. *Physics of the Solid State 57*, 11 (2015), 2320–2322.

[198] Vaseashta, A., Mihailescu, I. N., and Organization, N. A. T., Eds. *Functionalized nanoscale materials, devices and systems.* NATO science for peace and security series. Series B, Physics and biophysics. Springer, Dordrecht, 2008. Meeting Name: NATO Advanced Study Institute on Functionalized Nanoscale Materials, Devices and Systems for Chem.-bio Sensors, Photonics and Energy Generation and Storage OCLC: ocn233935190.

[199] Vollath, D. Plasma Synthesis of Nanoparticles. *KONA Powder and Particle Journal 25*, 0 (2007), 39–55.

[200] Wang, X., Hafiz, J., Mukherjee, R., Renault, T., Heberlein, J., Girshick, S. L., and McMurry, P. H. System for In Situ Characterization of Nanoparticles Synthesized in a Thermal Plasma Process. *Plasma Chemistry and Plasma Processing 25*, 5 (2005), 439–453.

[201] Wang, X., Kruis, F. E., and McMurry, P. H. Aerodynamic Focusing of Nanoparticles: I. Guidelines for Designing Aerodynamic Lenses for Nanoparticles. *Aerosol Science and Technology 39*, 7 (2005), 611–623.

[202] Wang, X., and McMurry, P. H. A Design Tool for Aerodynamic Lens Systems. *Aerosol Science and Technology 40*, 5 (2006), 320–334.

[203] Wang, X., and McMurry, P. H. An experimental study of nanoparticle focusing with aerodynamic lenses. *International Journal of Mass Spectrometry 258*, 1-3 (2006), 30–36.

[204] Whitehead, C. B., Özkar, S., and Finke, R. G. LaMer's 1950 model of particle formation: a review and critical analysis of its classical nucleation and fluctuation theory basis, of competing models and mechanisms for phase-changes and particle

formation, and then of its application to silver halide, semiconductor, metal, and metal-oxide nanoparticles. *Materials Advances 2*, 1 (2021), 186–235.

[205] Winterer, M. *Nanocrystalline ceramics: synthesis and structure.* No. v. 53 in Springer series in materials science. Springer, Berlin ; New York, 2002.

[206] Woo, K., Kim, Y., Lee, B., Kim, J., and Moon, J. Effect of Carboxylic Acid on Sintering of Inkjet-Printed Copper Nanoparticulate Films. *ACS Applied Materials & Interfaces 3*, 7 (2011), 2377–2382.

[207] Yang, X., Li, C., Yang, L., Yan, Y., and Qian, Y. Reduction-Nitridation Synthesis of Titanium Nitride Nanocrystals. *Journal of the American Ceramic Society 86*, 1 (2003), 206–208.

[208] Yeh, Y.-W., Raitses, Y., Koel, B. E., and Yao, N. Stable synthesis of few-layered boron nitride nanotubes by anodic arc discharge. *Scientific Reports 7*, 1 (2017), 3075.

[209] Young, R. A., Ed. *The Rietveld method*, 1. publ. in paperb., reprint ed. No. 5 in Monographs on crystallography. Oxford Univ. Press, Oxford, 2002.

[210] Zhang, G., Yan, P., Wang, P., Chen, Y., and Zhang, J. The structure and tribological behaviors of CrN and Cr–Ti–N coatings. *Applied Surface Science 253*, 18 (2007), 7353–7359.

Appendix A: Suggested anode holder for arc discharge reactor

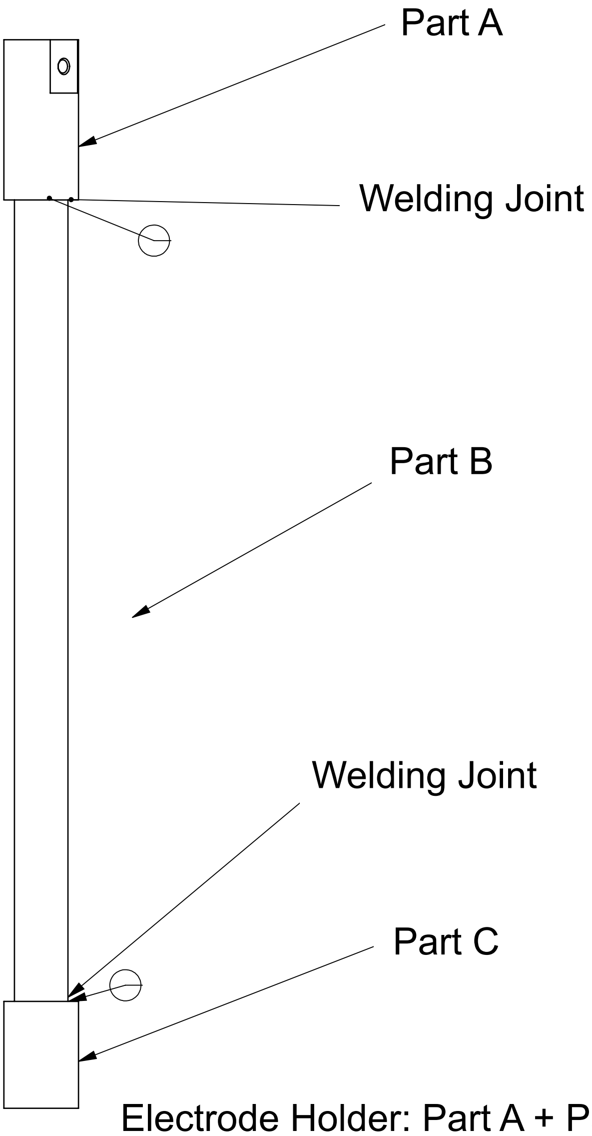

Electrode Holder: Part A + Part B + Part C

Material: Stainless Steel

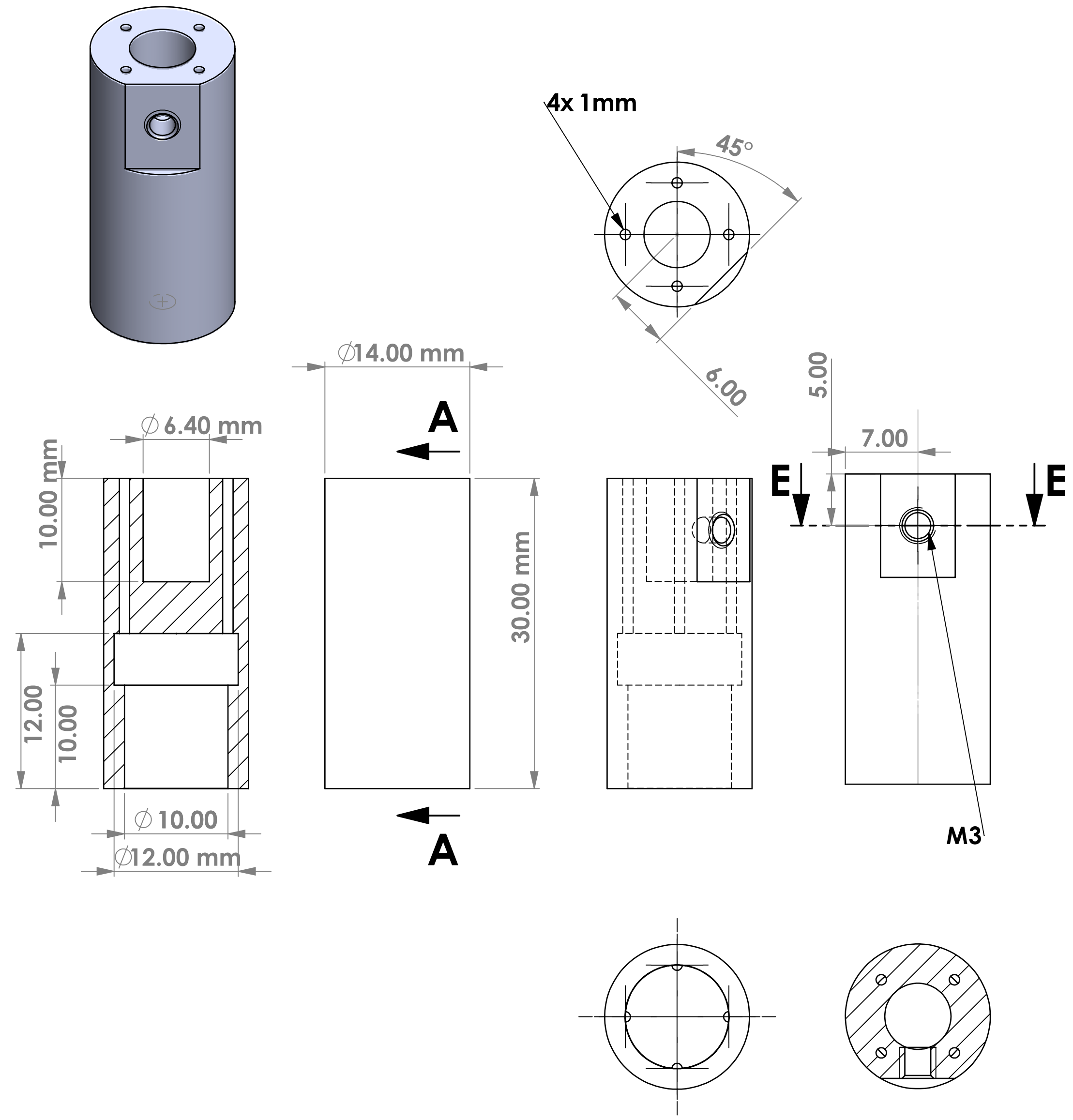

Electrode Holder: Part A

Material: Stainless Steel

Scale: 2:1

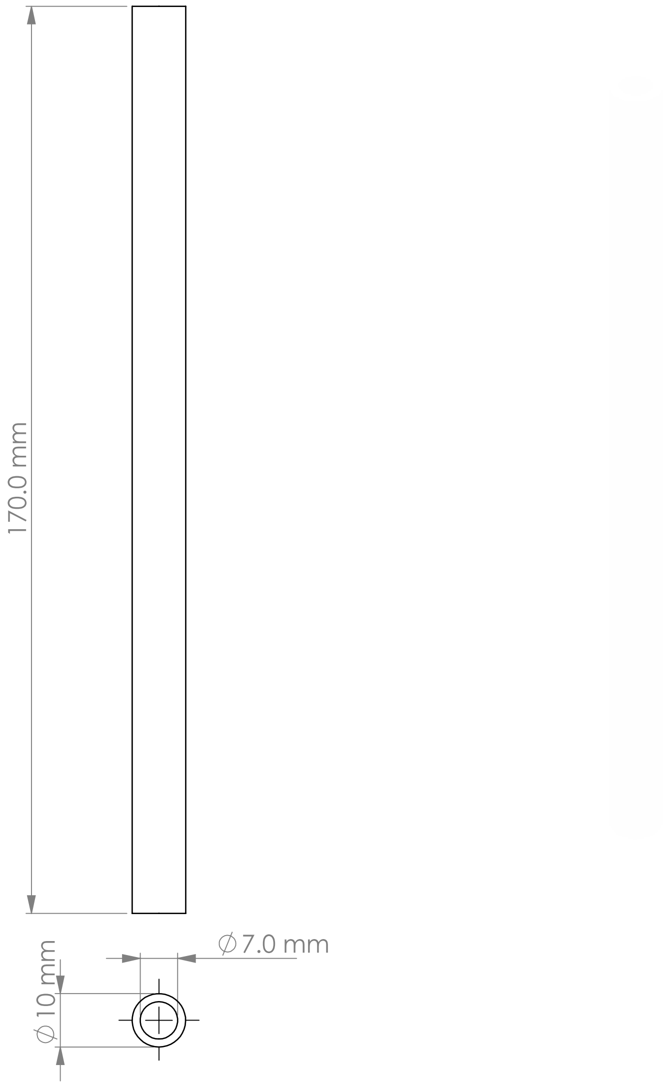

Electrode Holder: Part B

Material: Stainless Steel

Scale: 1:1

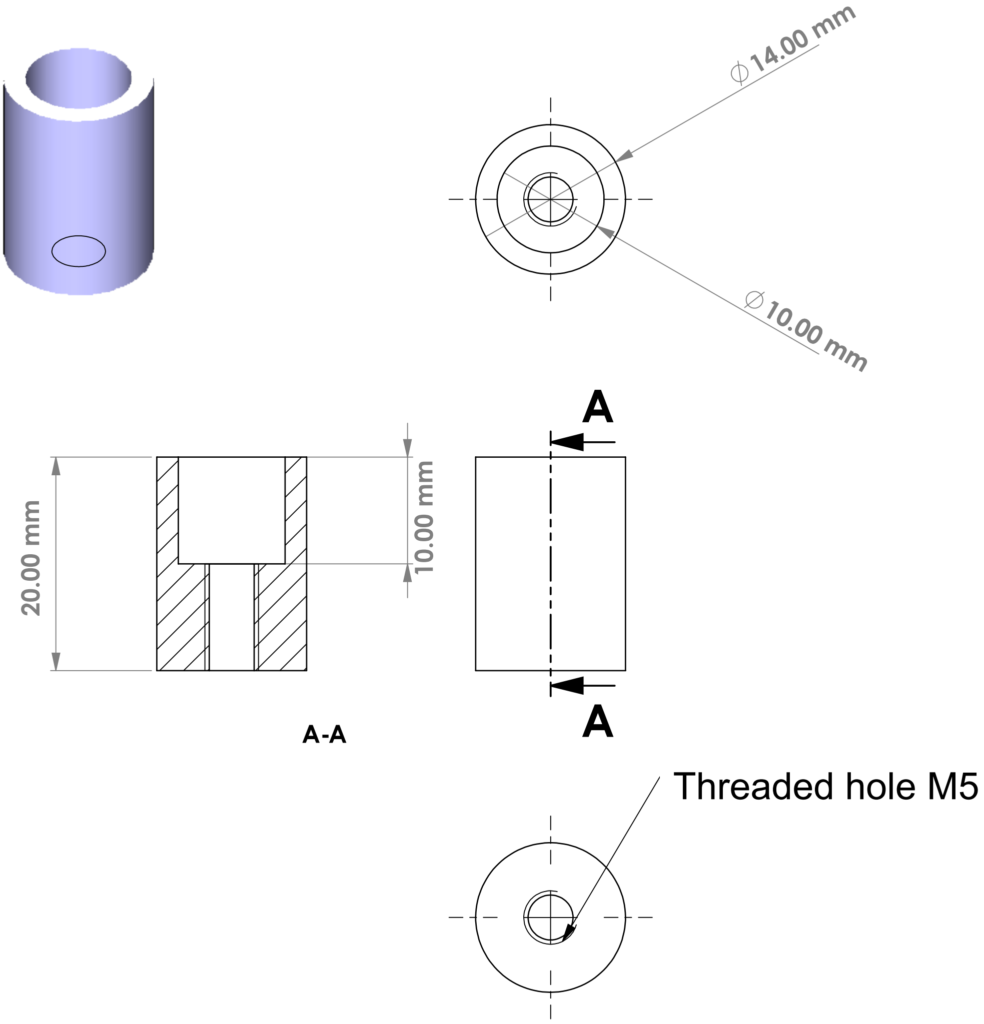

Electrode Holder: Part C

Material: Stainless Steel

Scale: 2:1

Appendix B: Configuration of accelerating nozzles for ALS #2 and ALS #3

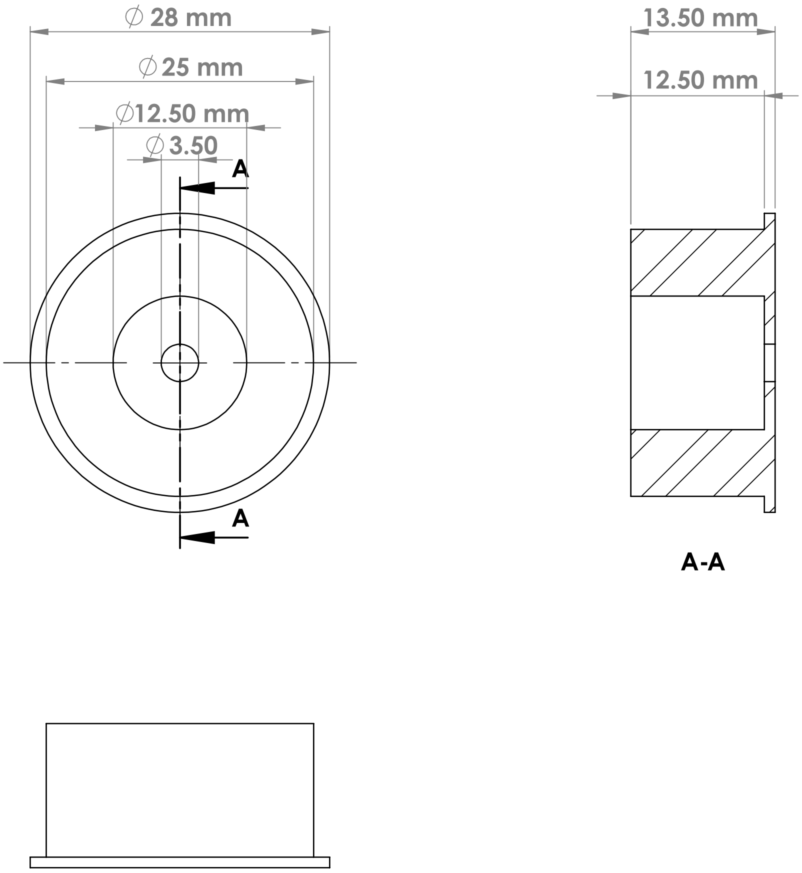

Accelerating Nozzle for ALS #2

Material: Stainless Steel

Scale: 2:1

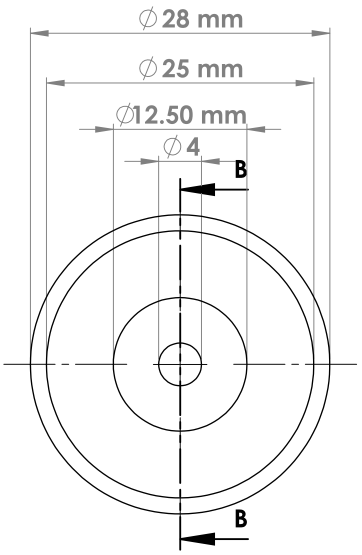

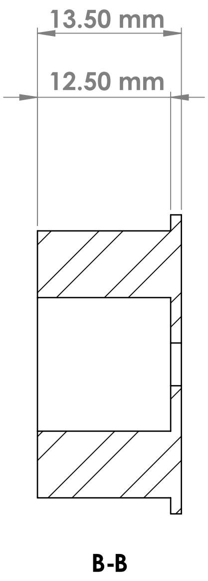

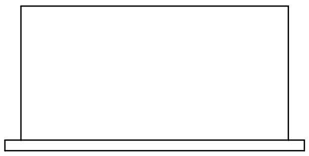

Accelerating Nozzle for ALS #3

Material: Stainless Steel

Scale: 2:1

Appendix C: CFD simulation to assess particle trajectories in ALS

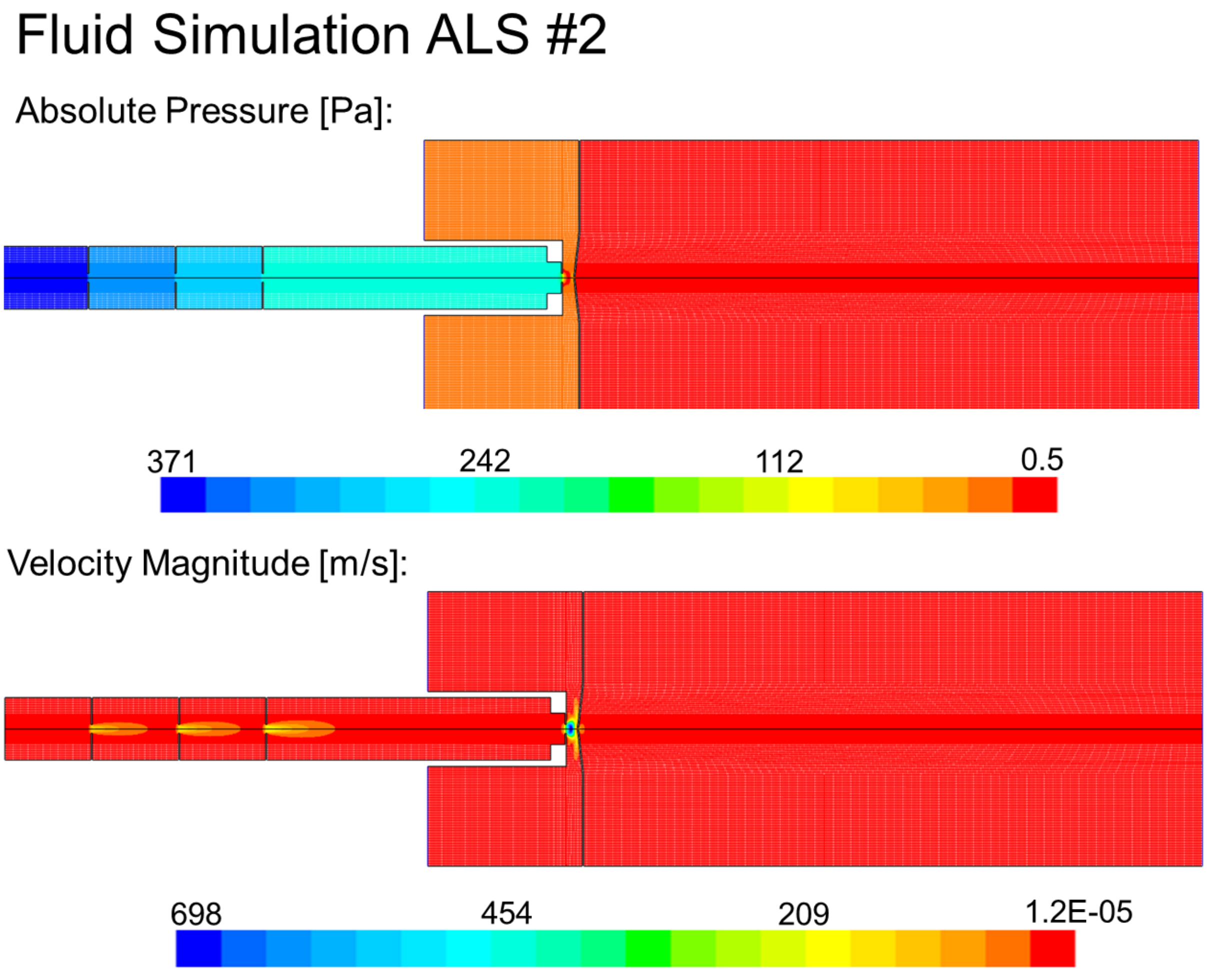
Fluid Simulation ALS #2
Absolute Pressure [Pa]:
371
242
112
0.5
Velocity Magnitude [m/s]:
698
454
209
1.2E-05

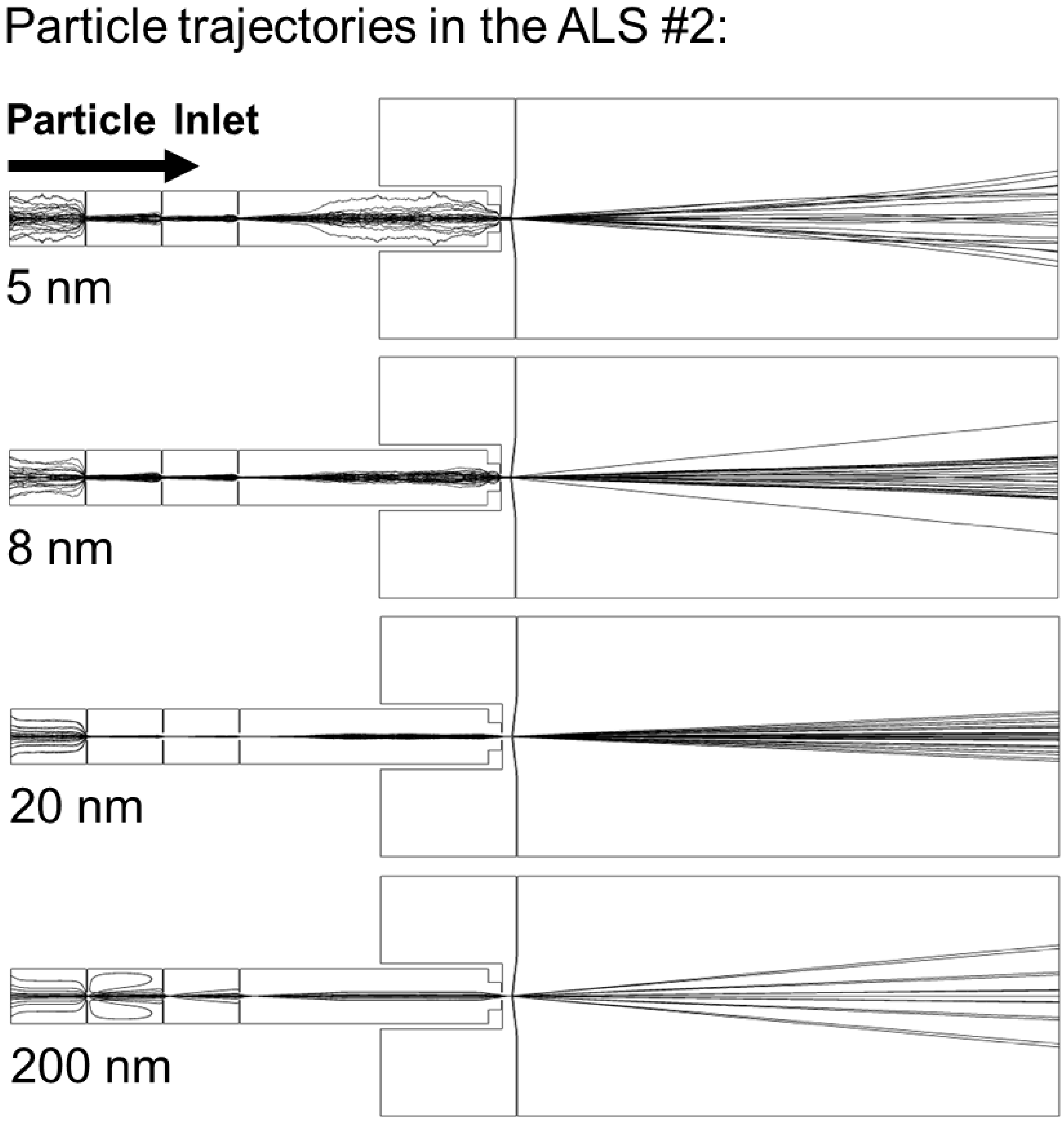
Particle trajectories in the ALS #2:
Particle Inlet
5 nm
8 nm
20 nm
200 nm

Fluid Simulation ALS #3

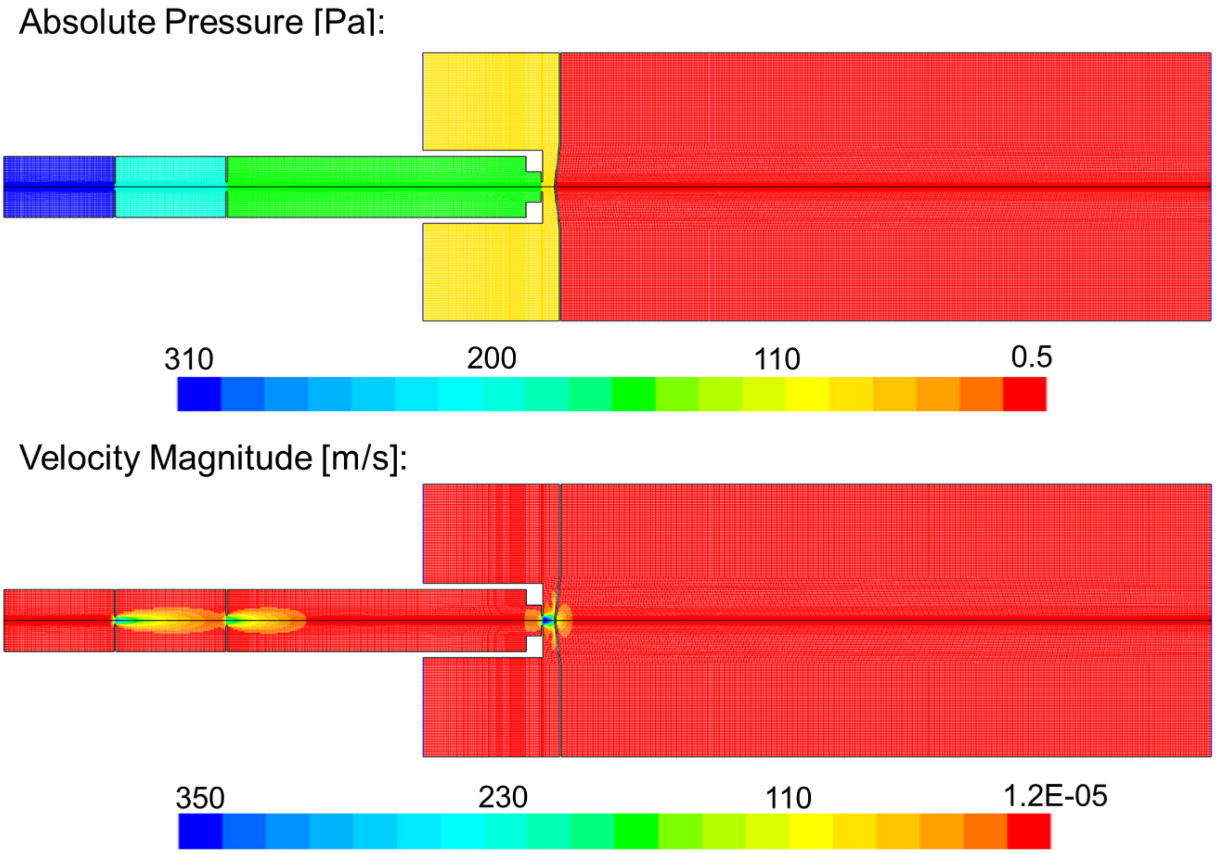

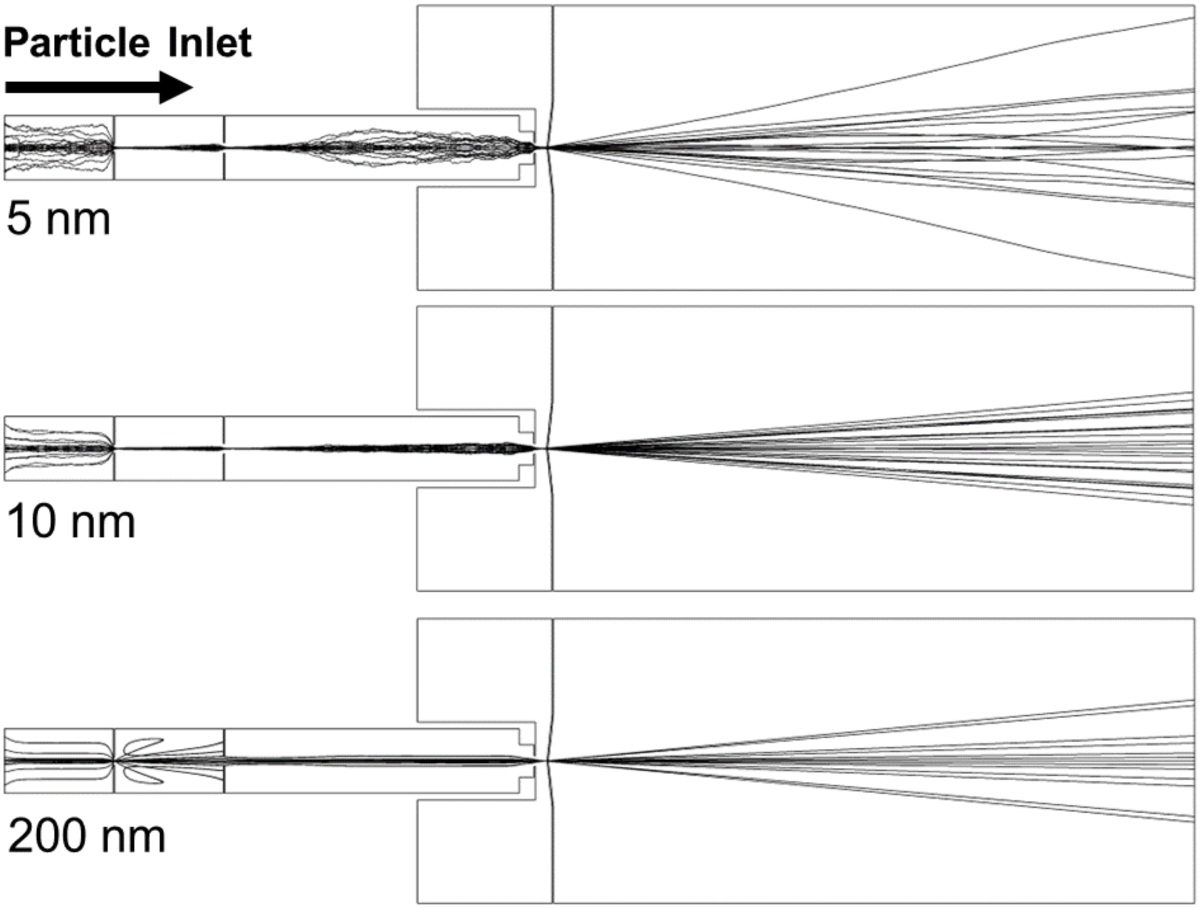

Particle trajectories in ALS #3:

DOI: 10.17185/duepublico/82250
URN: urn:nbn:de:hbz:465-20240814-083914-8